Micro- and Nanofluidic

Dimensionless Numbers

TABLE I. Dimensionless numbers used in this review.

Re	Reynolds	$\frac{\rho U_0 L_0}{\eta}$	inertial/viscous	Eq. (5)
Pe	Péclet	$\frac{U_0 L_0}{D}$	convection/diffusion	Eq. (7)
Ca	capillary	$\frac{\eta U_0}{\gamma}$	viscous/interfacial	Eq. (19)
Wi	Weissenberg	$\tau_p \dot{\gamma}$	polymer relaxation time/shear rate time	Eq. (24)
De	Deborah	$\frac{\tau_p}{\tau_{\text{flow}}}$	polymer relaxation time/flow time	Eq. (25)
El	elasticity	$\frac{\tau_p \eta}{\rho h^2}$	elastic effects/inertial effects	Eq. (26)
Gr	Grashof	$\frac{\rho U_b L_0}{\eta}$	Re for buoyant flow	Eq. (30)
Ra	Rayleigh	$\frac{U_b L_0}{D}$	Pe for buoyant flow	Eq. (29)
Kn	Knudsen	$\frac{\beta}{L_0}$	slip length/macroscopic length	Eqs. (36) and (38)

Reynolds Number

- Reynolds number

$$Re = \frac{\rho v_s L}{\mu} = \frac{v_s L}{\nu} = \frac{\text{Inertial forces}}{\text{Viscous forces}}$$

*v*s - mean fluid velocity,
L - characteristic length,
μ - (absolute) dynamic fluid viscosity,
ν - kinematic fluid viscosity: $\nu = \mu / \rho$,
ρ - fluid density.

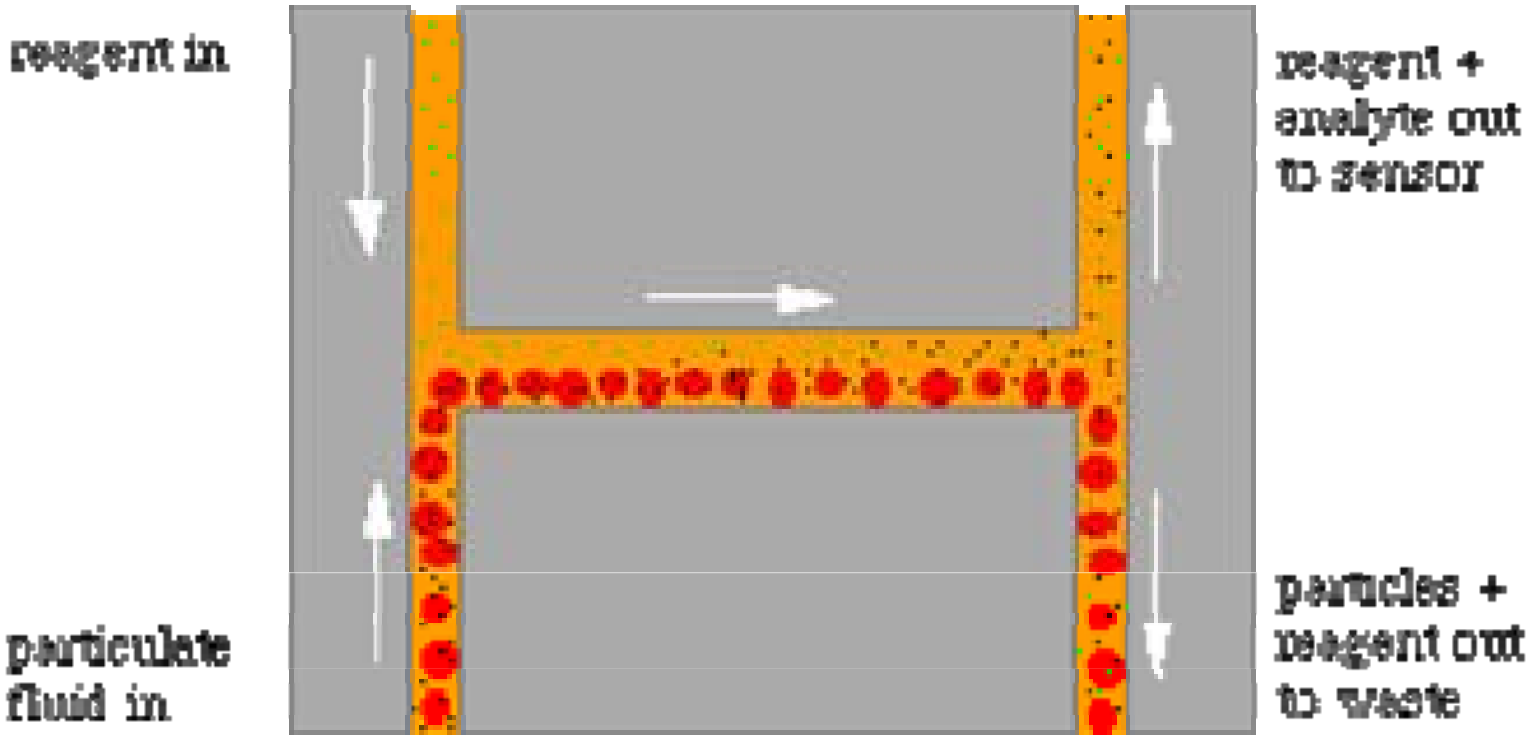
reagent in
particulate fluid in
reagent + analyte out to sensor
particles + reagent out to waste

Magnetic Separation in H-Channel System

Using Laminar Flow

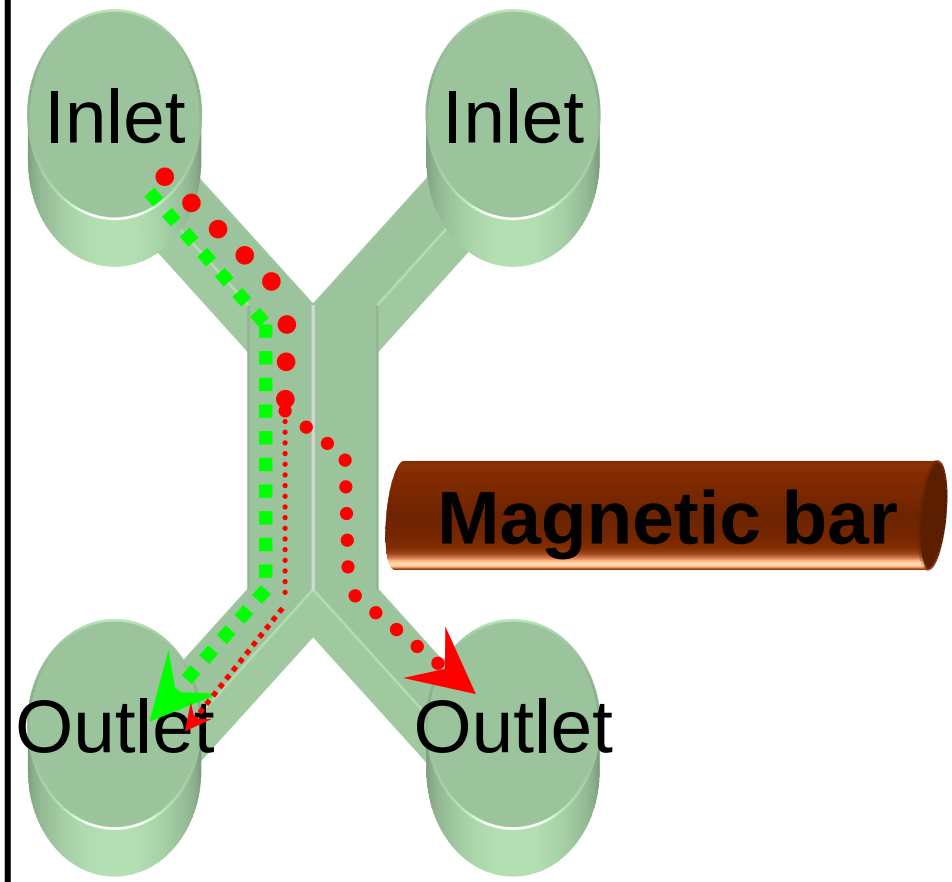

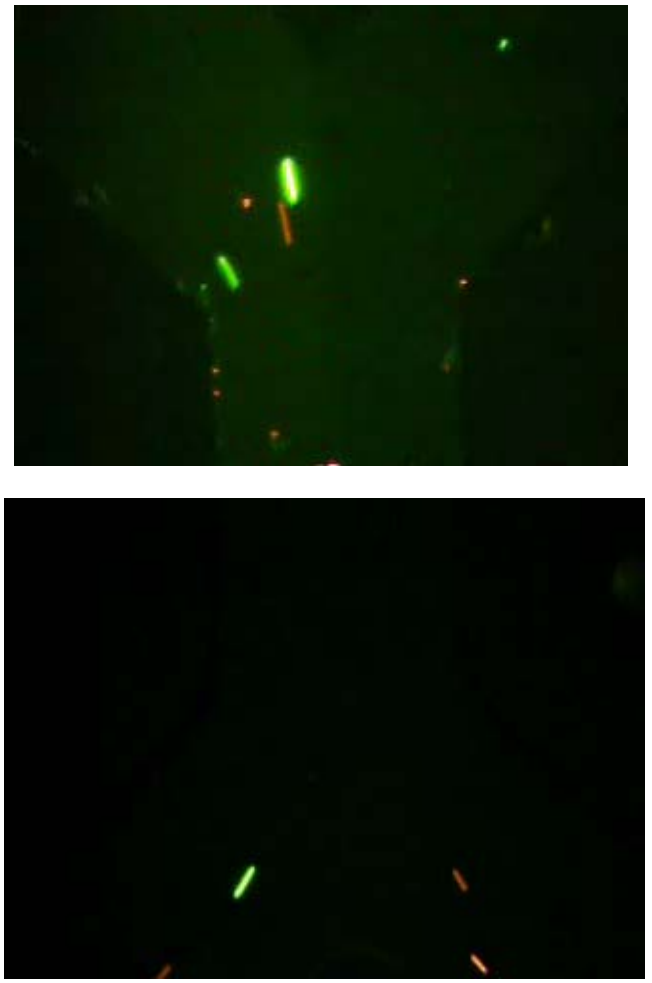

Peclet Number

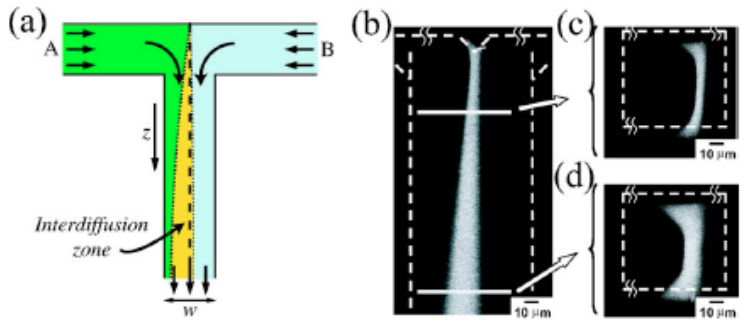

FIG. 5. (Color in online edition) (a) The microfluidic T sensor (Kamholz *et al.*, 1999). Different fluids are brought together at a T junction to flow alongside each other down the channel. A simple estimate suggests that the interdiffusion zone spreads diffusively, with the square root of time (or downstream distance), although (b)–(d) show this naive argument to break down near the "floor" and "ceiling" of the channel. Confocal microscopy reveals the three-dimensional nature of the spreading of the interface in the T sensor (Ismagilov *et al.*, 2000). (b) Fluorescent tracers mark reactions occurring in the interdiffusion zone, here seen from above. (c), (d) The no-slip nature of the top and bottom walls of the channel affect the flow profile, so that tracer molecules near the boundaries diffuse and spread with $z^{1/3}$, rather than $z^{1/2}$. Reprinted with permission from Ismagilov *et al.*, 2000. ©2000, AIP.

the channel is homogenized? A simple estimate requires the particles or molecules to diffuse across the entire channel, giving a time $\tau_D \sim w^2/D$, where w is the width of the channel. During this time, the stripe will have moved a distance $Z \sim U_0 w^2/D$ down the channel, so that the number of channel widths required for complete mixing would be of order

$$\frac{Z}{w} \sim \frac{U_0 w}{D} \equiv \mathrm{Pe}. \qquad (7)$$

100-μm channel at 100 μm/s

Pe ~250 channel widths (approximately 2.5 cm and 4 min)

Forward (advective) vs. transverse (diffusive) transport

Peclet number:

$$Pe = \frac{ud}{D}$$

Dispersion: distortion of a plug due to various processes

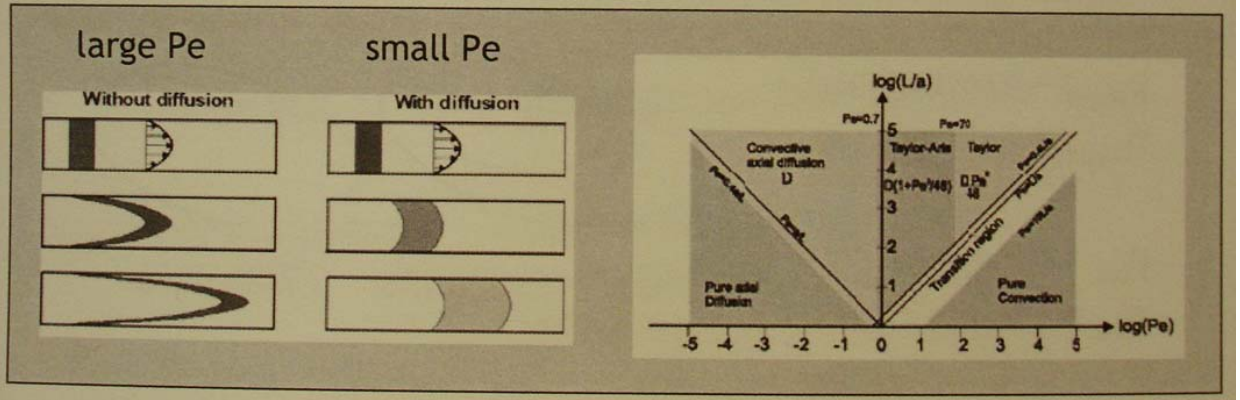

figures courtesy of F. R. Hansen, MIC

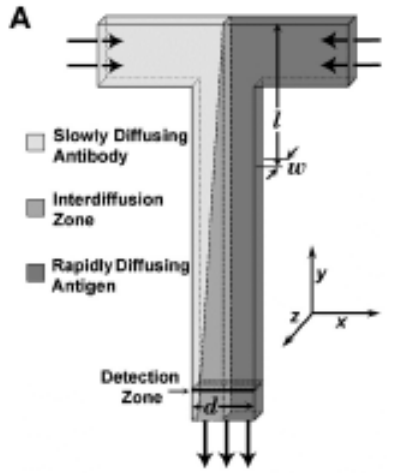
A
Slowly Diffusing Antibody
Interdiffusion Zone
Rapidly Diffusing Antigen
Detection Zone
l
w
d
y
z
x

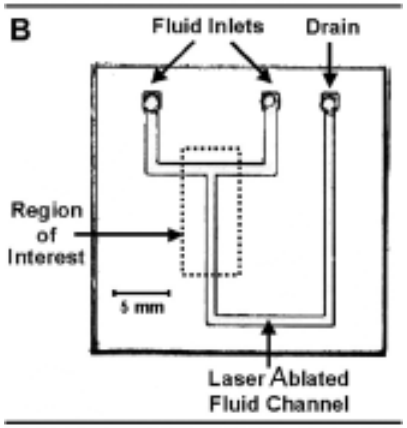
B
Fluid Inlets
Drain
Region of Interest
5 mm
Laser Ablated Fluid Channel

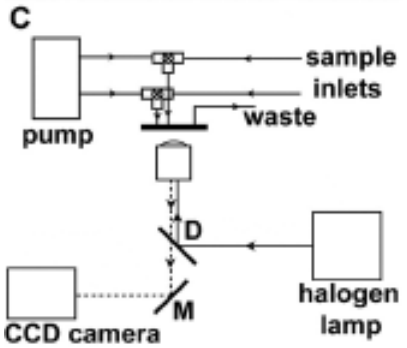
C
sample inlets
waste
pump
D
M
halogen lamp
CCD camera

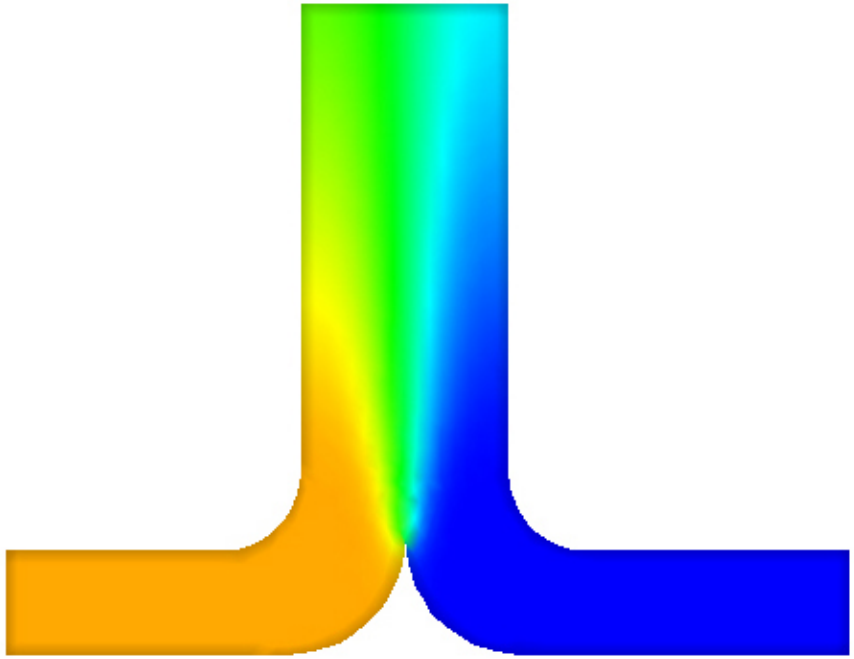

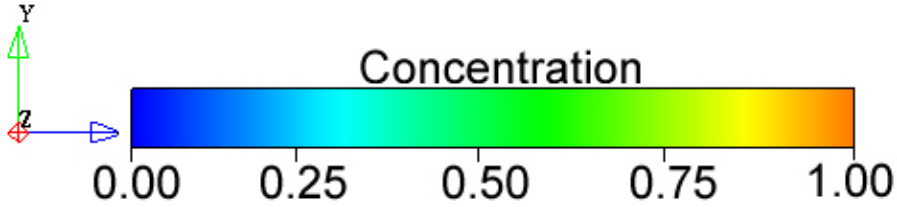
Y
Z
Concentration
0.00
0.25
0.50
0.75
1.00

Capillary Number

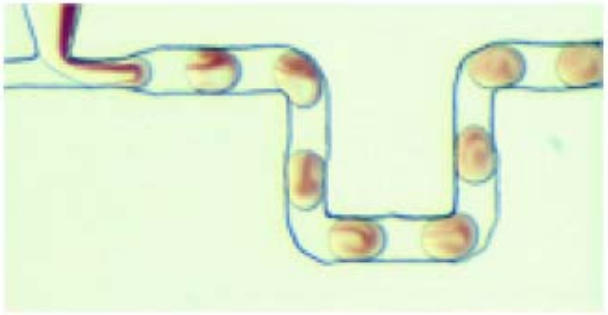

FIG. 16. (Color in online edition) Chaotic advection in a pumped droplet. A droplet driven down a channel experiences a dipolar, circulating flow; when the channel changes direction, the axis of the dipole changes as well. Alternating dipolar flows drive rapid mixing by chaotic advection, with mixing lengths that vary logarithmically with Pe. Reprinted with permission from Song, Bringer, *et al.*, 2003. ©2003, AIP.

face (Taylor, 1934). Capillary stresses of magnitude γ/R balance viscous stresses $\eta U_0/h$, giving a characteristic droplet size

$$R \sim \frac{\gamma}{\eta U_0} h = \frac{h}{\mathrm{Ca}}. \tag{15}$$

Here we have introduced the capillary number

$$\mathrm{Ca} = \frac{\eta U_0}{\gamma}, \tag{16}$$

a dimensionless parameter found whenever interfacial stresses compete with viscous stresses.

$4/3\pi R^3 \rho g = \gamma R$

http://www.seas.harvard.edu/projects/weitzlab/coolpic02122006.html

http://www.seas.harvard.edu/projects/weitzlab/coolpic03102006.html

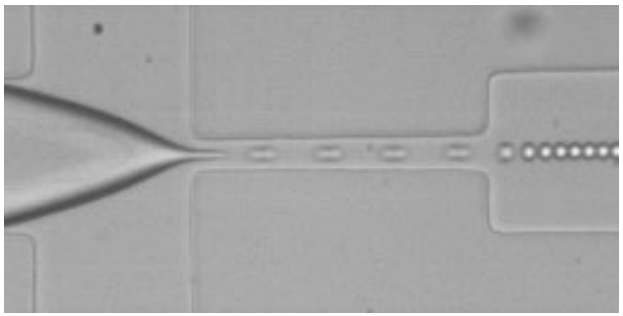

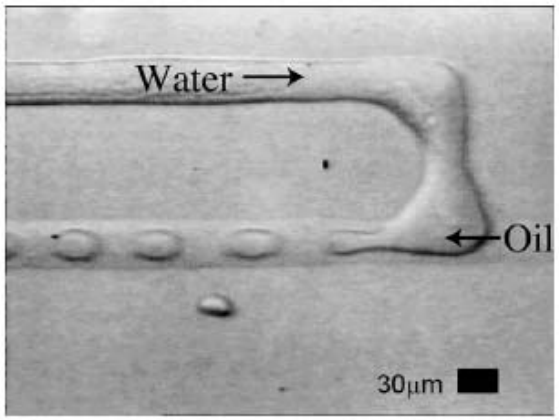

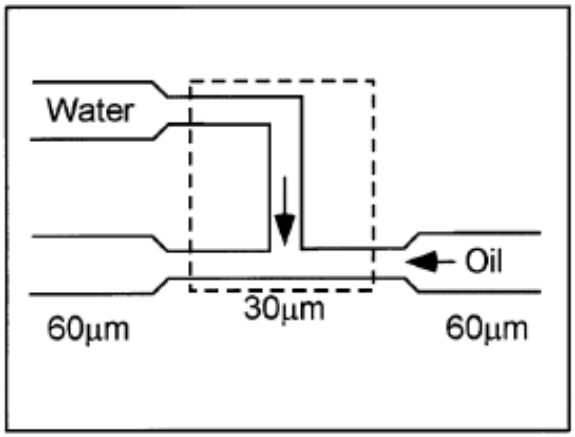

FIG. 15. Monodisperse microdroplet generation in a simple microfluidic device. The interface between flowing immiscible fluids is driven by competing stresses: viscous shear stresses tend to extend and drag the interface, whereas surface tension tends to reduce the interfacial area. The competition between the two leads to drop sizes (scaled by the channel height h) of order $R \sim \mathrm{Ca}^{-1}$. Adapted with permission from Thorsen *et al.*, 2001.

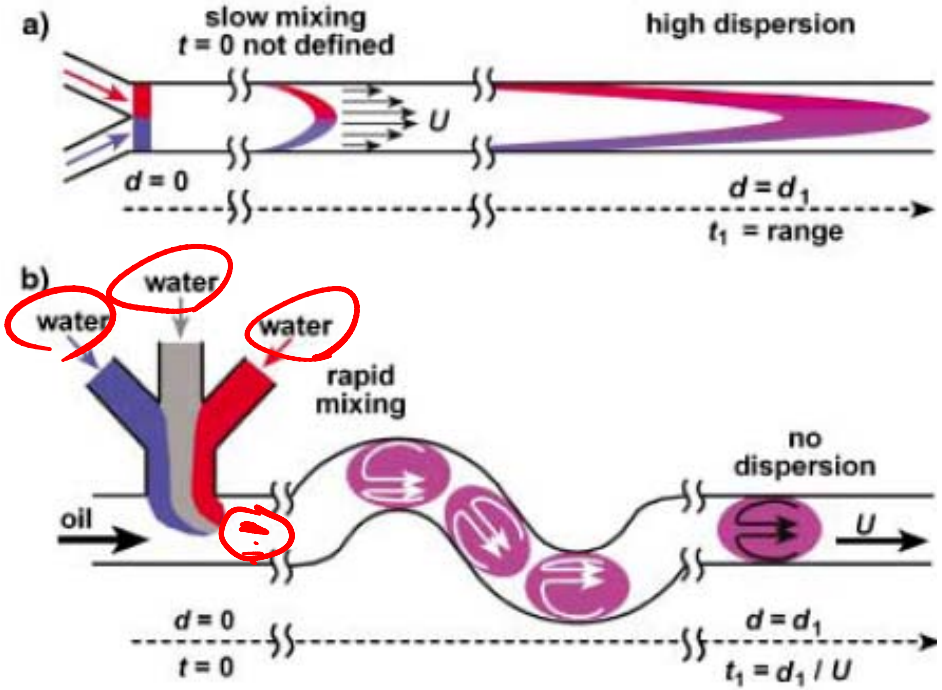

Figure 1. Schematic comparison of a reaction A + B conducted in a standard pressure-driven microfluidic system device (a) and in the microfluidic device described here (b). a) Reaction time $t \neq d/U$. b) Reaction time $t = d/U$. Two aqueous reagents (red, A and blue, B) can form laminar streams separated by a gray "divider" aqueous stream in a microchannel. When the three streams enter the channel with a flowing immiscible fluid, they form droplets (plugs). The reagents come into contact as the contents of the droplets are rapidly mixed. Internal recirculation within plugs flowing through channels of different geometries is shown schematically by arrows.

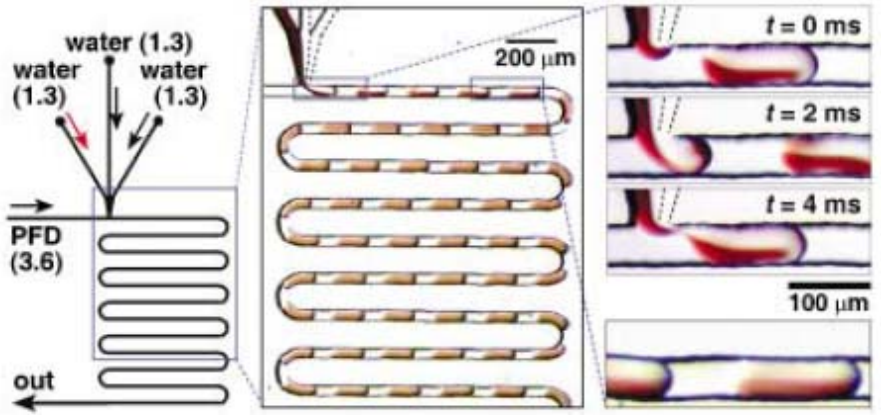

Figure 2. Spontaneous formation of uniform plugs out of multiple aqueous streams. Left: Schematic diagram of the microchannel network. Volumetric flow rates for all streams (in $\mu L\,min^{-1}$) are given in parenthesis. Middle: Microphotograph (10 μs exposure) of plug formation and transport. Right: Magnified microphotographs (10 μs exposure) of the plug-forming region at different time points. All microchannels had $50 \times 50\ \mu m^2$ cross sections. Total flow rate in the main channel: $7.5\ \mu L\,min^{-1}$ ($50\ mm\,s^{-1}$ average flow velocity); $Re \sim 2.5$ (water), ~0.93 (PFD). PFD here stands for a 10:1 mixture of perfluorodecaline and $C_6F_{11}C_2H_4OH$. Red stream: solution of $[Fe(SCN)_x]^{(3-x)+}$ prepared by mixing 0.067 M $Fe(NO_3)_3$ with 0.2 M KSCN; colorless streams: 0.2 M KNO_3.

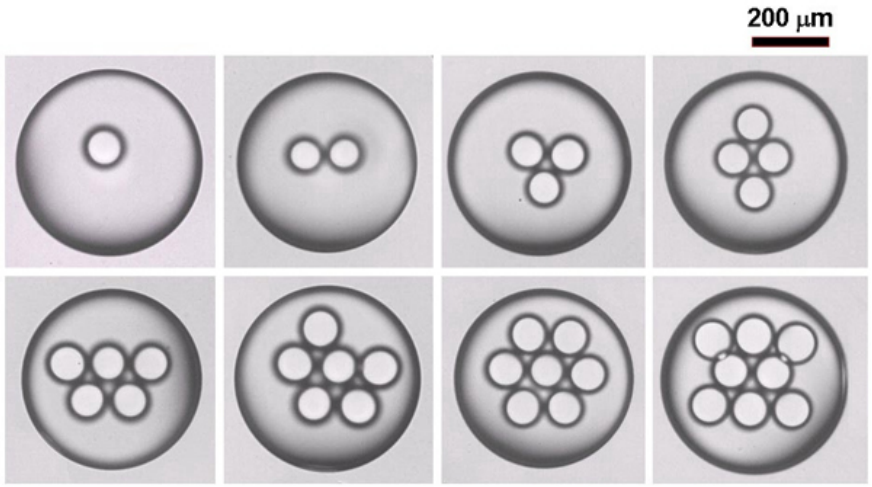
200 μm

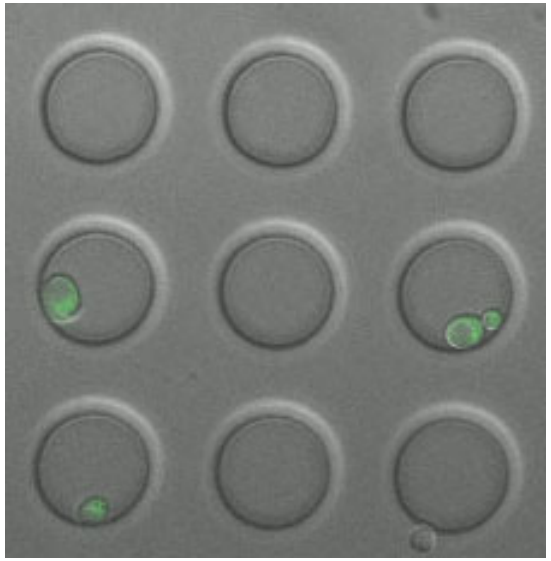

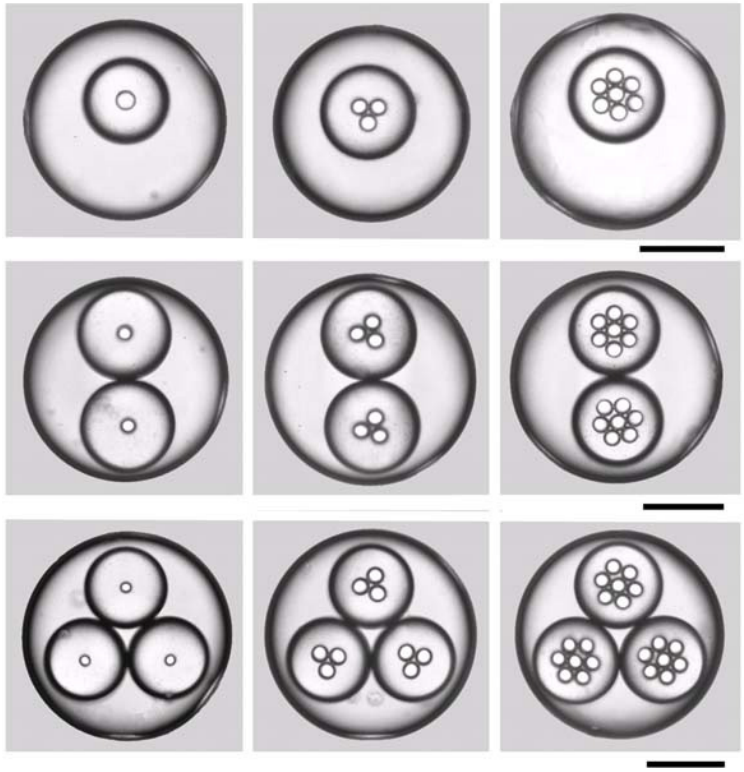

Application of nanofluidic channels

- Single cell studies
  - E-coli: 10 fL
  - Eukaryotic cell: 10 pL
- Control factor
  - DNA-protein interaction
- Genetic contents
  - SNP
  - Genome
- Length distribution

A DNA prism for high-speed continuous fractionation of large DNA molecules

nature biotechnology • VOLUME 20 • OCTOBER 2002

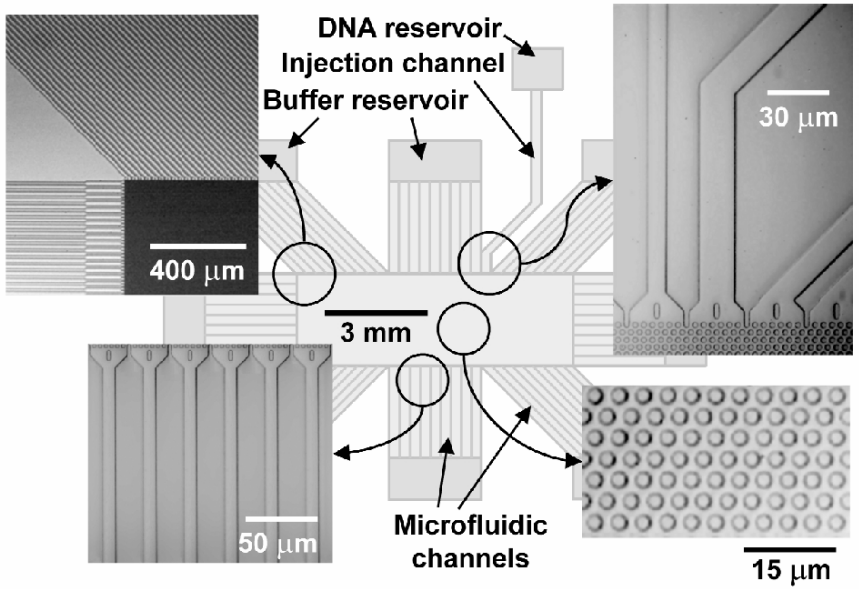

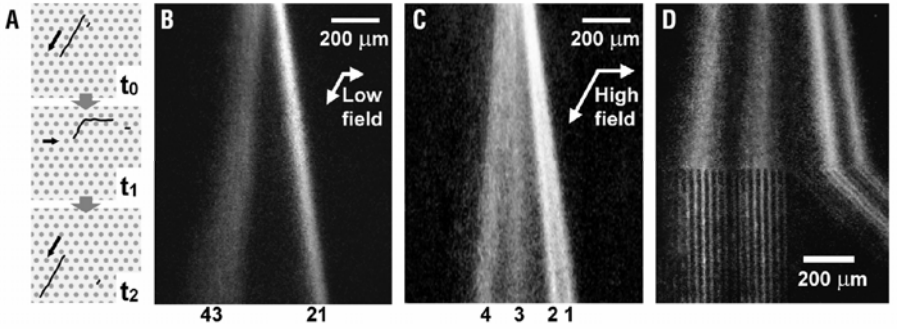

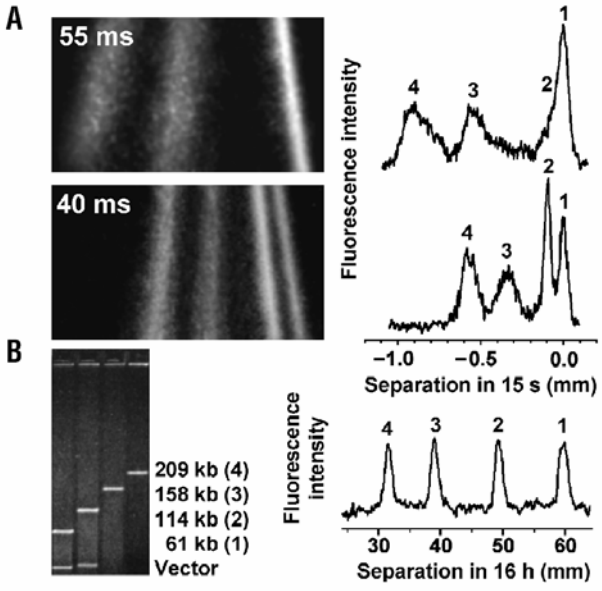

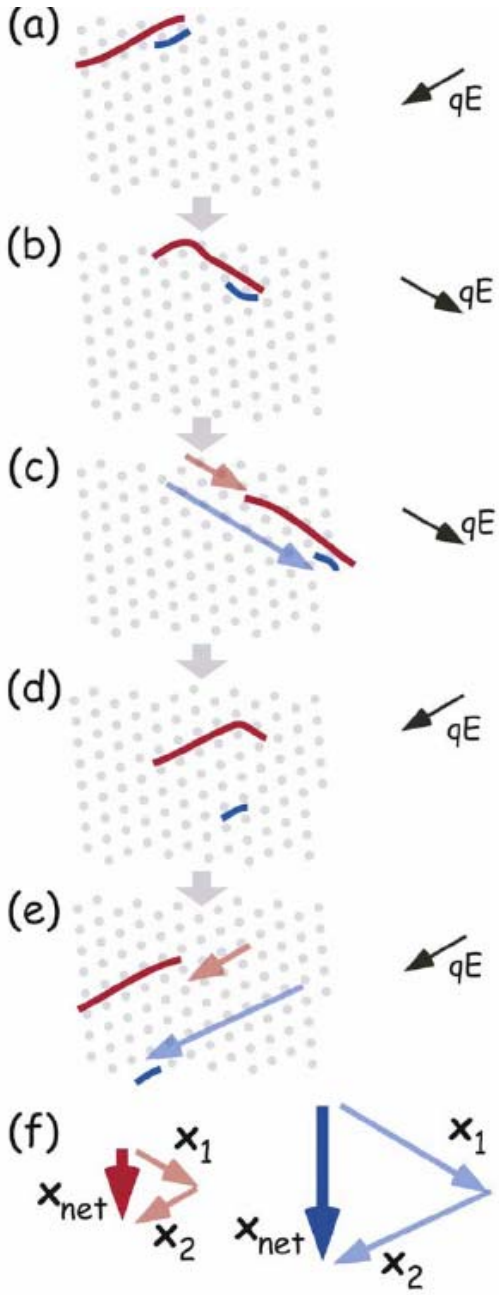
(a)
qE
(b)
qE
(c)
qE
(d)
qE
(e)
qE
(f)
x1
xnet
x2
x1
xnet
x2

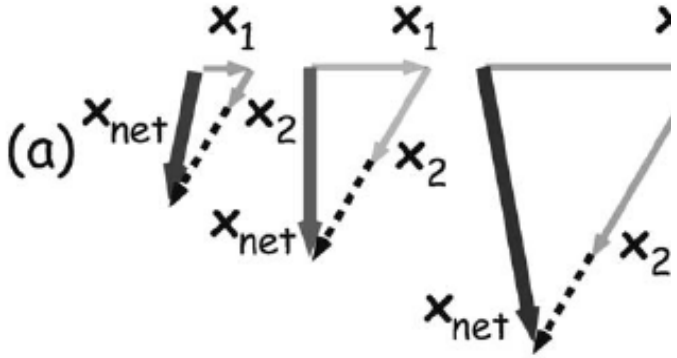
(a)
x1
xnet
x2
x1
x2
xnet
x2
xnet


(b)

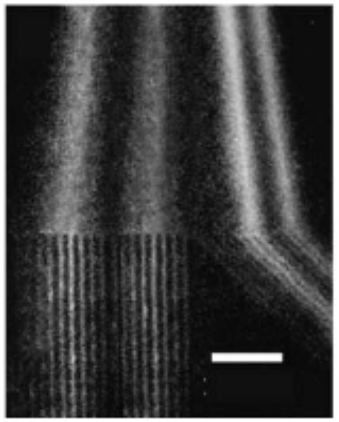
(c)

Continuous Particle Separation Through Deterministic Lateral Displacement

SCIENCE VOL 304 14 MAY 2004

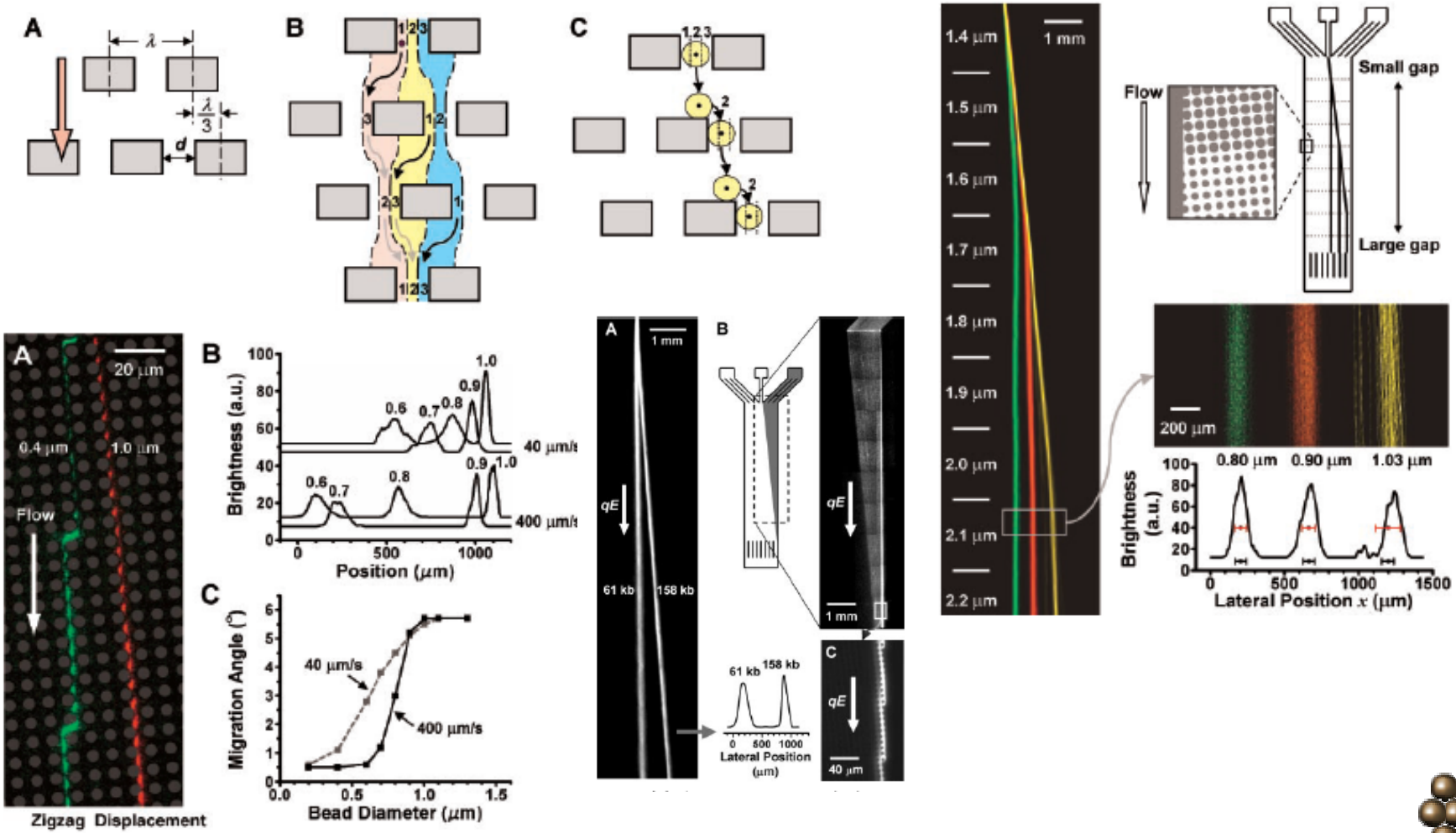

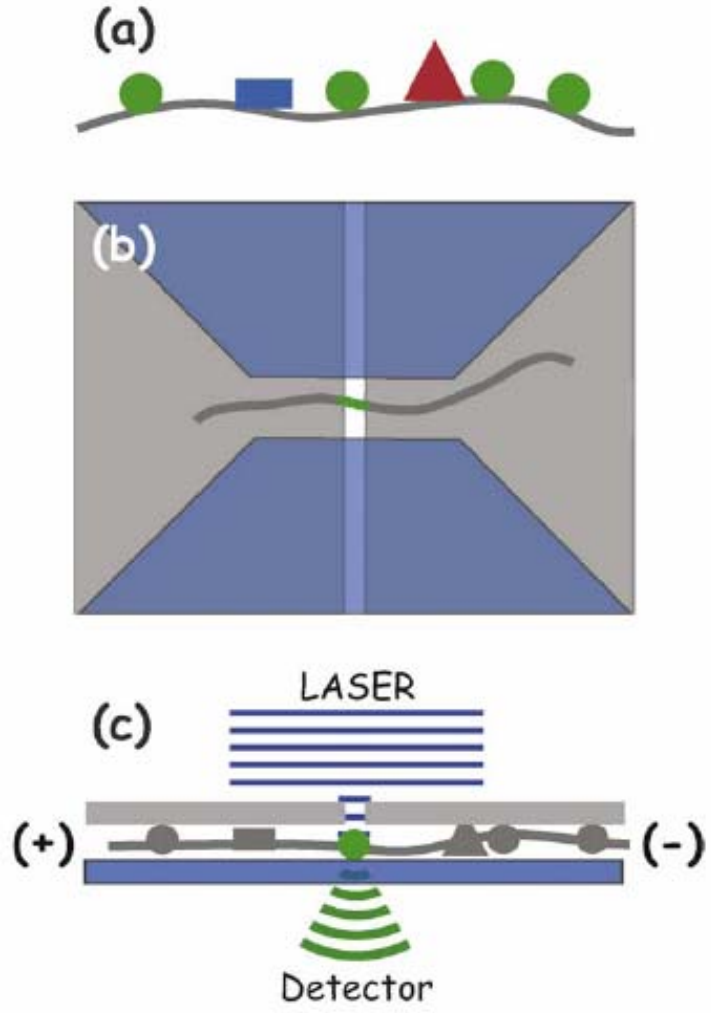
(a)
(b)
(c)
LASER
(+)
(-)
Detector

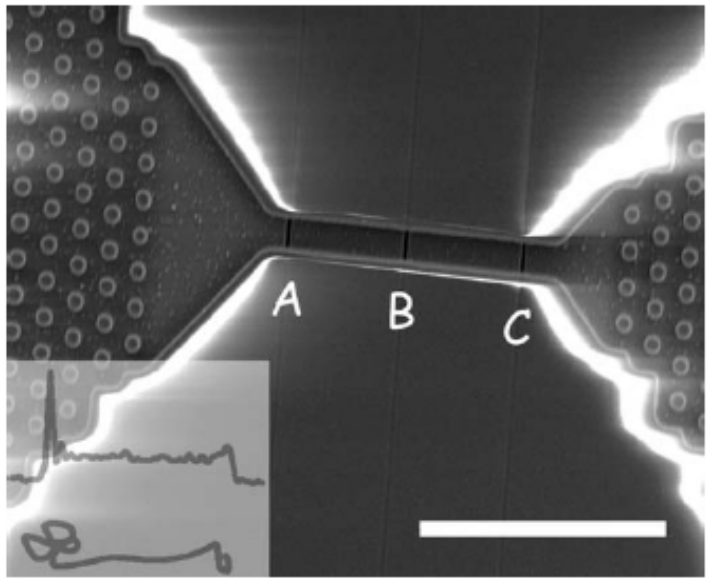
A
B
C

Separation of Long DNA Molecules in a Microfabricated Entropic Trap Array

12 MAY 2000 VOL 288 SCIENCE

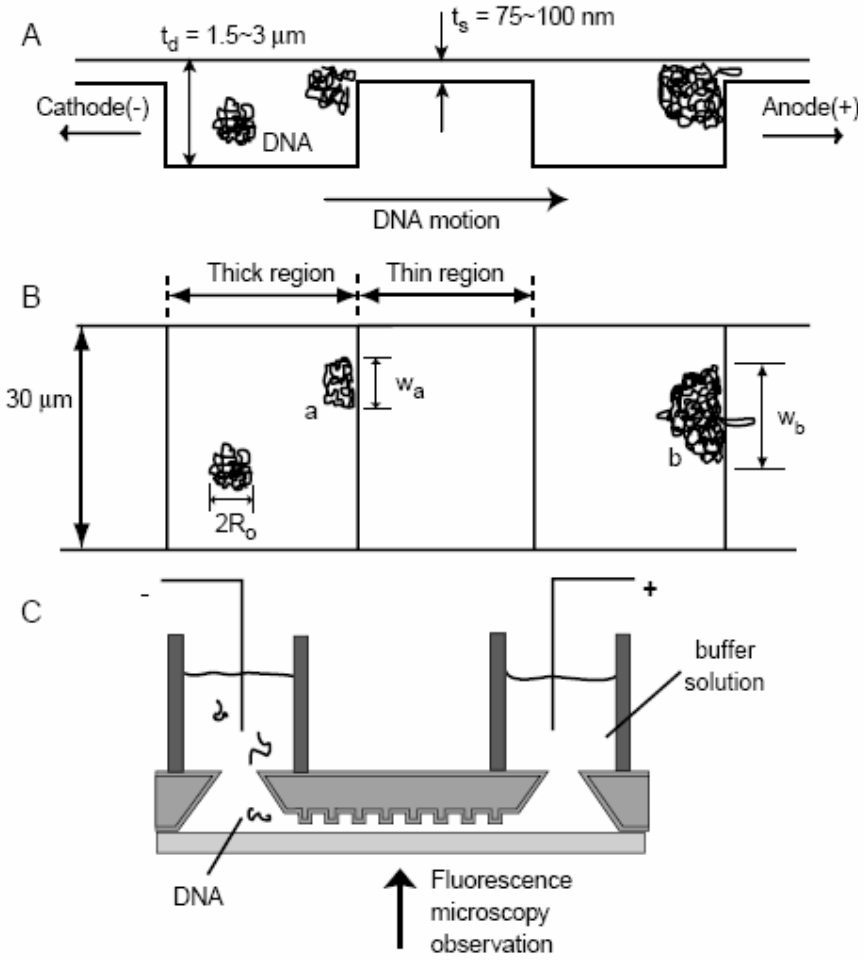

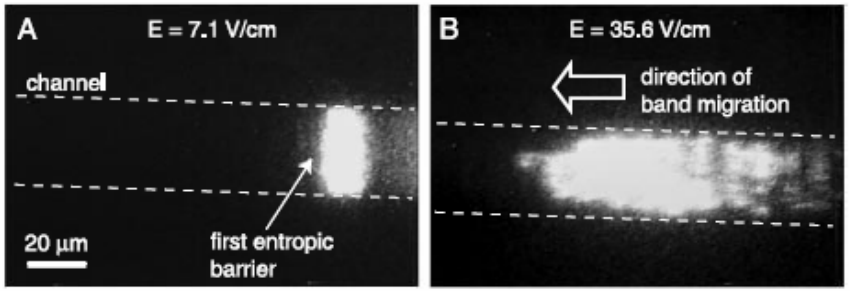

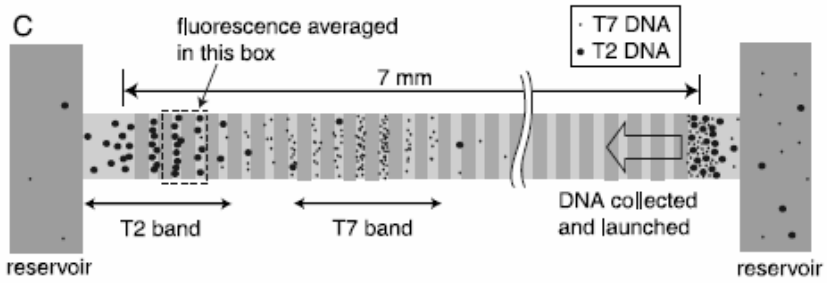

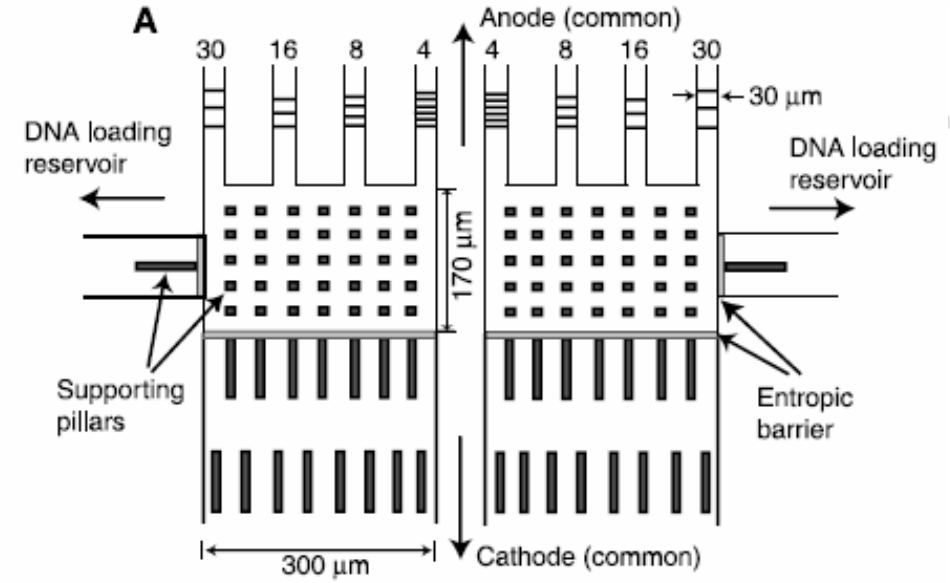
A
Anode (common)
30
16
8
4
4
8
16
30
30 µm
DNA loading reservoir
DNA loading reservoir
170 µm
Supporting pillars
Entropic barrier
300 µm
Cathode (common)

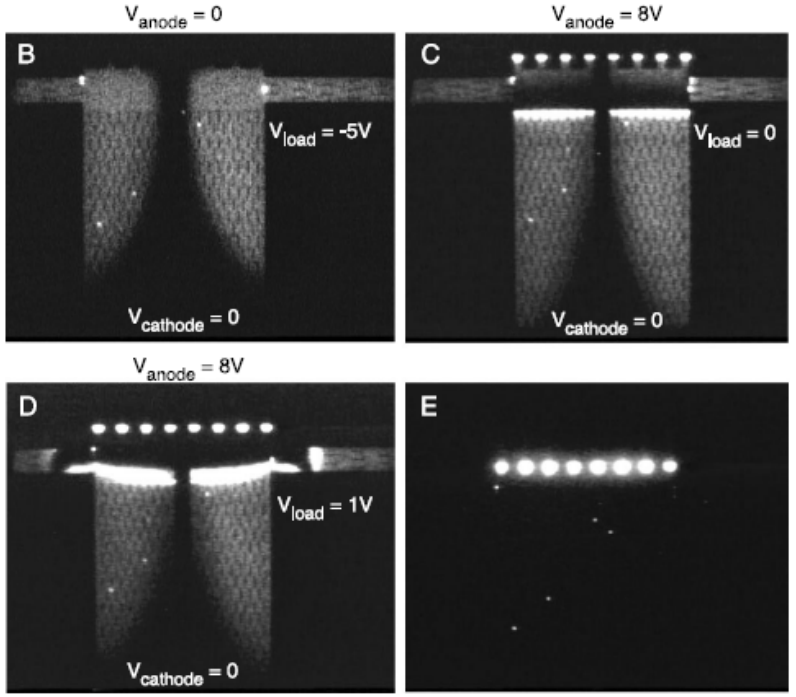
V anode = 0
B
V load = -5V
V cathode = 0
V anode = 8V
C
V load = 0
V cathode = 0
V anode = 8V
D
V load = 1V
V cathode = 0
E

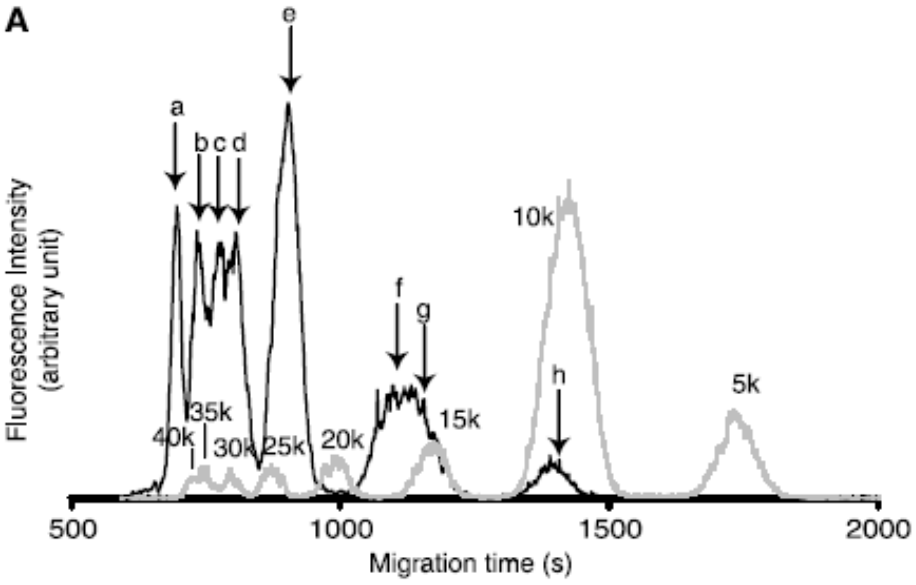
A
a
b c d
e
f
g
h
10k
5k
40k
35k
30k
25k
20k
15k
Fluorescence Intensity (arbitrary unit)
500
1000
1500
2000
Migration time (s)

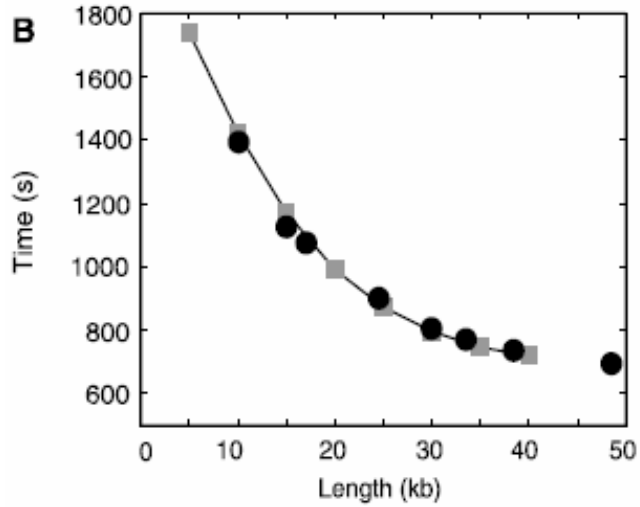
B
1800
1600
1400
1200
1000
800
600
Time (s)
0
10
20
30
40
50
Length (kb)

Nanofilter array chip for fast gel-free biomolecule separation

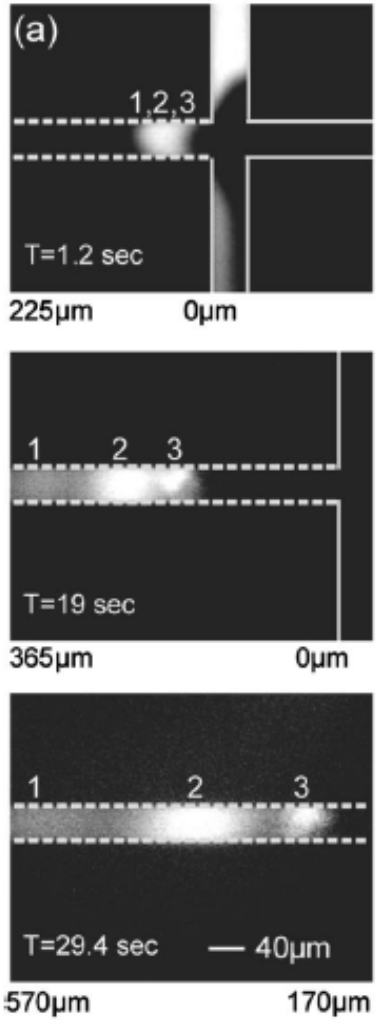

(b) SDS-Protein

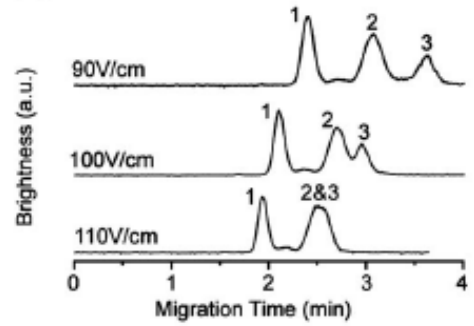

	$R_{S,12}$	$R_{S,23}$	N_1	H_1	N_1/L
90V/cm	2.16	1.61	1523	3.28	$3X10^5$

(c) dsDNA

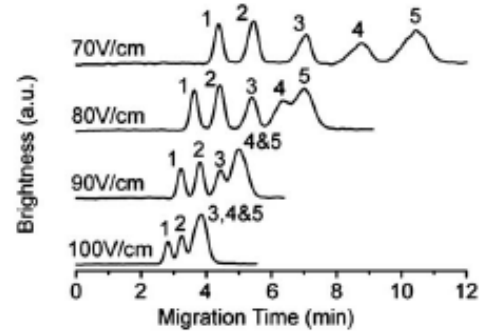

	μ_1	μ_2	μ_5	$R_{S,12}$	$R_{S,25}$
70V/cm	2.72	2.17	1.14	2.17	5.41
100V/cm	2.95	2.57	2.17	1.14	1.05

APPLIED PHYSICS LETTERS **87**, 263902 (2005)

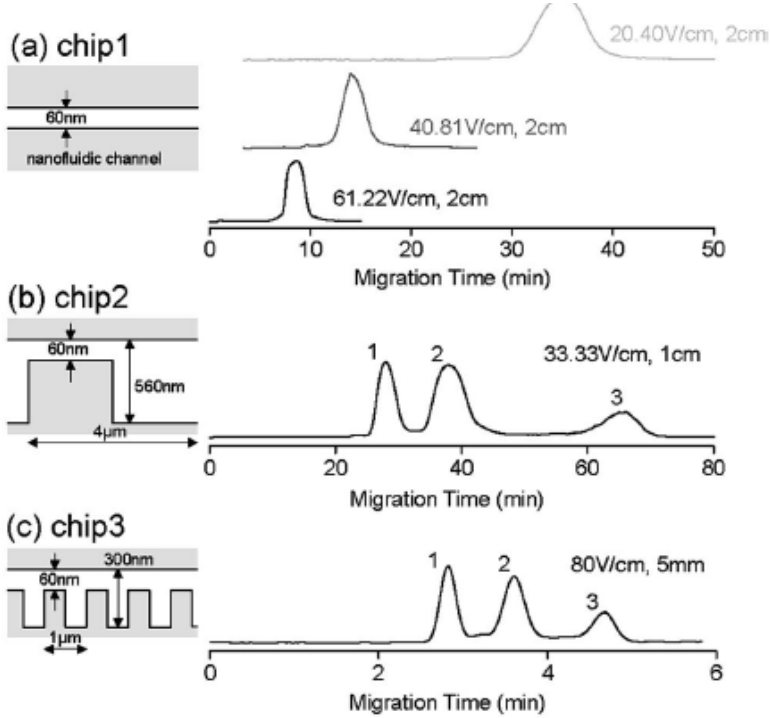

PRL 97, 018103 (2006)

Molecular Sieving in Periodic Free-Energy Landscapes Created by Patterned Nanofilter Arrays

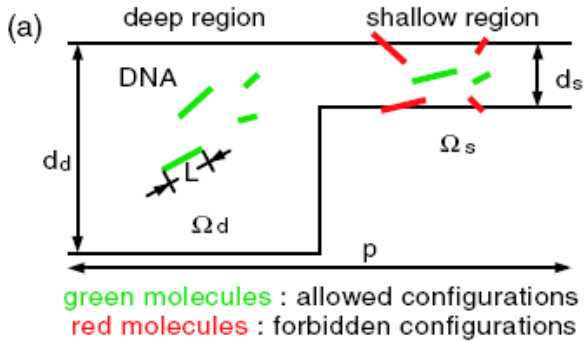

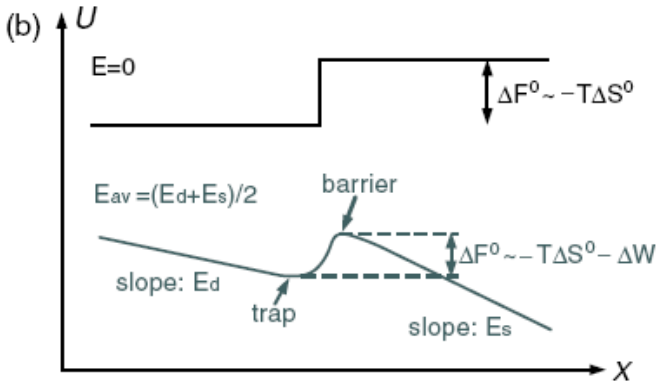

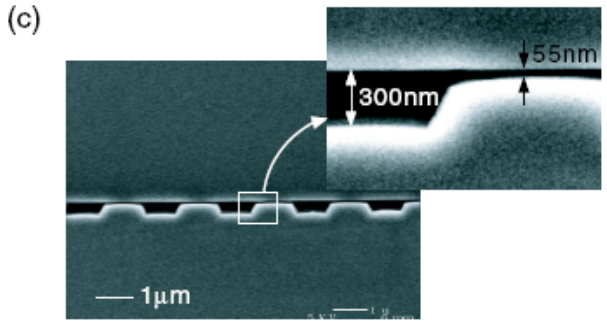

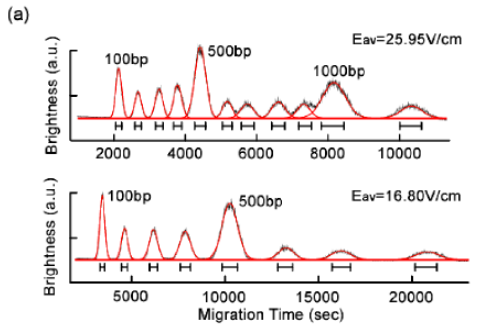

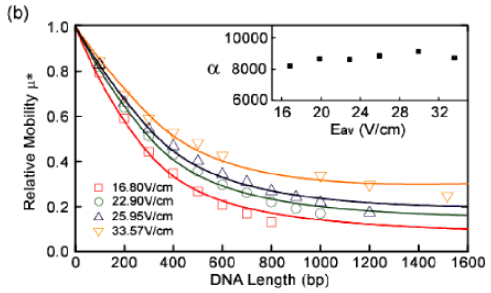

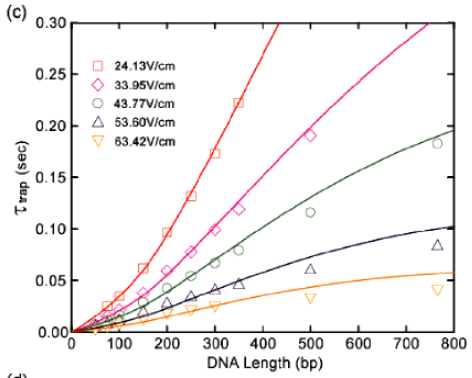

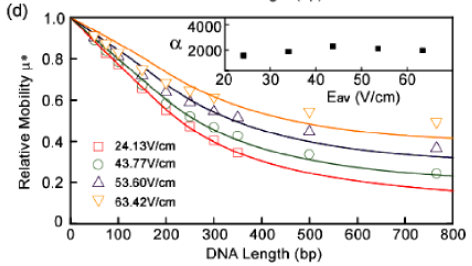

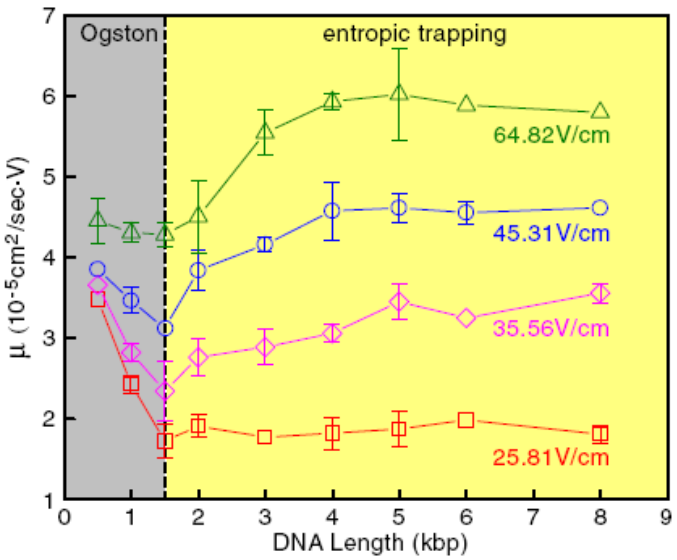

A patterned anisotropic nanofluidic sieving structure for continuous-flow separation of DNA and proteins

nature nanotechnology | VOL 2 | FEBRUARY 2007

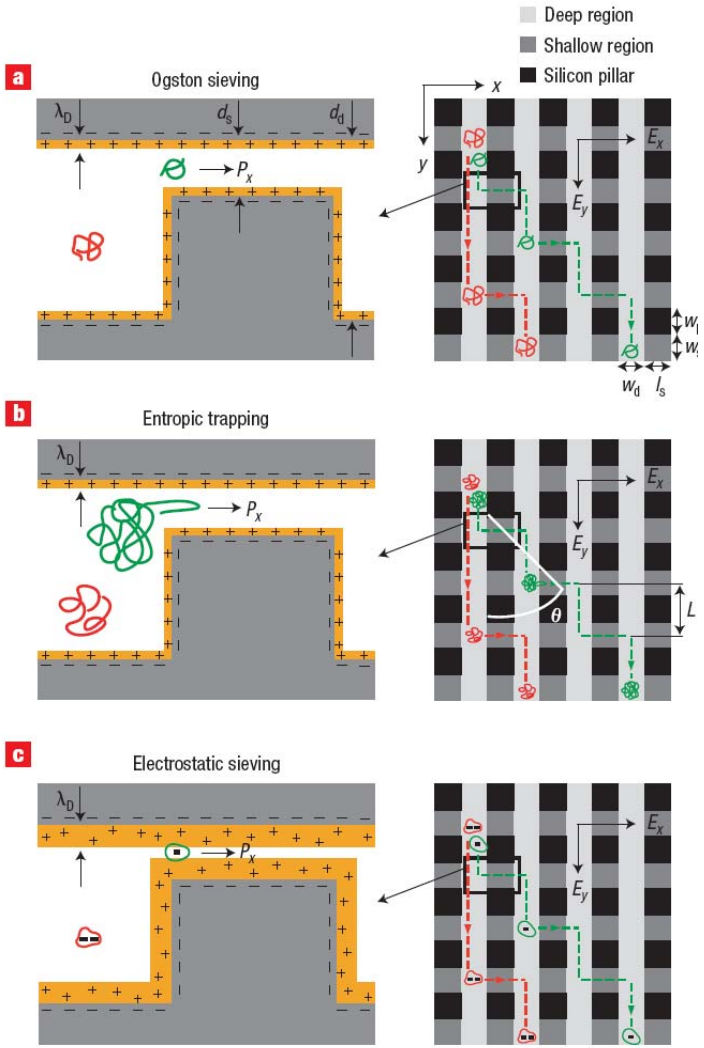

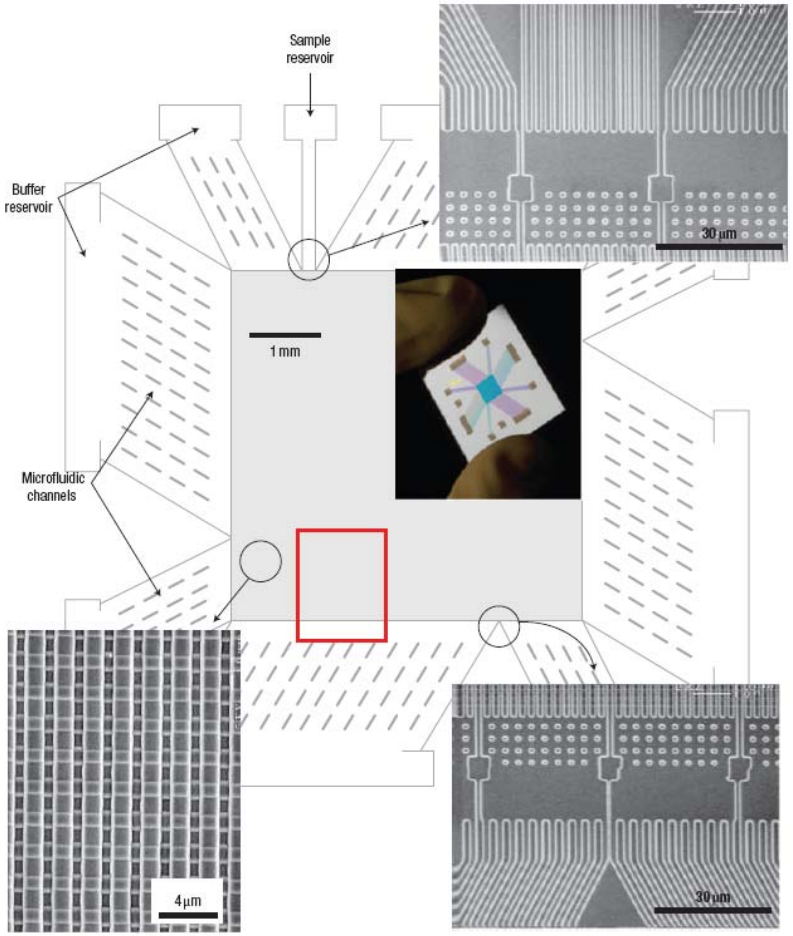

Sieving

- Ogston sieving
  - R < d
- Entropic trapping
  - R>d
- Electrostatic sieving
  - Debye length

- pI < pH ➔ positively charged
- pI > pH ➔ negatively charged

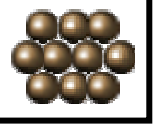

DNA Length

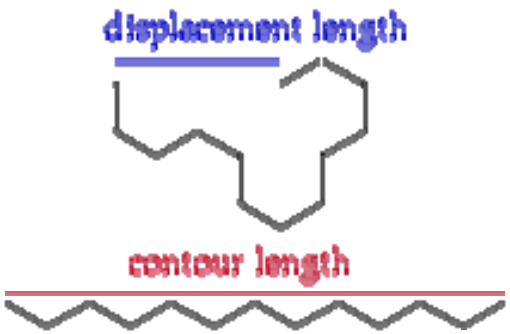

- Contour length
- Persistence length
  - The **persistence length** is a basic mechanical property quantifying the stiffness of a macromolecule of a polymer. It is defined as the length over which correlations in the direction of the tangent are lost.
- Radius of gyration
  - The **radius of gyration** *Rg* describes the distribution of particles (or infinitesimal elements) in a *D*-dimensional space by relating it to an equivalent distribution in a *D*-dimensional sphere, usually a circular (*D*=2) or spherical (*D*=3) distribution
- Kuhn length
  - The **Kuhn length** is a theoretical treatment of a real chain divided into *N* **Kuhn segments** with Kuhn length *b*, so that each Kuhn segments can be thought of as if they are freely joined with each other. The contour length $L = Nb$

Microfluidics - basics

J. P. Kutter
µ-TAS group
DTU

Electroosmotic flow

Interfacial phenomenon based on a charge separation which leads to a potential at the shear plane between a fixed and a mobile ion layer = ζ-potential

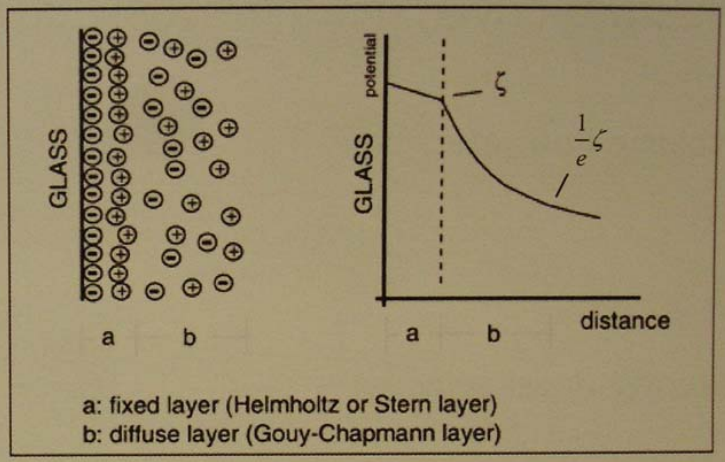

a: fixed layer (Helmholtz or Stern layer)
b: diffuse layer (Gouy-Chapmann layer)

Electroosmotic velocity

$$u_{eo} = \mu_{eo} E = \frac{\zeta \varepsilon}{4\pi\eta} E$$

μ_{eo}: electroosmotic mobility;
E: field strength; ε: dielectric constant

Double layer thickness

$$\delta = \sqrt{\frac{\varepsilon RT}{2F^2 z^2 c}}$$

R: gas constant; F: Faraday constant
z: charge; c: concentration

Debye Strength

$$I = \frac{1}{2}\sum_{i=1}^{n} c_i z_i^2$$

1 M NaCl => 0.5*1*1^2+0.5*1*1^2=1M

$$\lambda_D = \sqrt{\frac{\varepsilon_0 \varepsilon_r k T}{2 N_A e^2 I}}$$

$$\varepsilon_0 = \frac{1}{c^2 \mu_0} \approx 8.8541878176 \times 10^{-12}\ \mathrm{F/m}\ (\text{or}\ \mathrm{C^2/(J\ m)}),$$

80.1

5x TBE => I = ~130 mM ➔ Debye Length = 0.84 nm
0.05 x TBE => I = 1.3 mM ➔ Debye Length = 8.4 nm

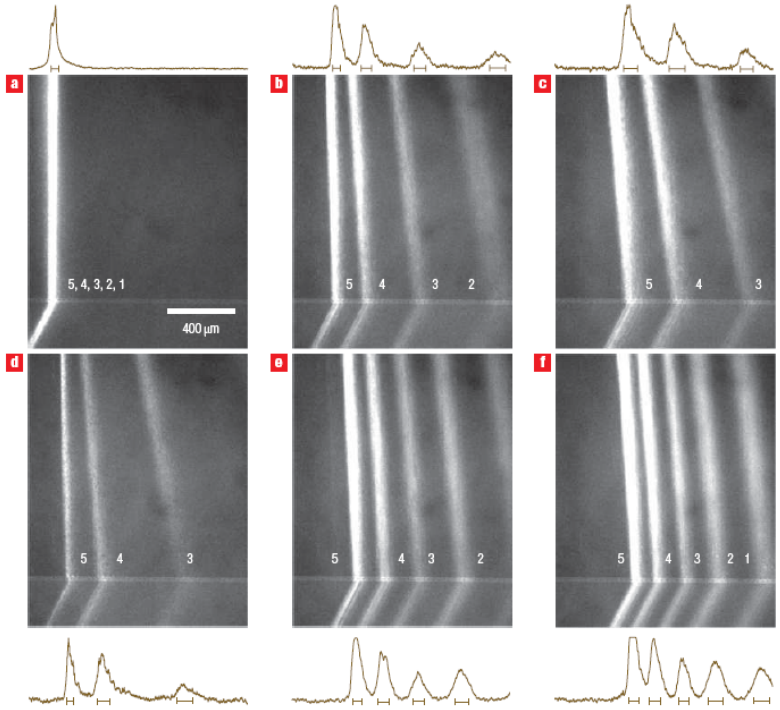
a
b
c
d
e
f
5, 4, 3, 2, 1
400 μm
5 4 3 2
5 4 3
5 4 3 2
5 4 3 2 1

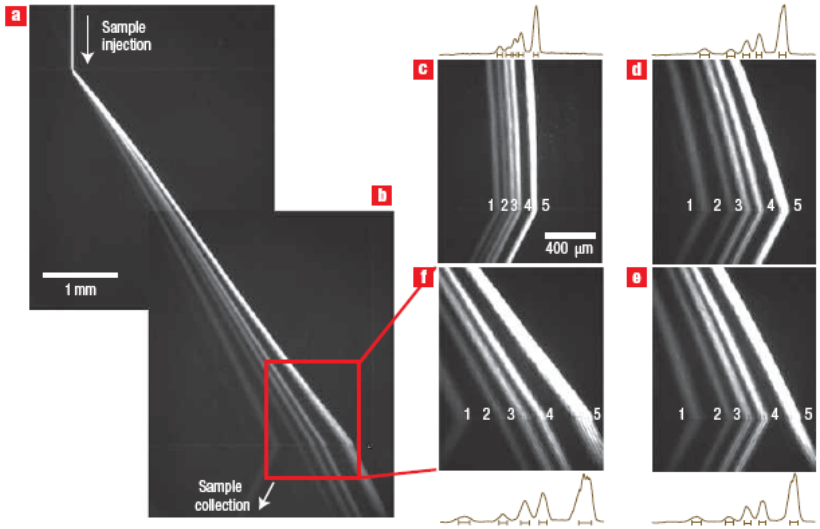
a
Sample injection
1 mm
Sample collection
b
c
1 2 3 4 5
400 μm
d
1 2 3 4 5
e
1 2 3 4 5
f
1 2 3 4 5

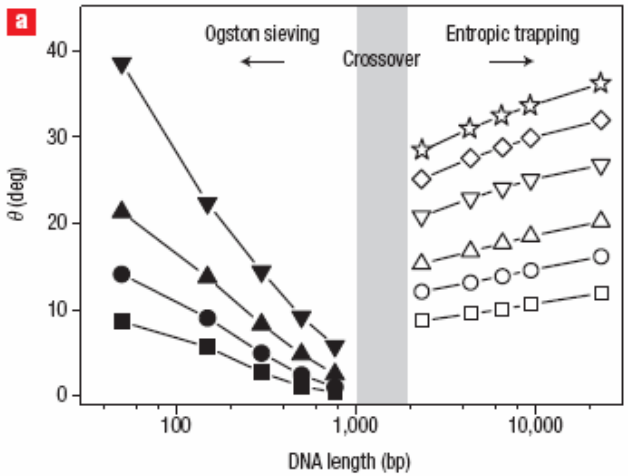
a
Ogston sieving
Crossover
Entropic trapping
θ (deg)
40
30
20
10
0
100
1,000
10,000
DNA length (bp)

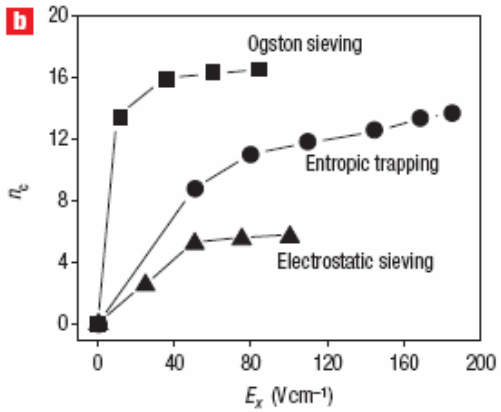
b
20
16
12
8
4
0
n_c
Ogston sieving
Entropic trapping
Electrostatic sieving
0
40
80
120
160
200
E_x (Vcm⁻¹)

Continuous-Flow pI-Based Sorting of Proteins and Peptides in a Microfluidic Chip Using Diffusion Potential

Anal. Chem. **2006,** *78,* 3528−3536

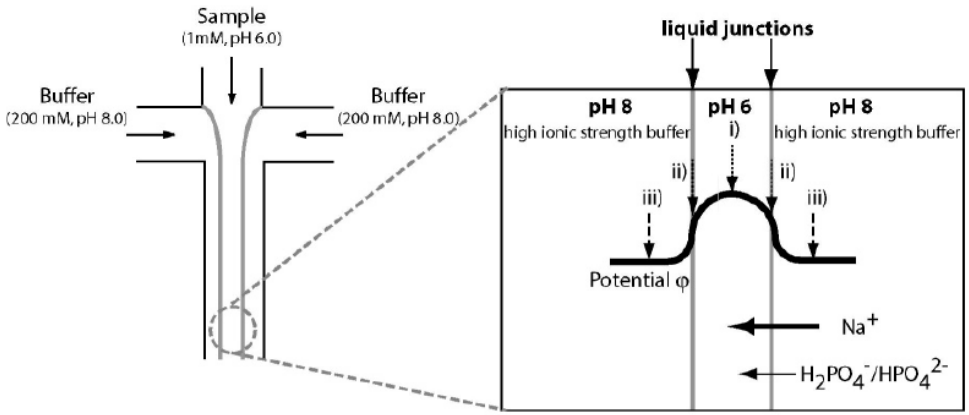

i) molecules with pI < pH 6.0 (always negative)
ii) molecules with pH 6.0 < pI < pH 8.0 (target)
iii) molecules with pI > pH 8.0 (always positive)

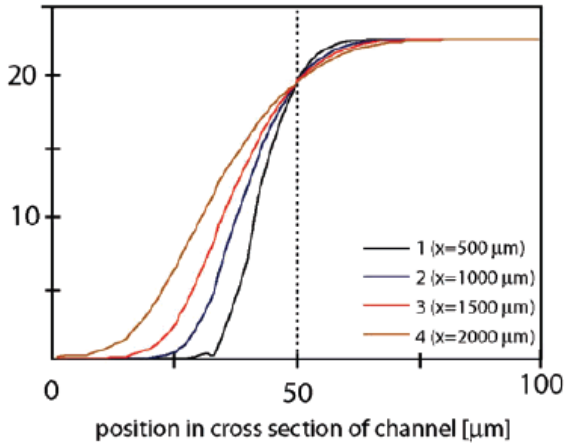

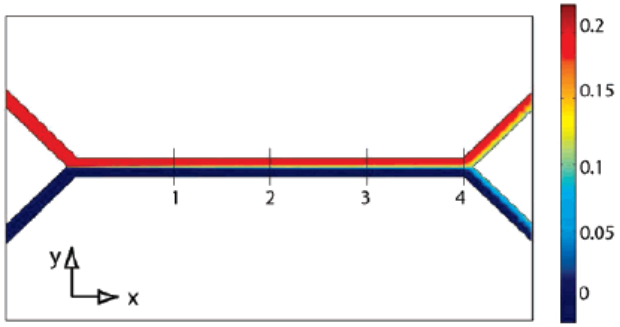

a) Tri-flow sorting scheme

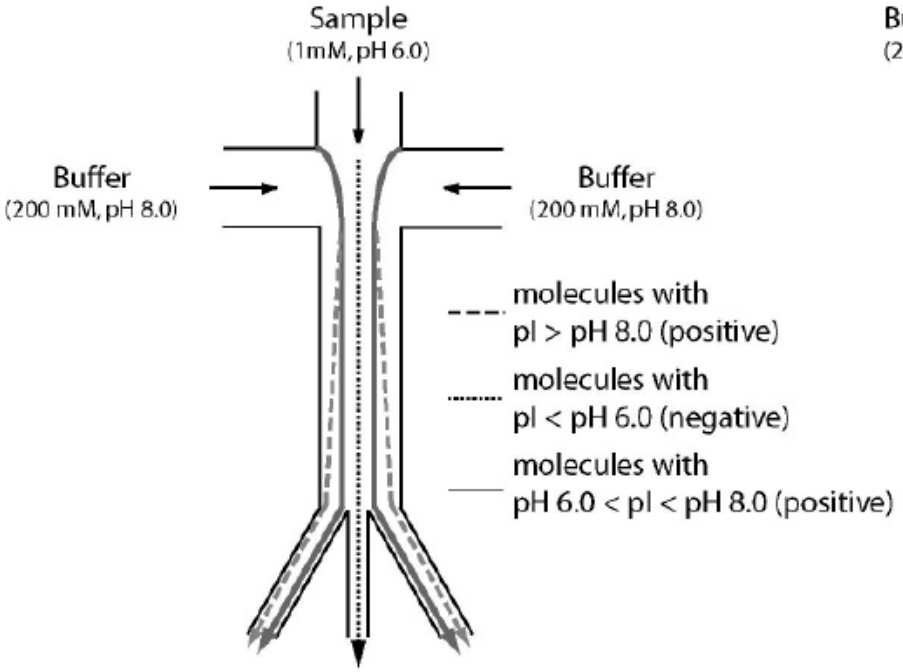

b) Binary-flow sorting scheme

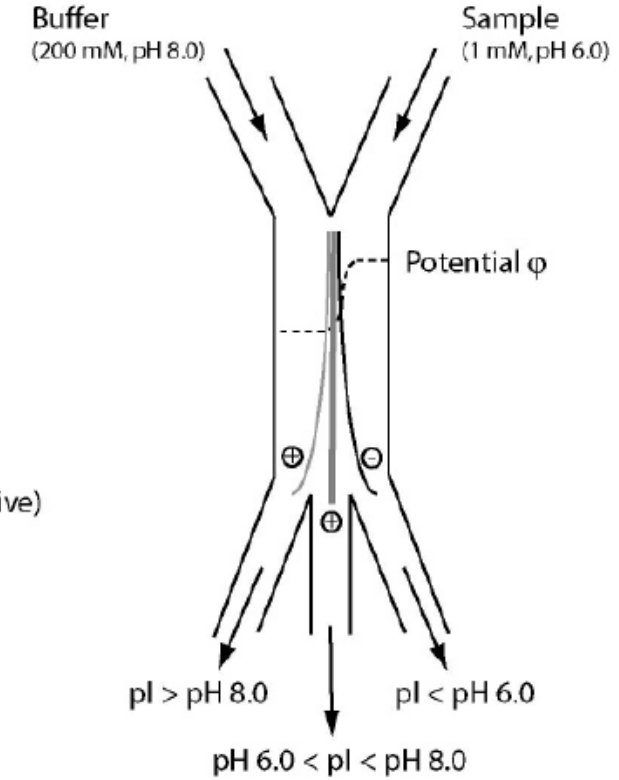

Chapter 26
SPR/SERS

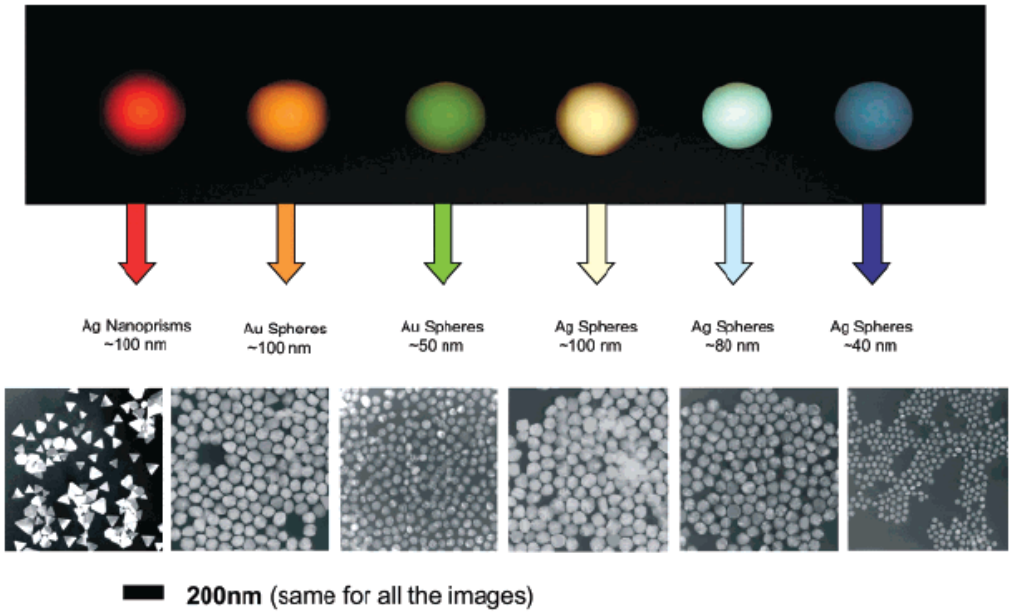

Figure 1. Sizes, shapes, and compositions of metal nanoparticles can be systematically varied to produce materials with distinct light-scattering properties.

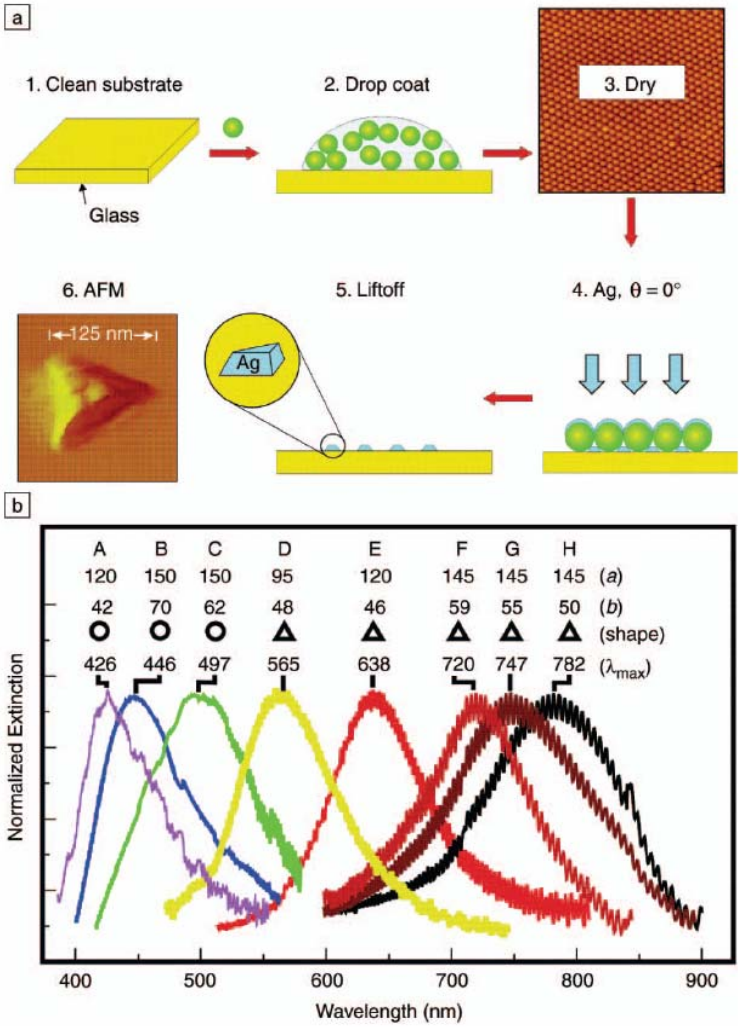

Figure 1. (a) Schematic representation of the nanosphere lithography (NSL) fabrication process. The AFM image in step 3 is 5 μm × 5 μm. (b) Size- and shape-tunable localized surface plasmon resonance spectra of various Ag nanoparticles (labeled A–H) fabricated by NSL. The wavelength of maximum extinction, λ_{max}, is changed by varying the in-plane width a *and out-of-plane height* b *of the nanoparticles.*

The simplest theoretical approach available for modeling the optical properties of nanoparticles is classical electrodynamics (i.e., solving Maxwell's equations with the metal dielectric constant taken from bulk measurements). For spherical particles, this leads to the following (Mie theory) expression for the extinction coefficient $E(\lambda)$ in the long-wavelength limit:[23]

$$E(\lambda) = \frac{24\pi N_A a^3 \varepsilon_m^{3/2}}{\lambda \ln(10)} \times \left[\frac{\varepsilon_i}{(\varepsilon_r + 2\varepsilon_m)^2 + \varepsilon_i^2} \right]. \quad (1)$$

Here, N_A is the areal density of the nanoparticles, a is the radius of the metallic nanosphere, ε_m is the dielectric constant of the medium surrounding the nanosphere (assumed to be a positive, real number), λ is the wavelength, and ε_r and ε_i are the real and imaginary parts of the metal dielectric function. This formula predicts a resonant peak when $\varepsilon_r = -2\varepsilon_m$, which for silver and gold occurs in the visible portion of the spectrum. In addition, any change in the dielectric constant of the medium (e.g., when molecules adsorb on the particle) leads to a change in the resonance wavelength.

$$\nabla \cdot \vec{H} = 0, \tag{4.}$$

$$\nabla \cdot \vec{E} = 0, \tag{5.}$$

$$\nabla \times \vec{E} + \frac{1}{c}\frac{\partial \vec{H}}{\partial t} = 0, \tag{6.}$$

$$\nabla \times \vec{H} - \frac{\varepsilon}{c}\frac{\partial \vec{E}}{\partial t} = 0, \tag{7.}$$

We consider an interface in the xy-plane between two half-infinite spaces, 1 and 2, of materials the optical properties of which are described by their complex frequency-dependent dielectric functions $\tilde{\varepsilon}_1(\omega)$ and $\tilde{\varepsilon}_2(\omega)$, respectively. We ignore magnetic materials. Surface polaritons can only be excited at such an interface if the dielectric displacement $\vec{D}$ of the electromagnetic mode has a component normal to the surface ($\|\vec{z}$) which can induce a surface charge density σ,

$$(\vec{D}_2 - \vec{D}_1) \cdot \vec{z} = 4\pi\sigma. \qquad 2.$$

S-polarized light propagating along the x-direction possesses only electric field components, $\vec{E}_i$, parallel to the surface ($\|$y-direction), i.e. transversal electric (TE) waves have $\vec{E}_i = (0, E_y, 0)$, and hence are unable to excite surface polaritons. Only p-polarized light (transversal magnetic TM) modes with $E = (E_x, 0, E_z)$, or, equivalently, $\vec{H} = (0, H_y, 0)$, can couple to such modes. The resulting surface electromagnetic wave, therefore, will have the following general form

$$\vec{A}_1 = \vec{A}_{10} e^{i(\vec{k}_{x1}\vec{x} + \vec{k}_{z1}\vec{z} - \omega t)} \text{ in medium } 1, z < 0 \qquad 3a.$$

and

$$\vec{A}_2 = \vec{A}_{20} e^{i(\vec{k}_{x2}\vec{x} - \vec{k}_{z2}\vec{z} - \omega t)} \text{ in medium } 2, z > 0, \qquad 3b.$$

where $\vec{A}$ stands for $\vec{E}$ and $\vec{H}$; $\vec{k}_{x1}$, and $\vec{k}_{x2}$ are the wavevectors in the x-direction; $\vec{k}_{z1}$, and $\vec{k}_{z2}$ those in the z-direction, i.e. normal to the interface; and ω is the angular frequency. Both fields $\vec{E}$ and $\vec{H}$ must fulfill the Maxwell equations:

with c being the speed of light in vacuo and ε the dielectric function of the material. The tangential components of $\vec{E}$ and $\vec{H}$ have to be equal at the interface, i.e.

$$E_{x1} = E_{x2} \tag{8.}$$

and

$$H_{y1} = H_{y2}. \tag{9.}$$

From Equation 8 it follows immediately that $k_{x1} = k_{x2} = k_x$. On the other hand, it follows from Equations 3 and 7 that

$$k_{z1} H_{y1} = \frac{\omega}{c} \varepsilon_1 E_{x1} \tag{10.}$$

and

$$k_{z2} H_{y2} = -\frac{\omega}{c} \varepsilon_2 E_{x2}. \tag{11.}$$

This leads to the only nontrivial solution if:

$$\frac{k_{z1}}{k_{z2}} = -\frac{\varepsilon_1}{\varepsilon_2}. \tag{12.}$$

Equation 12 indicates that surface electromagnetic modes can only be excited at interfaces between two media with dielectric constants of opposite sign.

Here we are dealing with the interface between a metal with its complex dielectric function ($\tilde{\varepsilon}_m = \varepsilon'_m + i\varepsilon''_m$) and a dielectric material ($\tilde{\varepsilon}_d = \varepsilon'_d + i\varepsilon''_d$), hence, with coupling the collective plasma oscillations of the nearly free electron gas in a metal to an electromagnetic field (5). These excitations are called plasmon surface polaritons (PSP) or surface plasmons, for short. From Equations 6, 7, 10, and 11 we obtain

$$k_x^2 + k_{zd}^2 = \left(\frac{\omega}{c}\right)^2 \varepsilon_d \qquad 13.$$

or

$$k_{zd} = \sqrt{\varepsilon_d \left(\frac{\omega}{c}\right)^2 - k_x^2}. \qquad 14.$$

With Equation 12 this leads to the dispersion relationships (i.e. the energy-momentum relation) for surface plasmons at a metal/dielectric interface:

$$k_x = \frac{\omega}{c}\sqrt{\frac{\varepsilon_m \cdot \varepsilon_d}{(\varepsilon_m + \varepsilon_d)}}. \qquad 15.$$

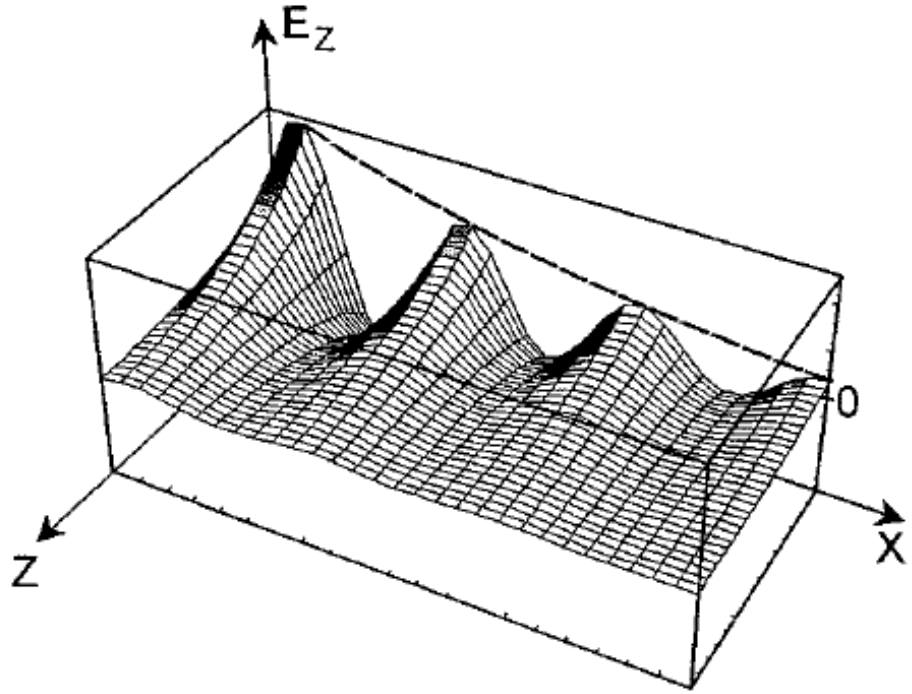

Figure 2 Schematic of the evanescent character of a surface plasmon mode excited at a metal/dielectric interface in the x-, y-plane propagating as a damped oscillatory wave in the x-direction. The electric field components along the z-direction, normal to the interface, decay exponentially, here shown for the E_z component.

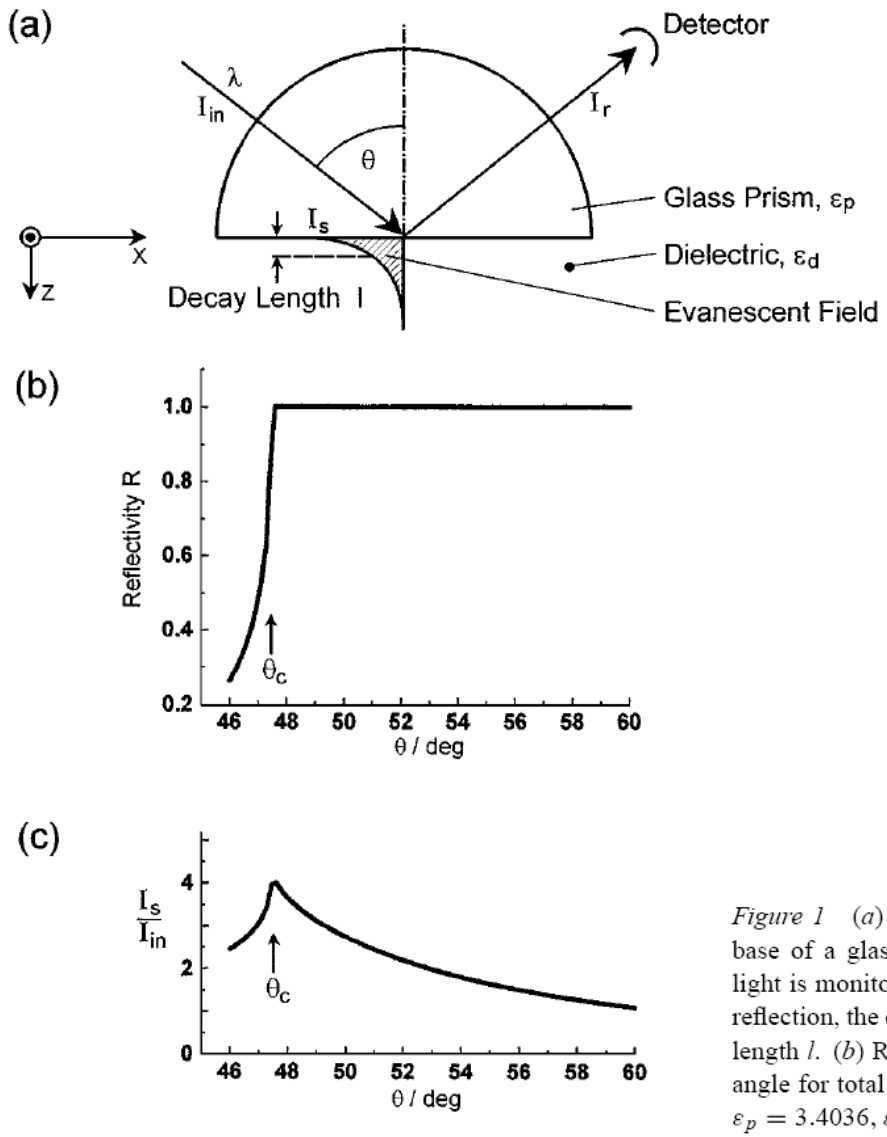

Figure 1 (*a*) Total internal reflection of a plane wave of wavelength λ and intensity I_{in} at the base of a glass prism with ε_p in contact with a dielectric medium of $\varepsilon_d < \varepsilon_p$. The reflected light is monitored with a detector. For incident angles $\theta > \theta_c$, the critical angle for total internal reflection, the evanescent field at the interface decays exponentially into the dielectric with a decay length l. (*b*) Reflectivity, i.e. I_r/I_{in}, as a function of the incident angle θ. θ_c denotes the critical angle for total internal reflection, and is given by $\sin\theta_c = \sqrt{\frac{\varepsilon_d}{\varepsilon_p}}$. The curve was calculated with $\varepsilon_p = 3.4036$, $\varepsilon_d = 1.778$. (*c*) Intensity enhancement, I_s/I_{in}, at the interface ($z = 0$) as a function of the incident angle θ.

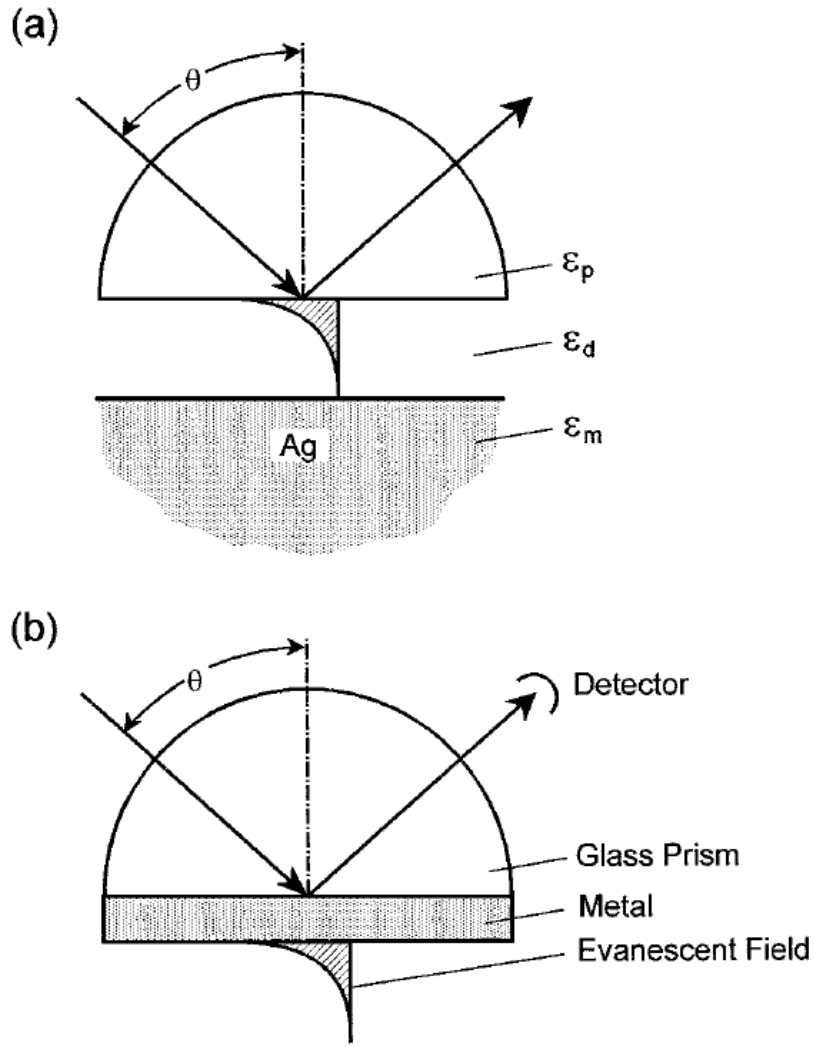

Figure 4 (*a*) The Otto configuration is based on the total internal reflection of a plane wave incident at an angle θ at the base of a prism. The evanescent tail of this inhomogeneous wave can excite PSP states at an Ag-dielectric interface, provided the coupling gap is sufficiently narrow. (*b*) Attenuated total internal reflection (ATR) construct for PSP excitation in the Kretschmann geometry. A thin metal film ($d \sim 50$ nm) is evaporated onto the base of the prism and acts as a resonator driven by the photon field incident at an angle θ.

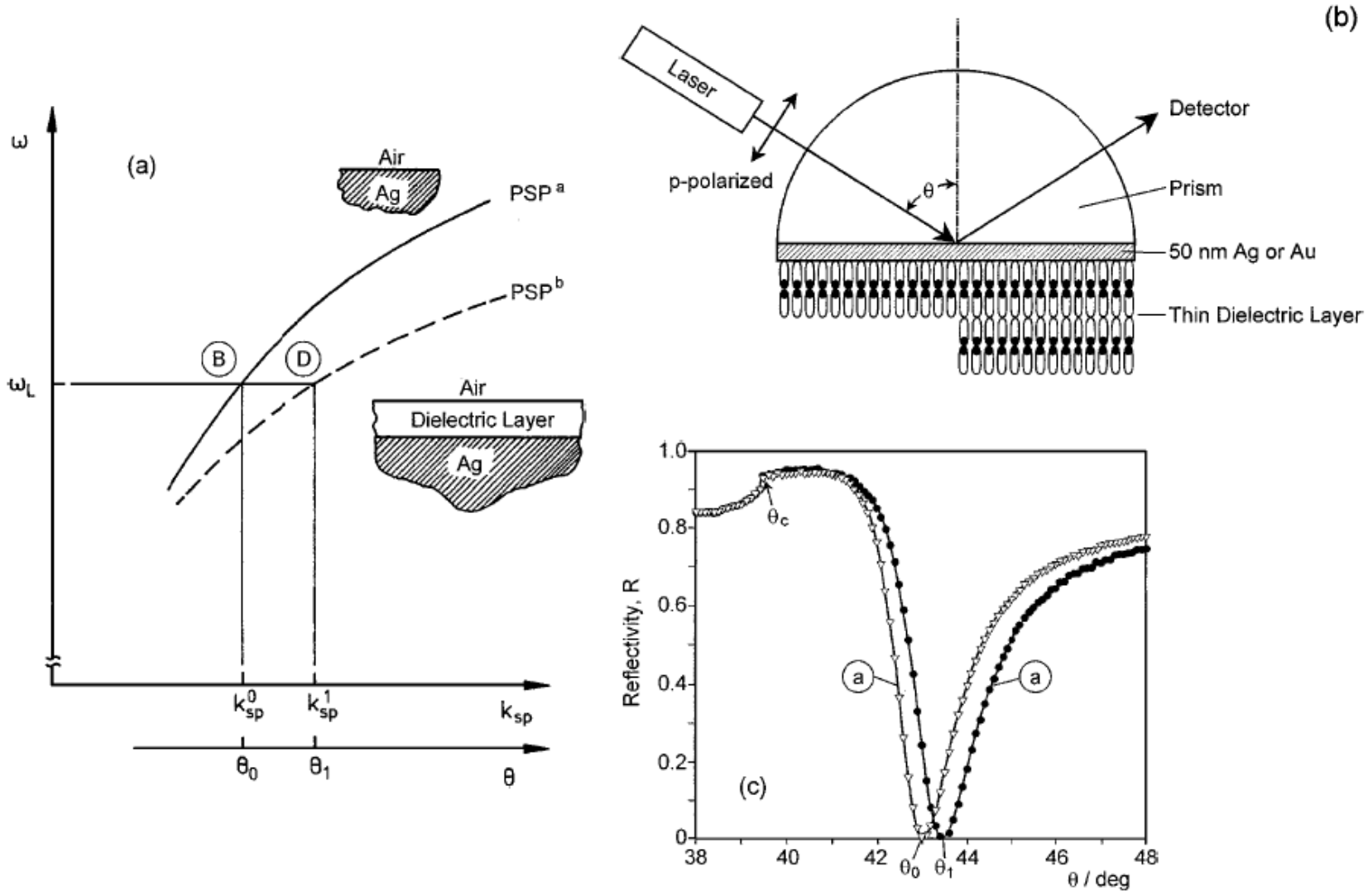

after self-assembling a monomolecular layer of HS-$(CH_2)_{21}$-OH. The symbols are experimental data points; the full curves are Fresnel fits with $\varepsilon_{BK7} = 2.29$, $\tilde{\varepsilon}_{Au} = -12.45 + i \cdot 1.3$, $d_{Au} = 46.9$ nm, $\varepsilon_{layer} = 2.1025$, $d_{layer} = 2.65$ nm. Data were taken at $\lambda = 633$ nm in air.

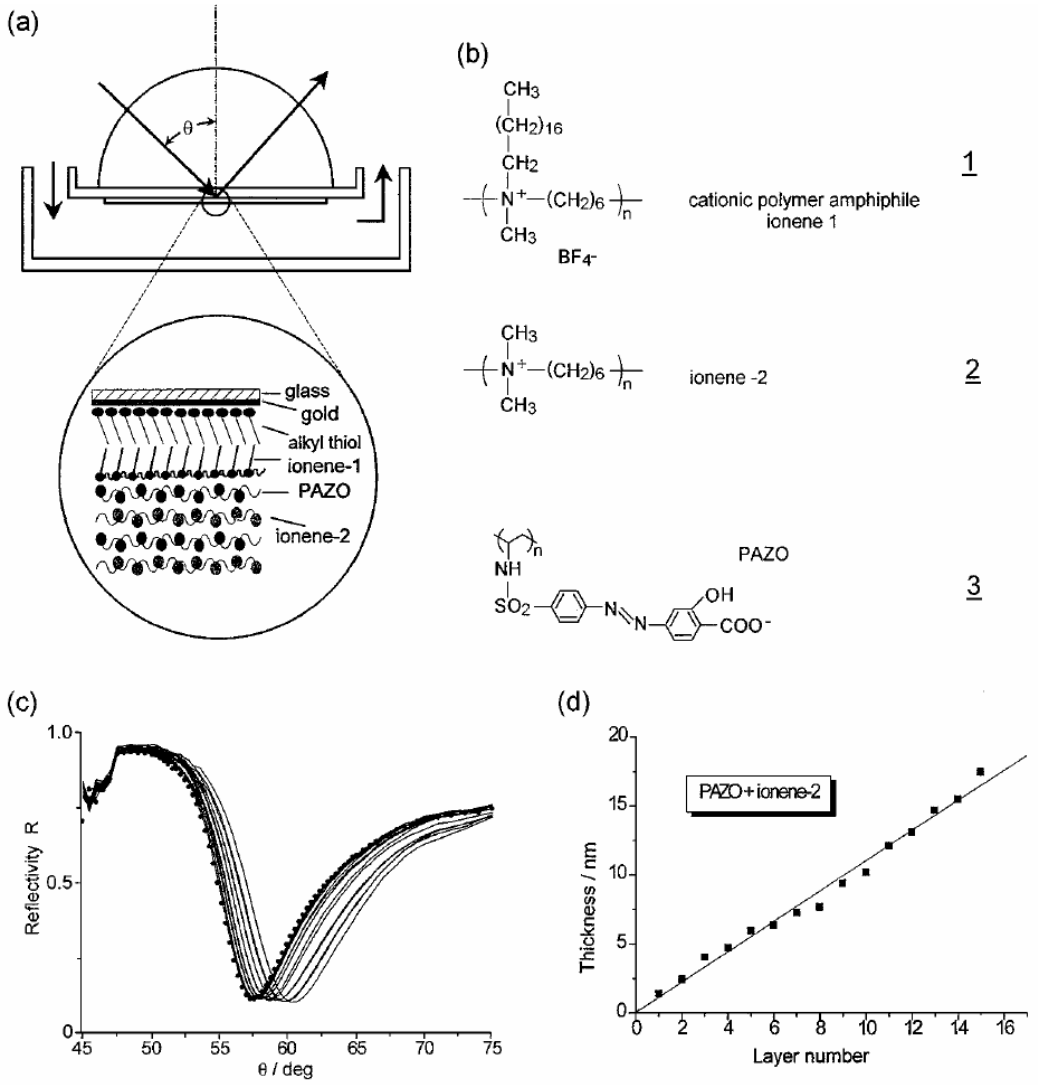

Figure 14 (*a*) Experimental construct for on-line surface plasmon optical observation of the alternating deposition of cationic and anionic polymers from solution to an Au substrate precoated by an alkyl thiol and an ionene-1 monolayer [refer to (*b*)]. The build-up architecture is given in the enlargement. (*b*) Structural formulas of the employed materials. (*c*) Series of ATR scans taken after each polyelectrolyte monolayer deposition. (*d*) Thickness increase as obtained from the ATR scans given in (*c*).

BIAcore X

The Corner Stones of Biacore Technology

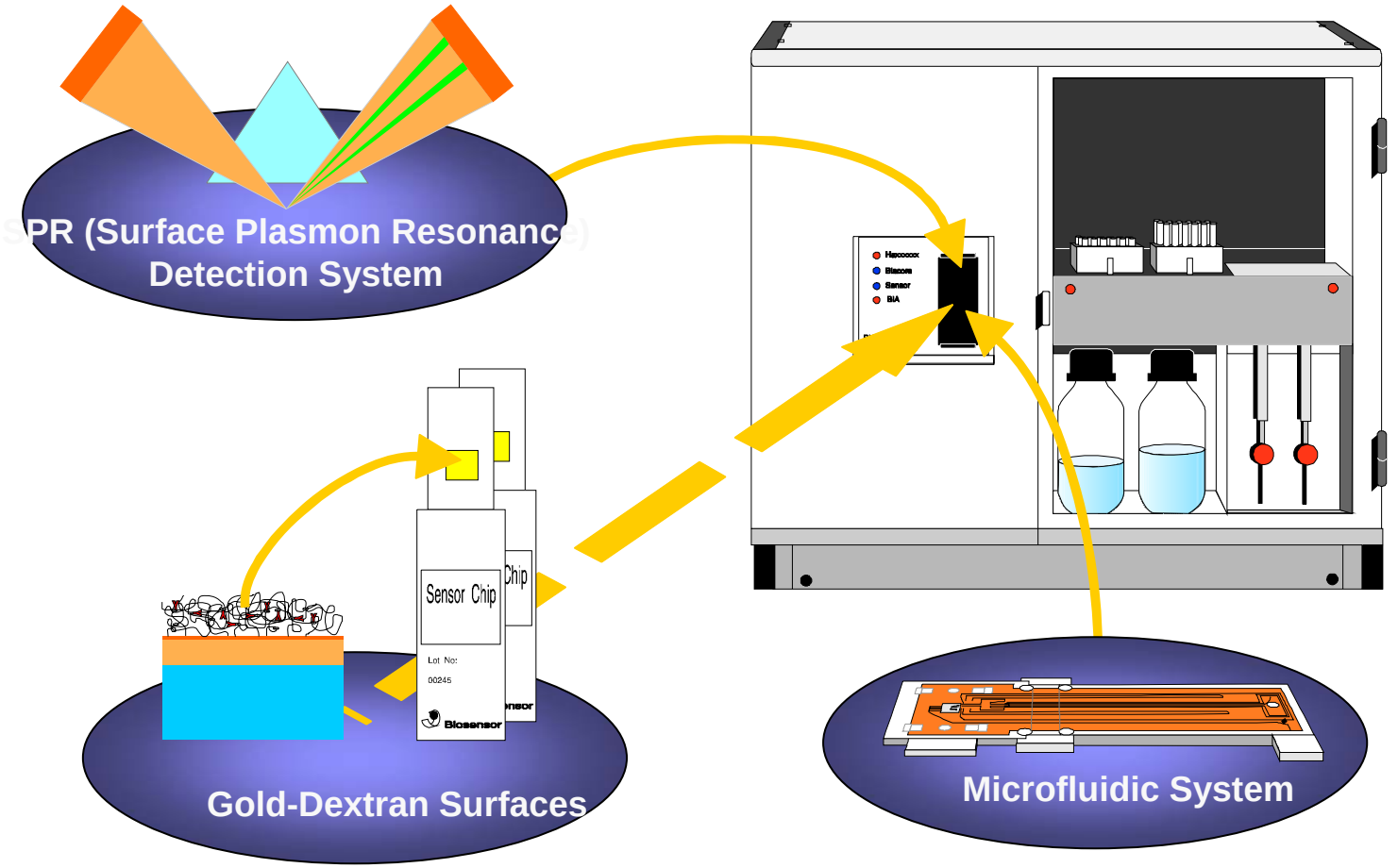

Biomolecular Binding in Real Time

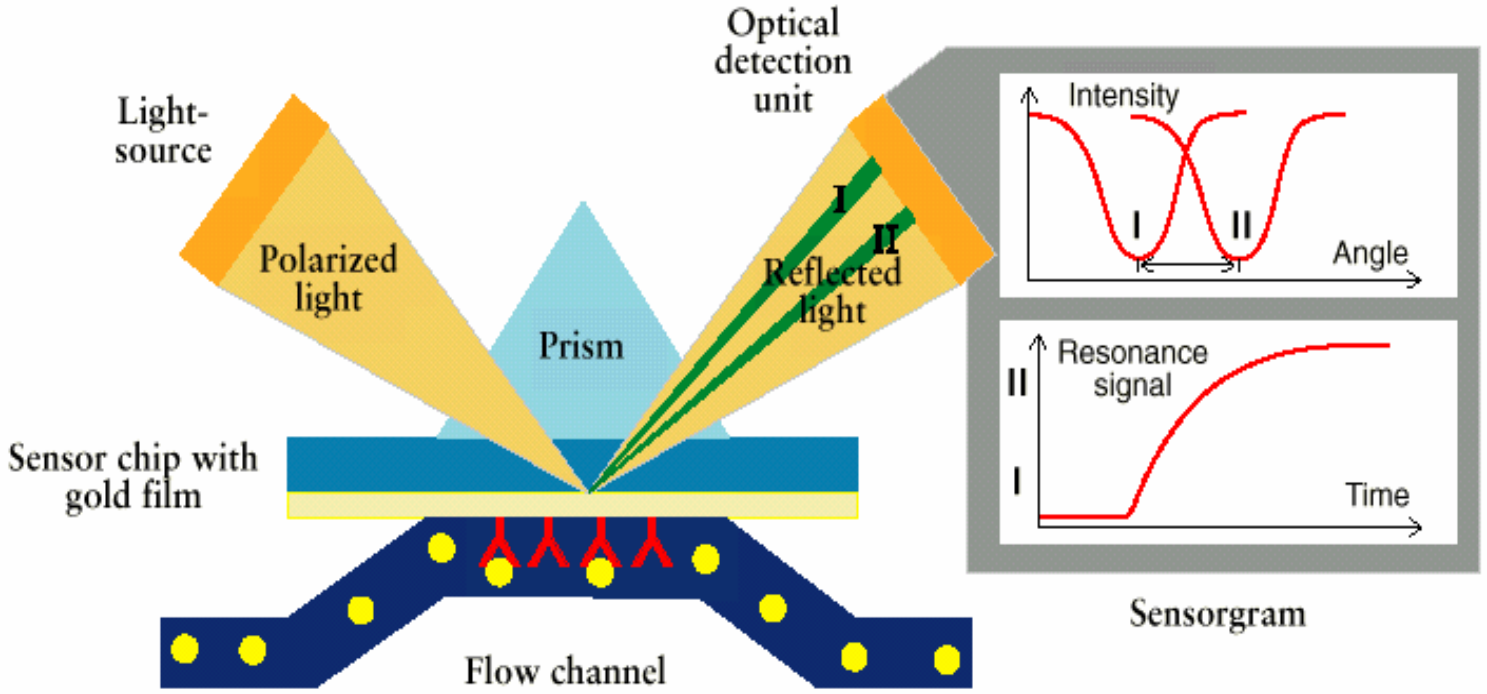

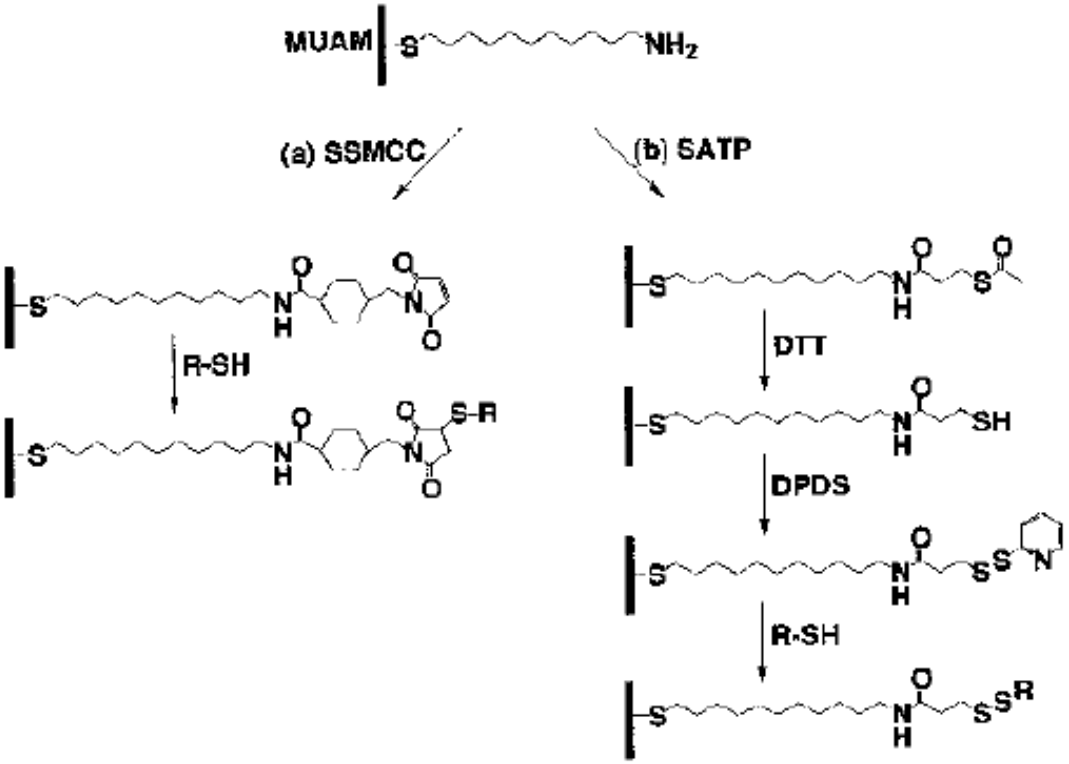

Figure 5.3 Surface attachment chemistry for the immobilization of thiol-modified DNA and cysteine-containing peptides: (a) The linker SSMCC is reacted with a well-packed self-assembled monolayer of 11-mercaptoundecylamine (MUAM) to create a maleimide-modified surface. The maleimide surface is then used to covalently attach thiol-modified DNA or cysteine-containing peptides. (b) In the second approach, SATP is reacted with MUAM to create a protected thiol surface. Upon deprotection with a basic solution containing DTT, the free sulfhydryl is reacted with dipyridyl disulfide to create a pyridyl disulfide surface. Thiol–disulfide exchange reactions are used to couple thiol-containing biomolecules to the surface.

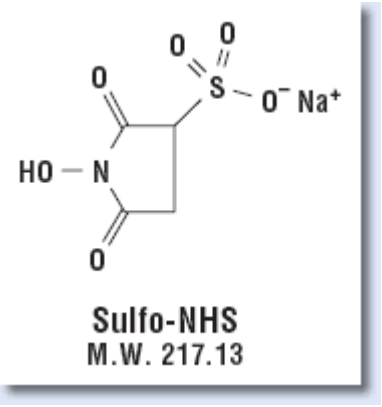

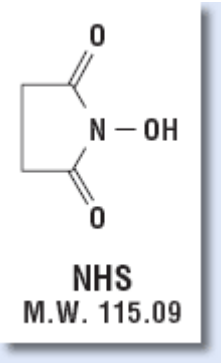

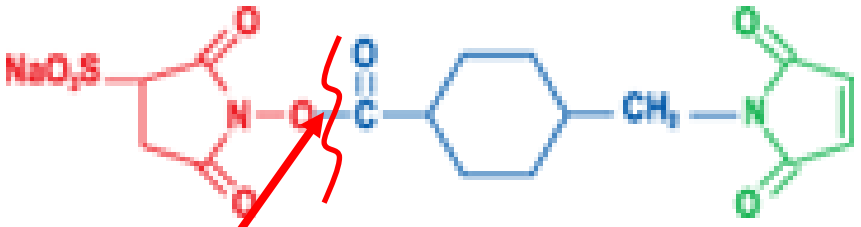

SulfoSuccinimidyl-4-(N-Maleimidomethyl)Cyclohexane-1-Carboxylate
SSMCC

The most popular NH_2- and SH- crosslinker

N-hydroxysuccinimide

NH_2 => amide

$R_1NH_2 + NHS\text{-}R_2 = >R_1NHC{=}OR_2$

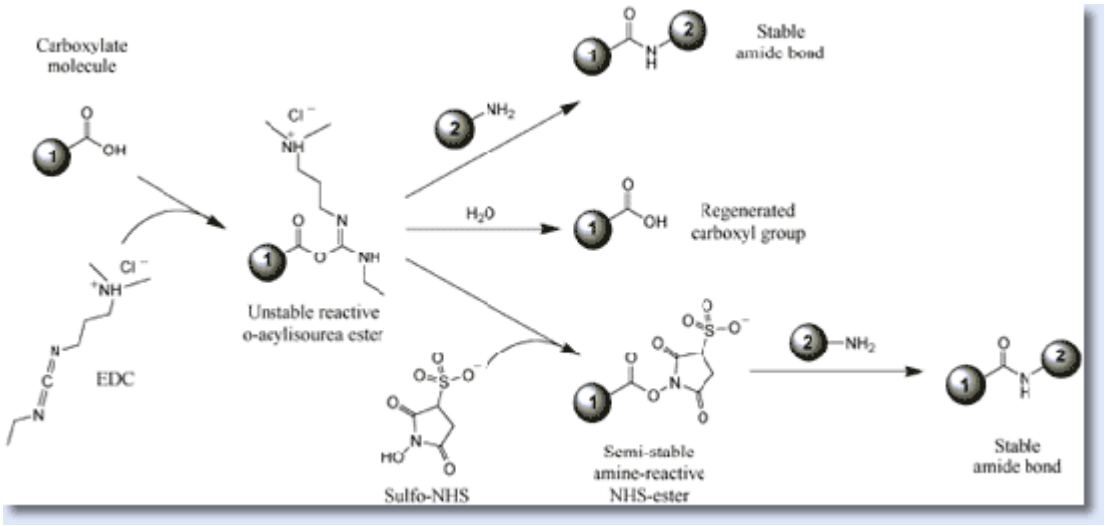

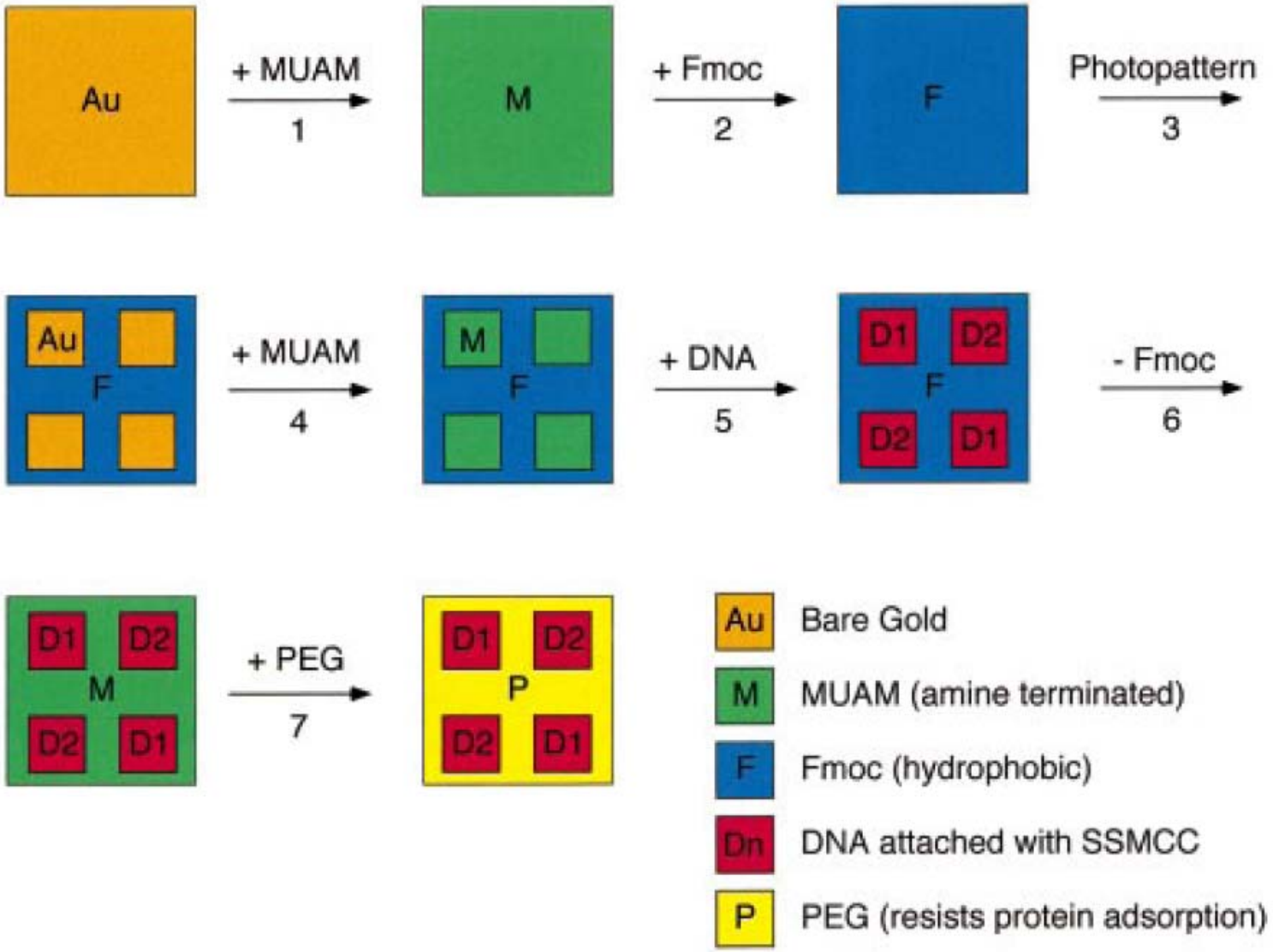

Figure 1. Fabrication scheme for the construction of multi-element DNA arrays. A clean gold surface is reacted with the amine-terminated alkanethiol MUAM, and subsequently reacted with Fmoc-NHS to create a hydrophobic surface. This surface is then exposed to UV radiation through a quartz mask and rinsed with solvent to remove the MUAM+Fmoc from specific areas of the surface, leaving bare gold pads. These bare gold areas on the sample surface are filled in with MUAM, resulting in an array of MUAM pads surrounded by a hydrophobic Fmoc background. Solutions of DNA are then delivered by pipet onto the specific array locations and are covalently bound to the surface via the bifunctional linker SSMCC. In the final two steps, the Fmoc-terminal groups on the array background are removed and replaced by PEG groups which prohibit the nonspecific binding of analyte proteins to the background.

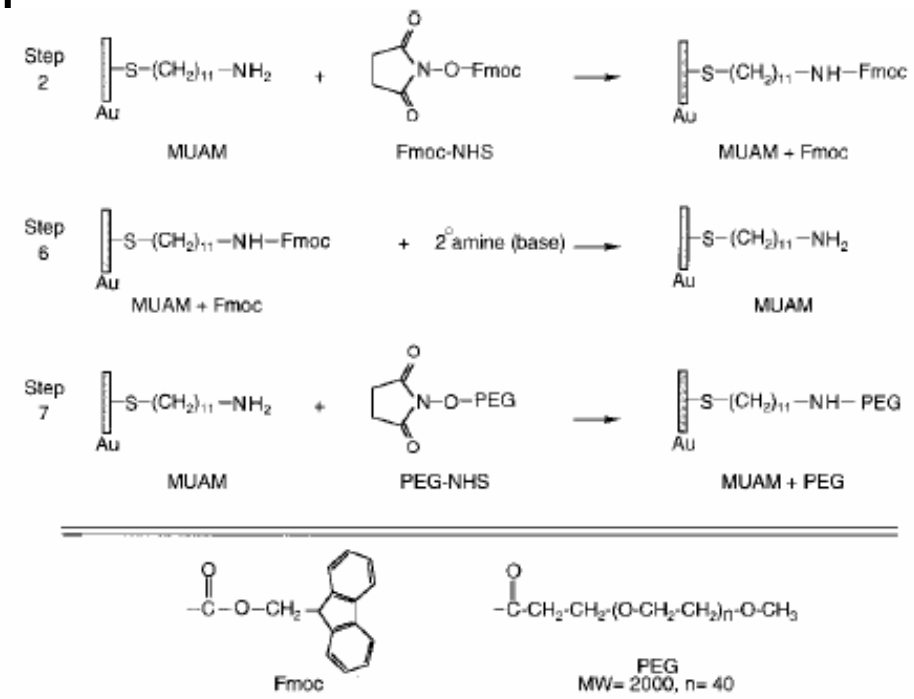

Figure 2. Surface reaction scheme showing the steps involved in the reversible modification of the array background. (Step 2) The starting amine-terminated alkanethiol surface (MUAM) is reacted with the Fmoc-NHS protecting group to form a carbamate linkage thus creating a hydrophobic Fmoc-terminated surface. (Step 6) After DNA immobilization (see Figure 3), the hydrophobic Fmoc group is removed from the surface with a basic secondary amine, resulting in the return of the original MUAM surface. (Step 7) In the final array fabrication step, the deprotected MUAM is reacted with PEG-NHS to form an amide bond that covalently attaches PEG to the array surface.

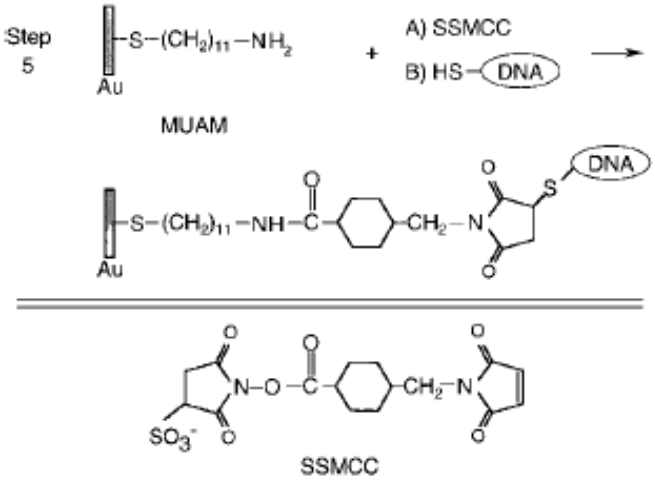

Figure 3. Surface reaction scheme showing the immobilization of thiol-terminated DNA to the array surface. In Step 5 of the DNA array fabrication, the heterobifunctional linker SSMCC is used to attach 5′-thiol modified oligonucleotide sequences to reactive pads of MUAM. This linker contains an NHSS ester functionality (reactive toward amines) and a maleimide functionality (reactive toward thiols). The surface is first exposed to a solution of the linker, whereby the NHSS ester end of the molecule reacts with the MUAM surface. Excess linker is rinsed away and the array surface is then spotted with 5′-thiol-modified DNA that reacts with the maleimide groups forming a covalent bond to the surface monolayer.

Surface Plasmon Resonance Imaging

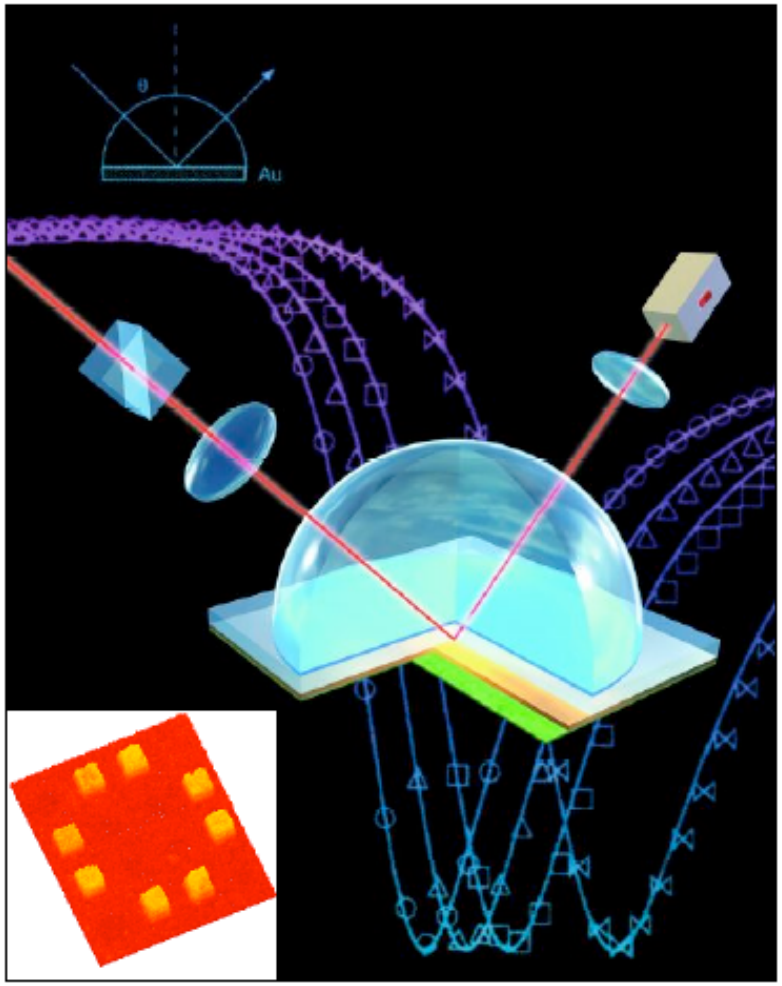

SPR imaging is a label-free method for monitoring bioaffinity interactions at gold surfaces in an array format.

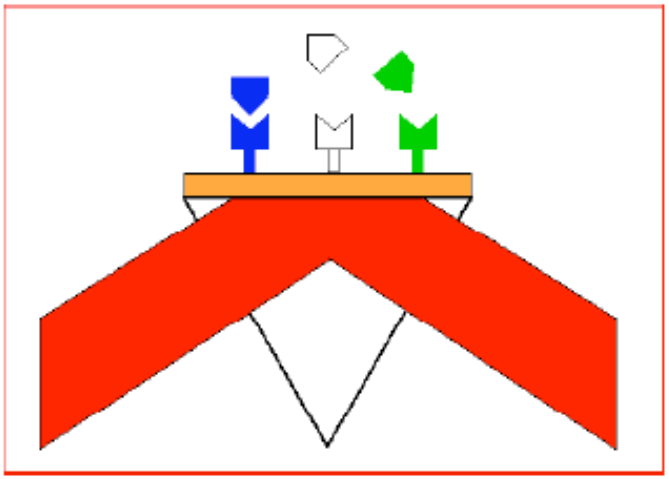

Robert M. Corn, UCI

Review: Applied Spectroscopy, **57** 320A-332A (2003).

UCIrvine
University of California, Irvine

DNA/DNA

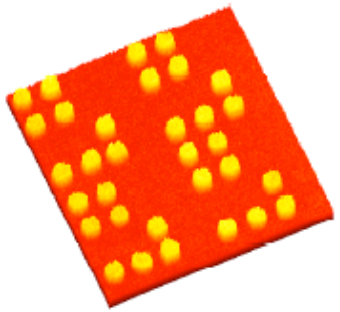

Protein/Peptide

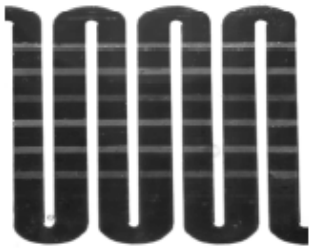

Protein/Protein

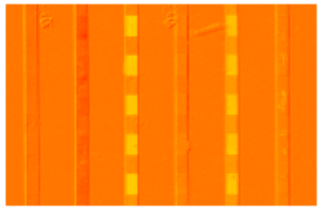

Screening of Biomolecular Arrays with SPR Imaging

RNA/DNA

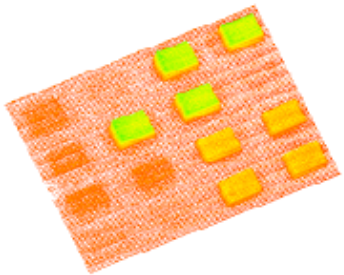

Protein/DNA

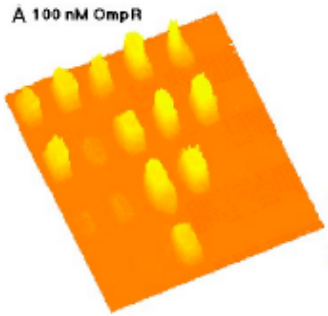

Protein/
Carbohydrate

Concanavalin A

UCIrvine
University of California, Irvine

SPR Imaging Apparatus

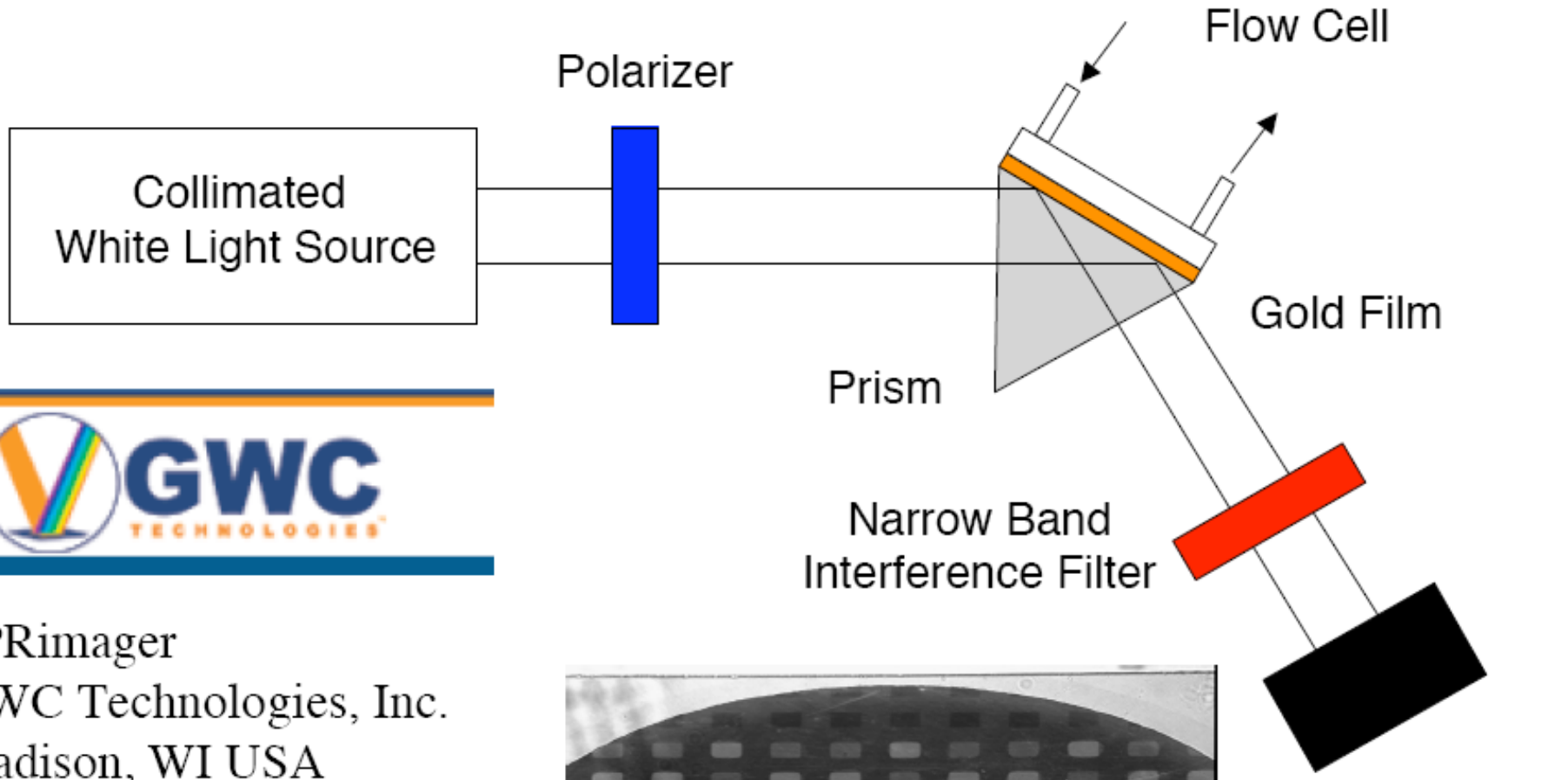

SPRimager
GWC Technologies, Inc.
Madison, WI USA

www.gwctechnologies.com

Raw Image

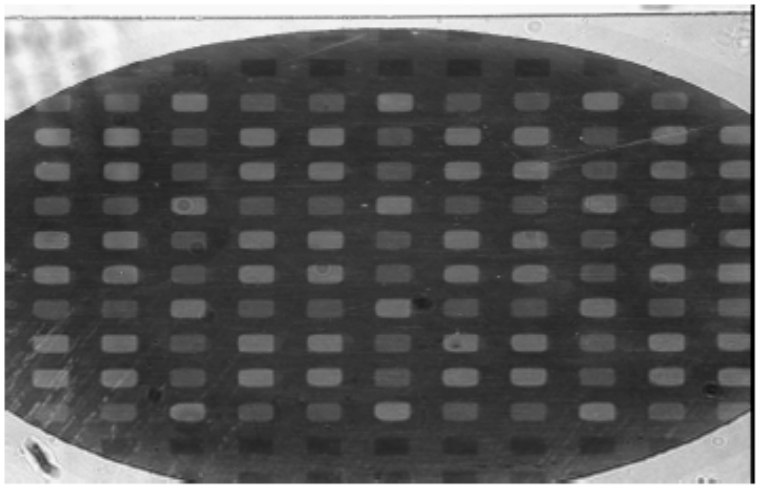

UCIrvin
University of California, I

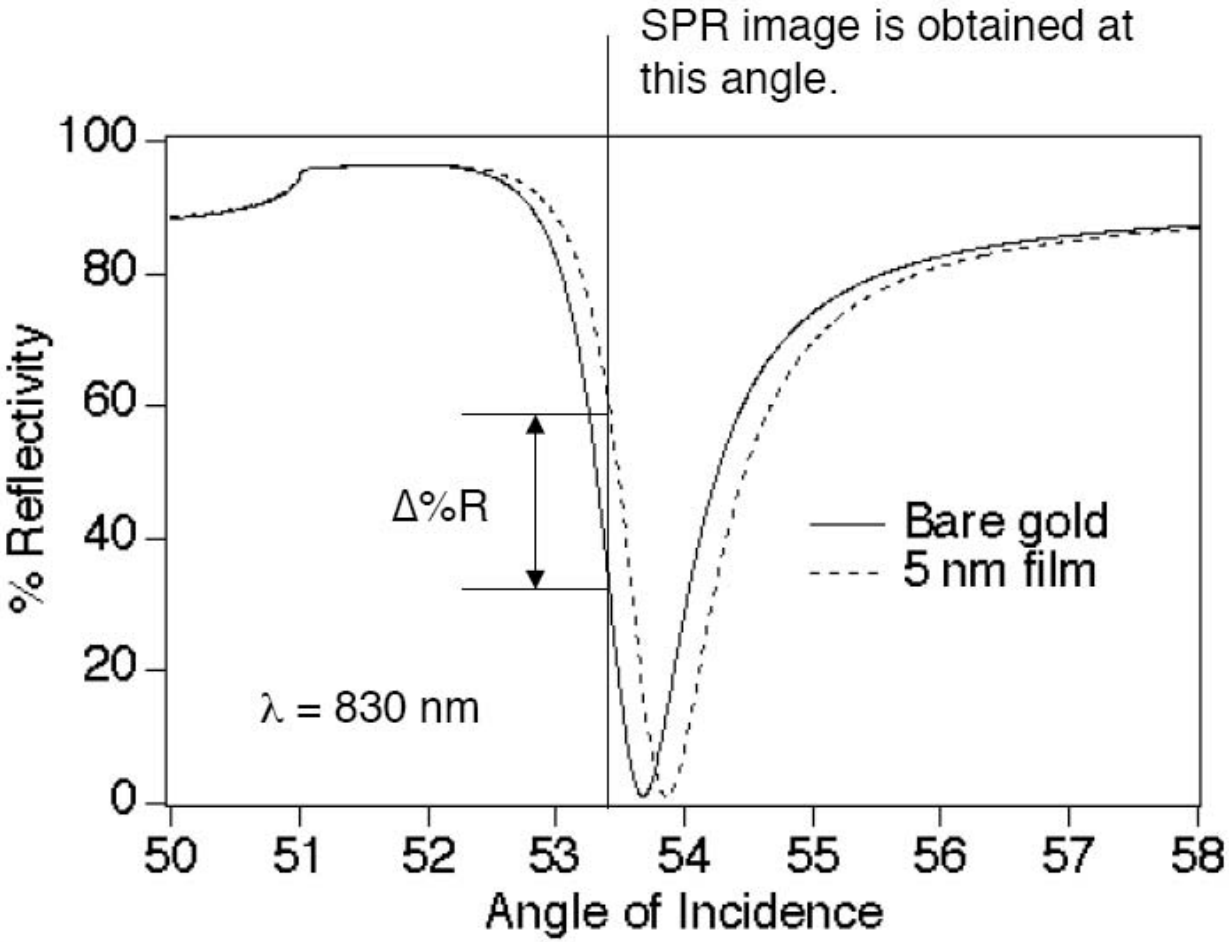

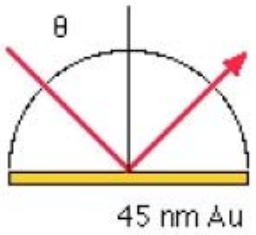

UCIrvine
University of California, Irvine

Probing Single Molecules and Single Nanoparticles by Surface-Enhanced Raman Scattering

SCIENCE • VOL. 275 • 21 FEBRUARY 1997

Shuming Nie* and Steven R. Emory

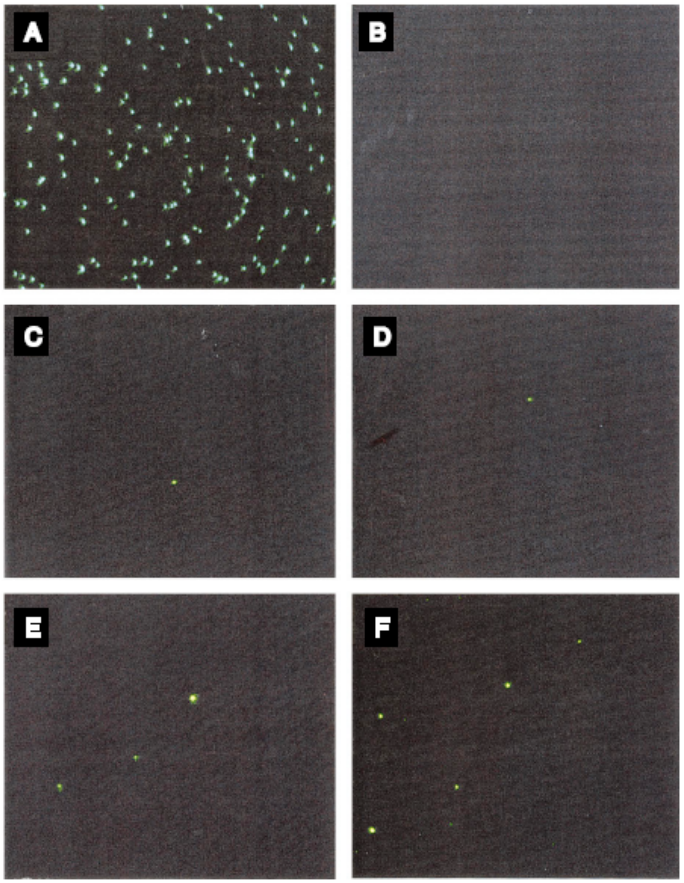

Fig. 1. Single Ag nanoparticles imaged with evanescent-wave excitation. Total internal reflection of the laser beam at the glass-liquid interface was used to reduce the laser scattering background. The instrument setup for evanescent-wave microscopy was adapted from Funatsu *et al.* (*11*). The images were directly recorded on color photographic film (ASA-1600) with a 30-s exposure by a Nikon 35-mm camera attached to the microscope. (**A**) Unfiltered photograph showing scattered laser light from all particles immobilized on a polylysine-coated surface. (**B**) Filtered photographs taken from a blank Ag colloid sample (incubated with 1 mM NaCl and no R6G analyte molecules). (**C**) and (**D**) Filtered photographs taken from a Ag colloid sample incubated with 2×10^{-11} M R6G. These images were selected to show at least one Raman scattering particle. Different areas of the cover slip were rapidly screened, and most fields of view did not contain visible particles. (**E**) Filtered photograph taken from Ag colloid incubated with 2×10^{-10} M R6G. (**F**) Filtered photograph taken from Ag colloid incubated with 2×10^{-9} M R6G. A high-performance bandpass filter was used to remove the scattered laser light and to pass Stokes-shifted Raman signals from 540 to 580 nm (920 to 2200 cm^{-1}). Continuous-wave excitation at 514.5 nm was provided by an Ar ion laser. The total laser power at the sample was 10 mW. Note the color differences between the scattered laser light in (A) and the red-shifted light in (C) through (F).

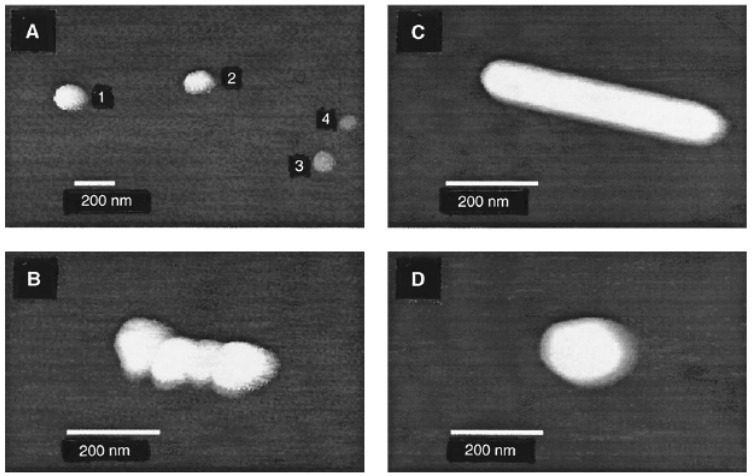

Fig. 2. Tapping-mode AFM images of screened Ag nanoparticles. (**A**) Large area survey image showing four single nanoparticles. Particles 1 and 2 were highly efficient for Raman enhancement, but particles 3 and 4 (smaller in size) were not. (**B**) Close-up image of a hot aggregate containing four linearly arranged particles. (**C**) Close-up image of a rod-shaped hot particle. (**D**) Close-up image of a faceted hot particle.

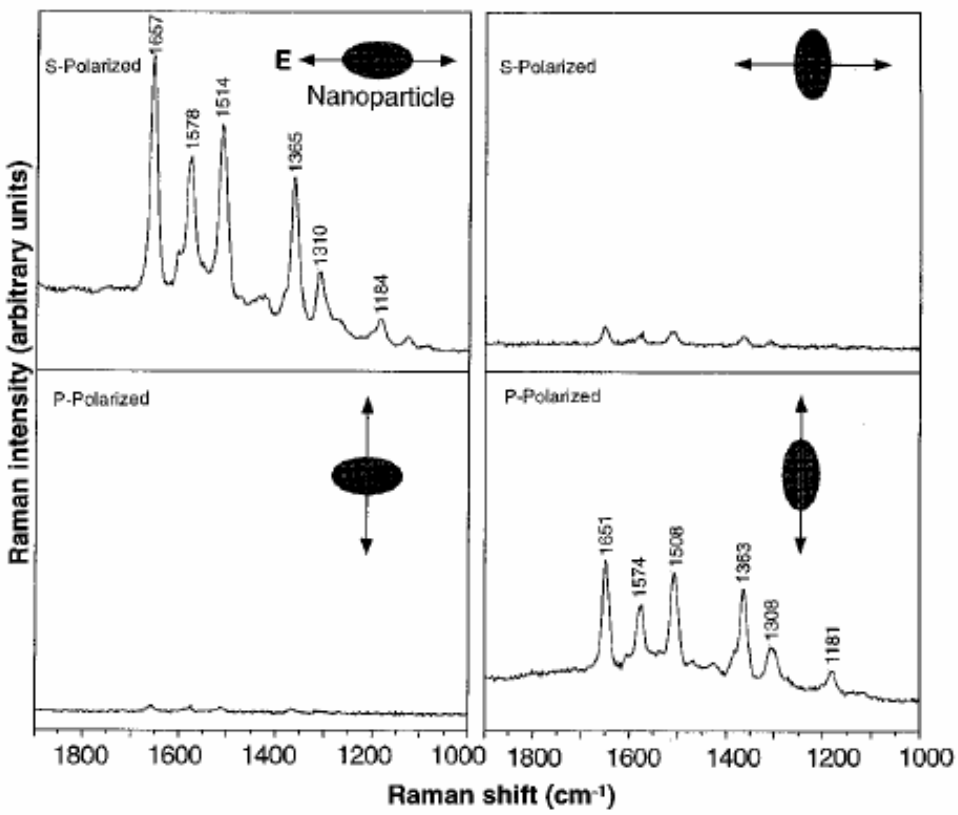

Fig. 3. Surface-enhanced Raman spectra of R6G obtained with a linearly polarized confocal laser beam from two Ag nanoparticles. The R6G concentration was 2×10^{-11} M, corresponding to an average of 0.1 analyte molecule per particle. The direction of laser polarization and the expected particle orientation are shown schematically for each spectrum. Laser wavelength, 514.5 nm; laser power, 250 nW; laser focal radius, ~250 nm; integration time, 30 s. All spectra were plotted on the same intensity scale in arbitrary units of the CCD detector readout signal.

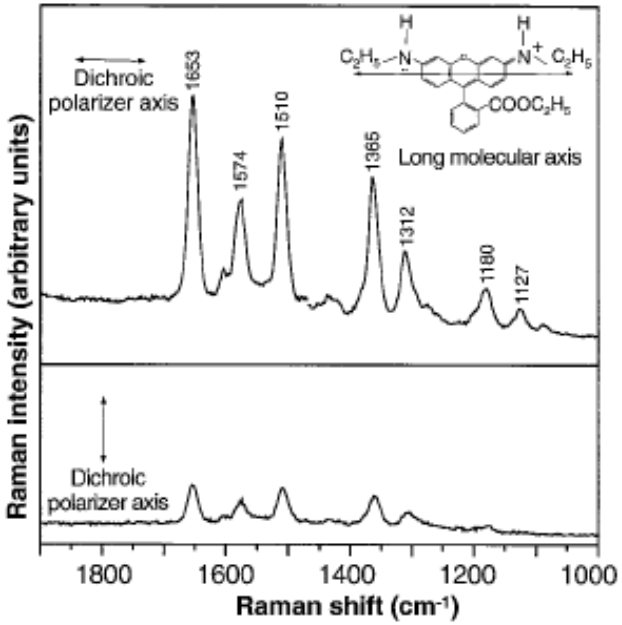

Fig. 4. Emission-polarized surface-enhanced Raman signals of R6G observed from a single Ag nanoparticle with a polarization-scrambled confocal laser beam. A dichroic sheet polarizer was rotated 90° to select Raman scattering signals polarized parallel (upper spectrum) or perpendicular (lower spectrum) to the long molecular axis of R6G. (**Inserts**) Structure of R6G, the electronic transition dipole (along the long axis when excited at 514.5 nm), and the dichroic polarizer orientations. Other conditions as in Fig. 3.

troscopic signatures of adsorbed molecules. For single rhodamine 6G molecules adsorbed on the selected nanoparticles, the intrinsic Raman enhancement factors were on the order of 10^{14} to 10^{15}, much larger than the ensemble-averaged values derived from conventional measurements. This enormous enhancement leads to vibrational Raman signals that are more intense and more stable than single-molecule fluorescence.

Electromagnetic contributions to single-molecule sensitivity in surface-enhanced Raman scattering

PRE 62 4318

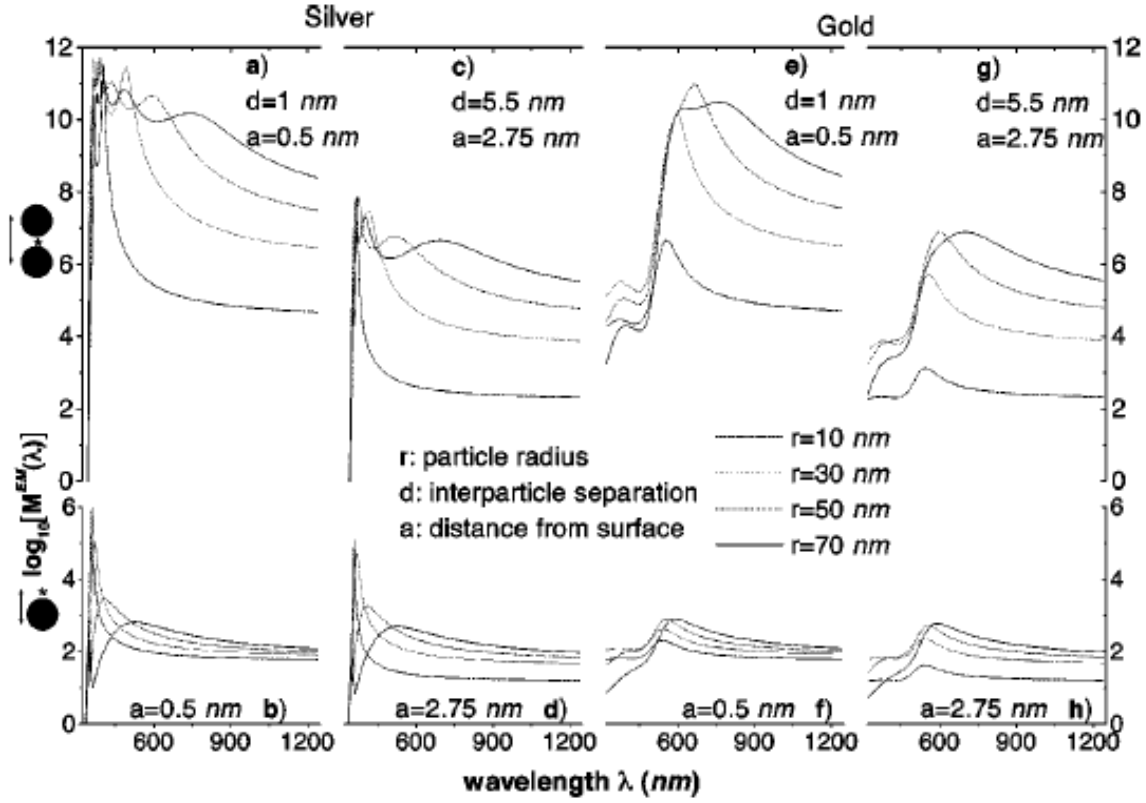

FIG. 3. (Color) EM-enhancement factor M^{EM} at a cross section through six different silver particle configurations. The wavelength of the incident field is $\lambda = 514.5$ nm with vertical polarization. The left-hand column illustrates the EM enhancement for dimer configurations of two spheres (top) and two polygons (bottom) with a separation of 1 nm. The middle column shows the same situation, but with a separation distance of 5.5 nm. The right-hand column shows the case of an isolated single particle. All particles share a common largest dimension of 90 nm. Note that the color scale from dark blue to dark red is logarithmic, covering the interval $10^0 < M^{EM} < 10^8$. Regions with enhancement outside this interval are shown in dark blue and dark red, respectively.

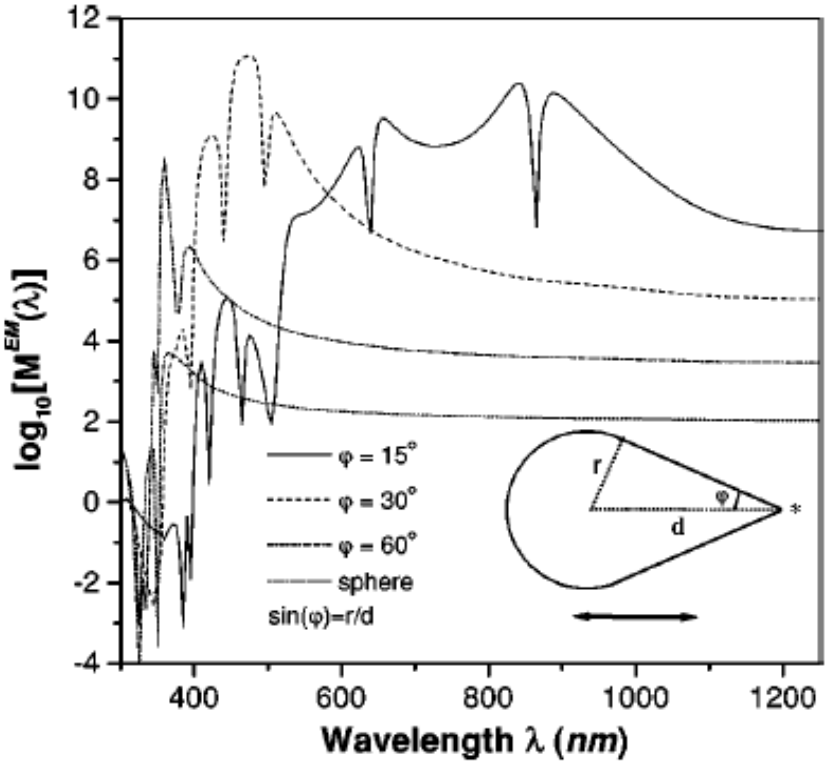

FIG. 5. EM-enhancement factor for a rotationally symmetric silver droplet as a function of the angle defining the opening edge ϕ. The field is polarized parallel to the axis of the droplet and the evaluation position (star) is located 0.5 nm outside the tip. As the droplet becomes sharper the enhancement increases several orders of magnitude.

Nanosphere Arrays with Controlled Sub-10-nm Gaps as Surface-Enhanced Raman Spectroscopy Substrates

J. AM. CHEM. SOC. 2005, *127*, 14992−14993

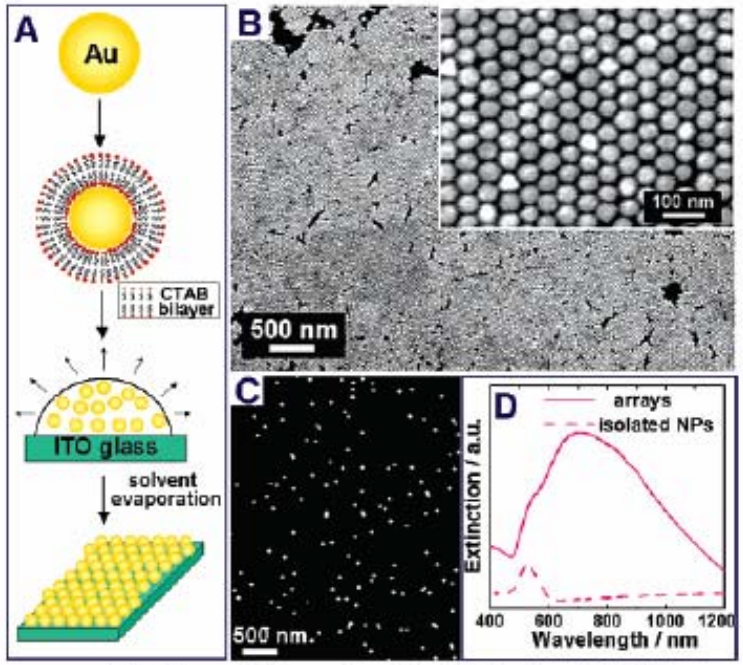

Figure 1. (A) Schematic illustration of the fabrication of sub-10-nm gap Au NP arrays. (B) SEM image of the arrays. (C) SEM image of monolayer of isolated Au NPs on ITO glass. (D) Vis−NIR extinction spectrum of the monolayer of isolated Au NPs and arrays.

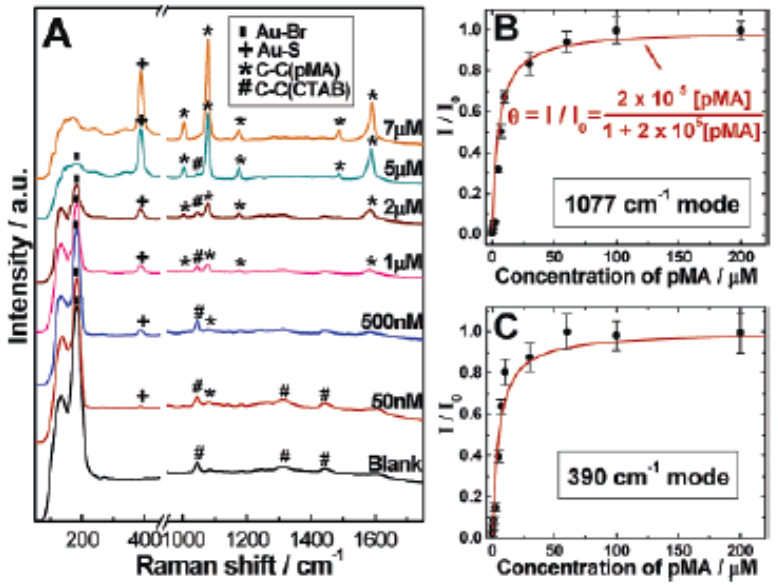

Figure 2. (A) SERS spectra of 5 μL of pMA with different concentrations deposited on the NP arrays. The excitation laser wavelength is 785 nm. Adsorption isotherm of pMA on the NP arrays obtained according to (B) 1077 and (C) 390 cm^{-1} modes in the SERS spectra. I_0 is the peak intensity of a saturated pMA monolayer.

Profiling the Near Field of a Plasmonic Nanoparticle with Raman-Based Molecular Rulers

NANO LETTERS

2006
Vol. 6, No. 10
2338−2343

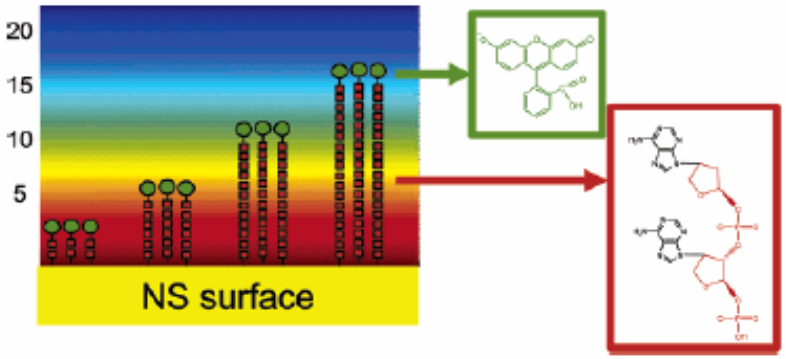

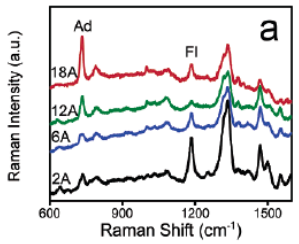

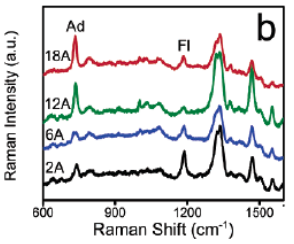

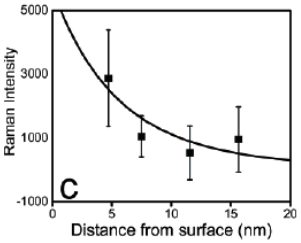

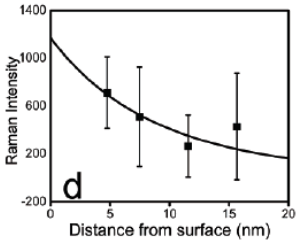

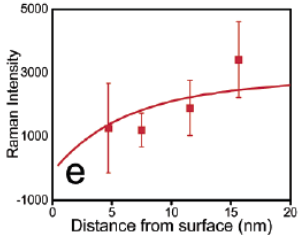

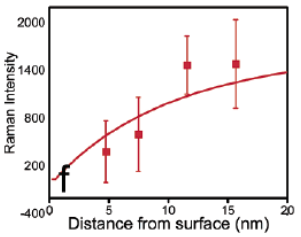

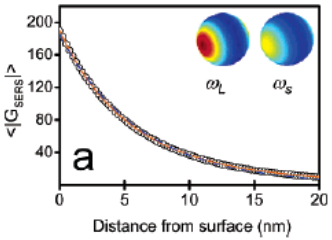

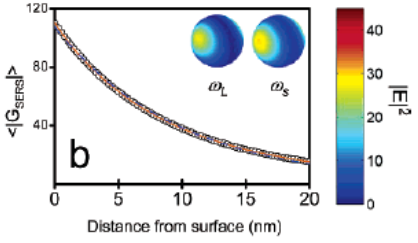

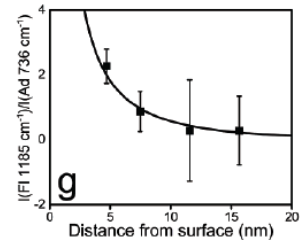

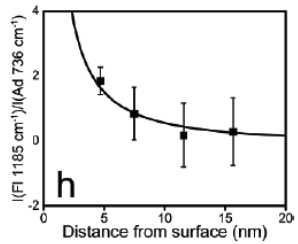

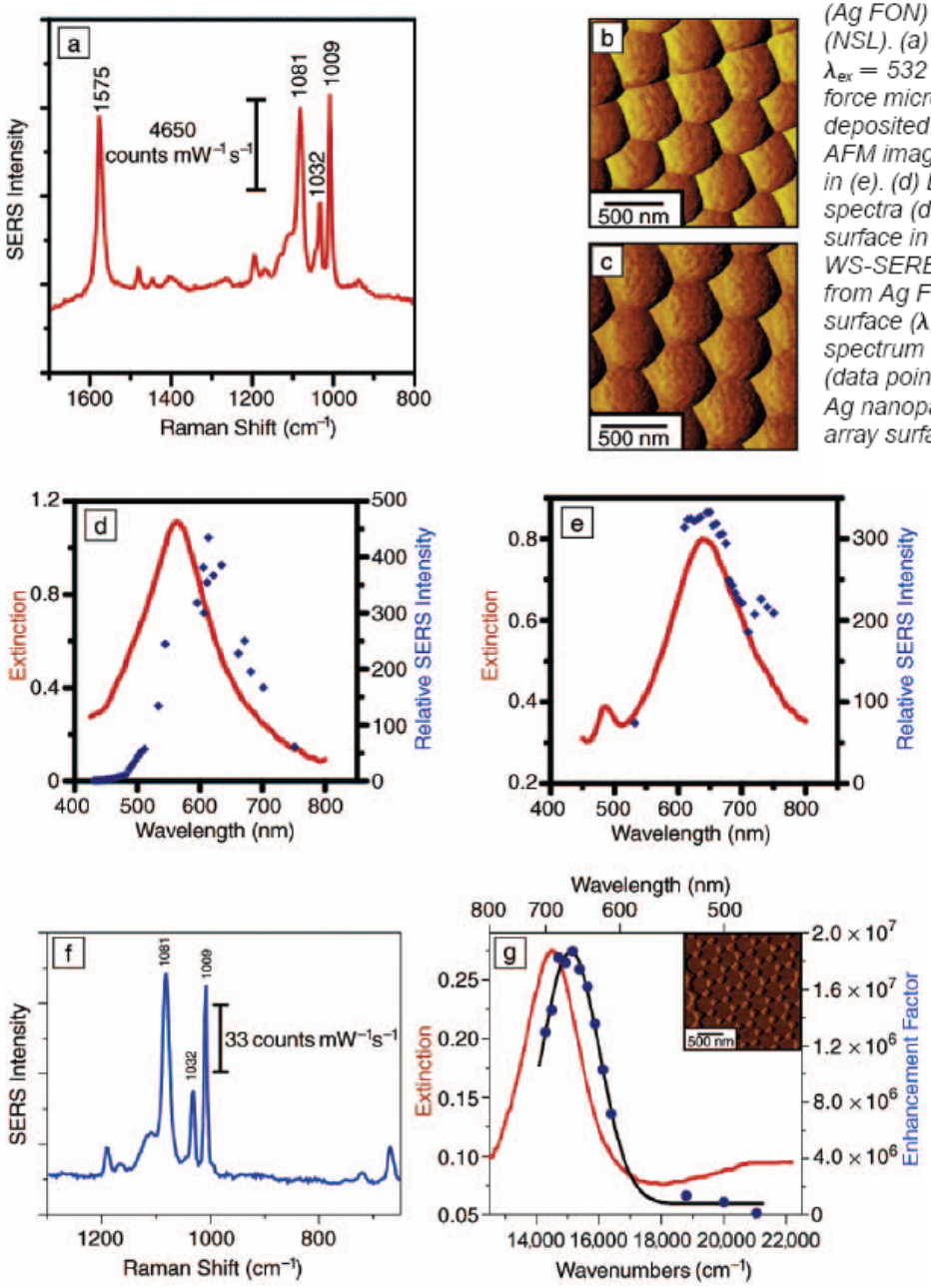

Figure 6. Localized surface plasmon resonance (LSPR), surface-enhanced Raman spectroscopy (SERS), and wavelength-scanned surface-enhanced Raman excitation spectroscopy (WS-SERES) results for benzenethiol adsorbed on Ag film-over-nanosphere (Ag FON) surfaces and nanoparticle arrays fabricated by nanosphere lithography (NSL). (a) SERS spectrum measured from Ag FON surface with excitation wavelength λ_{ex} = 532 nm, power = 3.0 mW, and 100 s data acquisition time. (b) Contact-mode atomic force microscopy (AFM) image of Ag FON surface (nanosphere diameter D = 410 nm, deposited mass thickness d_m = 200 nm) used for SERS in (a). (c) Contact-mode AFM image of Ag FON surface (D = 500 nm, d_m = 250 nm) used for WS-SERES in (e). (d) LSPR spectrum (solid line, λ_{max} = 562 nm, FWHM = 144 nm) and WS-SERES spectra (data points) for the 1081 cm^{-1} band of benzenethiol measured from the Ag FON surface in (b). (e) LSPR spectrum (solid line, λ_{max} = 638 nm, FWHM = 131 nm) and WS-SERES spectra (data points) for the 1081 cm^{-1} band of benzenethiol measured from Ag FON surface in (c). (f) SERS spectrum measured from Ag nanoparticle array surface (λ_{ex} = 532 nm, power = 3.0 mW, 100 s data acquisition time). (g) LSPR spectrum (solid line, λ_{max} = 688 nm, FWHM = 95 nm) and WS-SERES spectra (data points) for the 1081 cm^{-1} band of benzenethiol measured from a Ag nanoparticle array surface. (inset) Tapping-mode AFM image of a representative array surface.

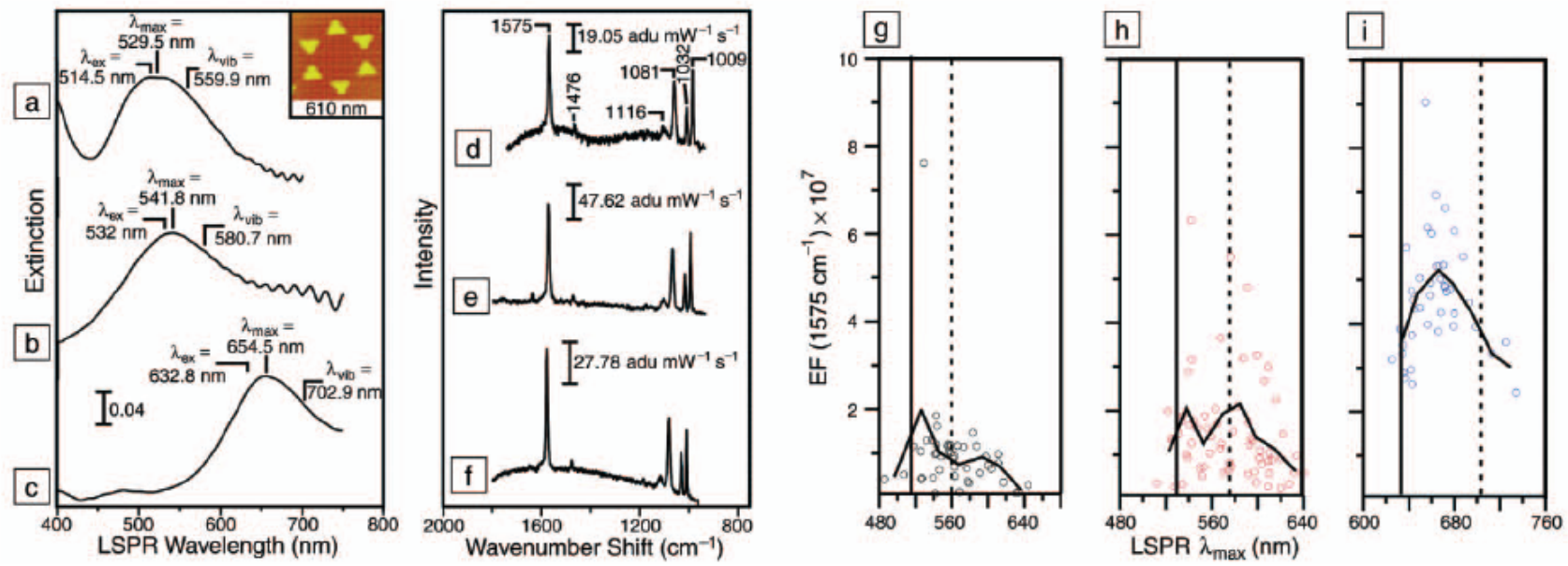

Figure 5. (a)–(f) Correlated, spatially resolved, localized surface plasmon resonance (LSPR) and surface-enhanced Raman spectroscopy (SERS) results for benzenethiol adsorbed on Ag nanoparticle arrays fabricated by nanosphere lithography. (a), (d) Ag nanoparticles fabricated with nanosphere diameter D = *280 nm and deposited mass thickness* d_m = *36 nm, probed with an excitation wavelength* λ_{ex} = *514.5 nm, power = 0.7 mW. A representative atomic force micrograph of the substrate is shown in the inset. (b), (e) Ag nanoparticles fabricated with* D = *280 nm,* d_m = *36 nm, probed with* λ_{ex} = *532.0 nm, power = 0.7 mW. (c), (f) Ag nanoparticles fabricated with* D = *400 nm,* d_m = *56 nm, probed with* λ_{ex} = *632.8 nm, power = 1.2 mW. (g)–(i) Plasmon-sampled surface-enhanced Raman excitation spectroscopy (PS-SERES) results for the 1575 cm^{-1} band of benzenethiol with three different excitation wavelengths: (g)* λ_{ex} = *514.5 nm, (h)* λ_{ex} = *532.0 nm, and (i)* λ_{ex} = *632.8 nm. For each* λ_{ex}, *both the wavelength location of the excitation (solid line) and the scattering (dashed line) are marked. The overlaid curves represent the bin-averaged values of the LSPR* λ_{max} *and the enhancement factor. Bin widths are (g) 24 nm, (h) 16 nm, and (i) 16 nm.*

Anal. Chem. 2003, *75*, 6171−6176

Spectroscopic Tags Using Dye-Embedded Nanoparticles and Surface-Enhanced Raman Scattering

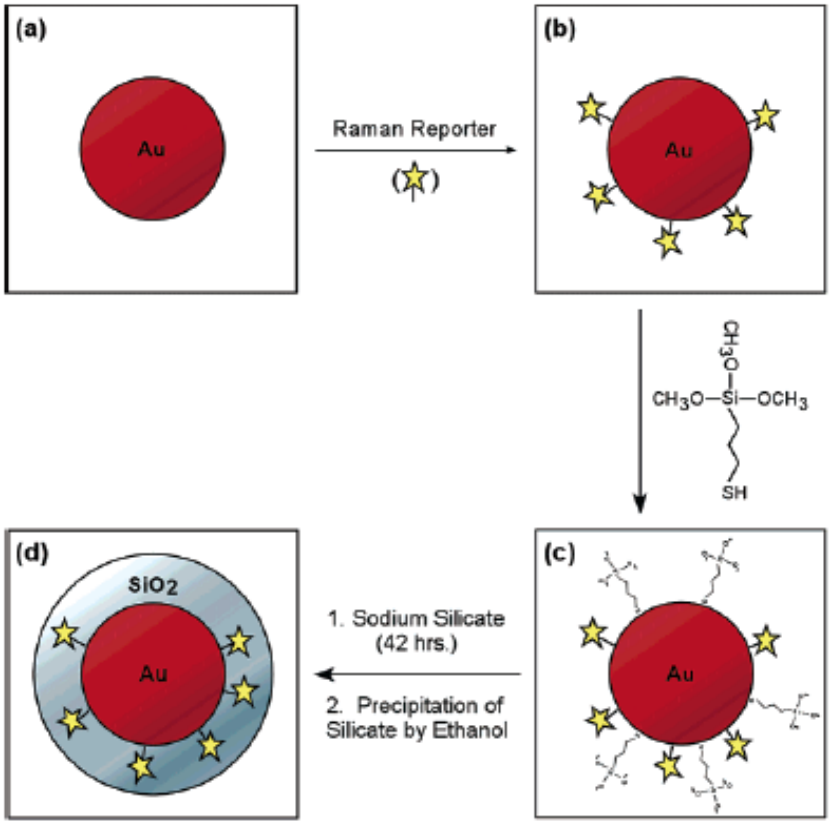

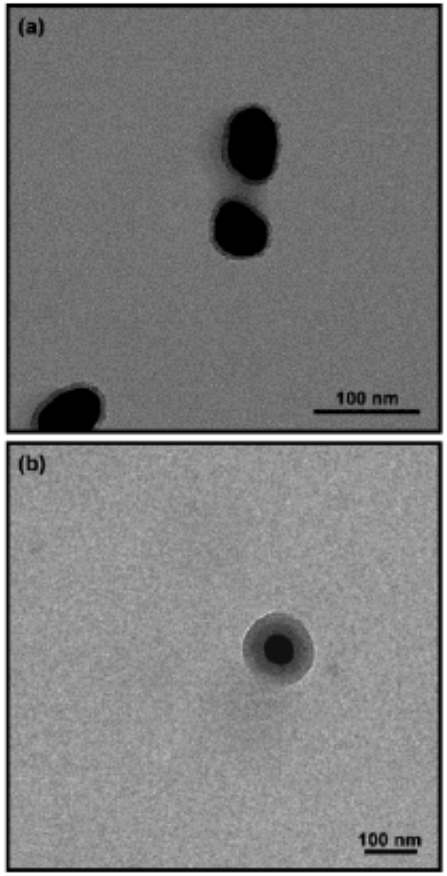

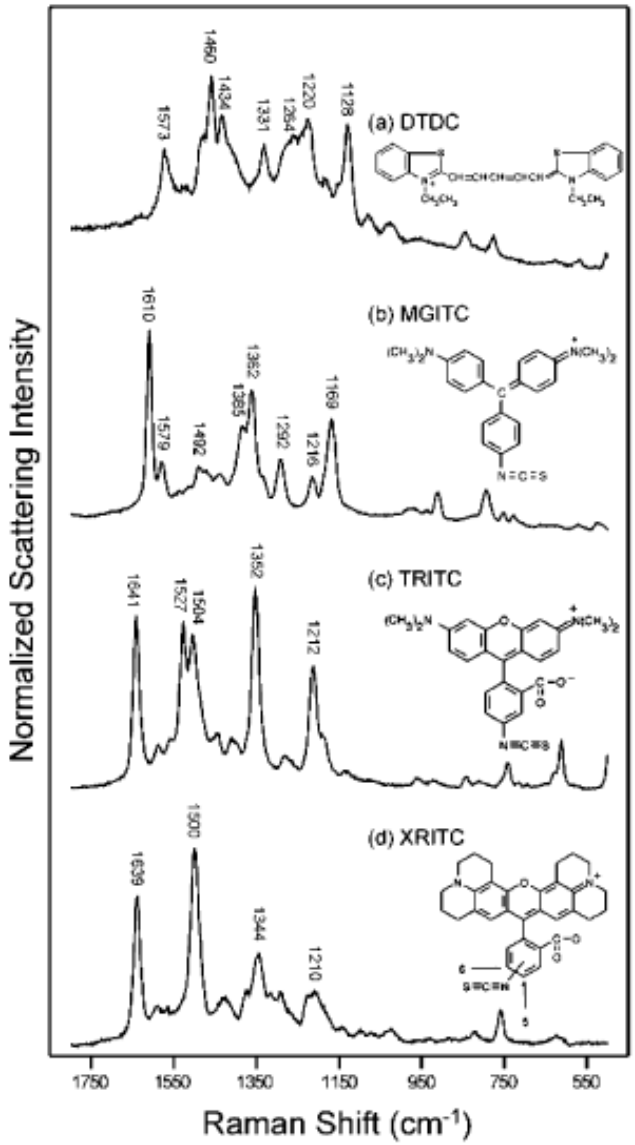

Figure 4. Chemical structures of four Raman reporters and their surface-enhanced resonance Raman spectra: (a) 3,3′-Diethylthiadicarbocyanine iodide (DTDC); (b) malachite green isothiocyanate (MGITC); (c) tetramethylrhodamine-5-isothiocyanate (TRITC); and (e) rhodamine-5-(and-6)-isothiocyanate (XRITC).

Anal. Chem. 2006, *78*, 6967−6973

Nanoparticle Probes with Surface Enhanced Raman Spectroscopic Tags for Cellular Cancer Targeting

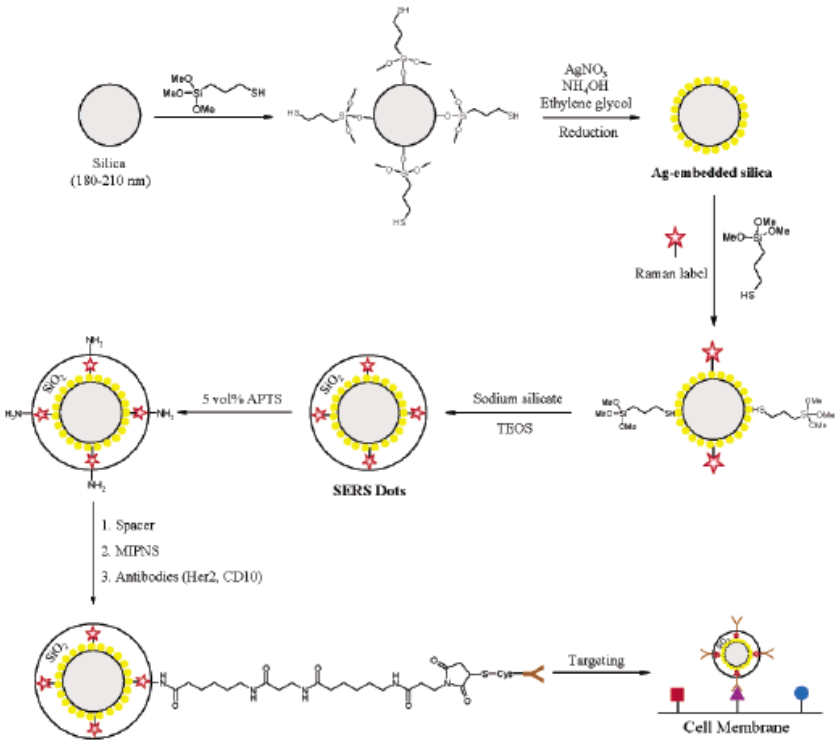

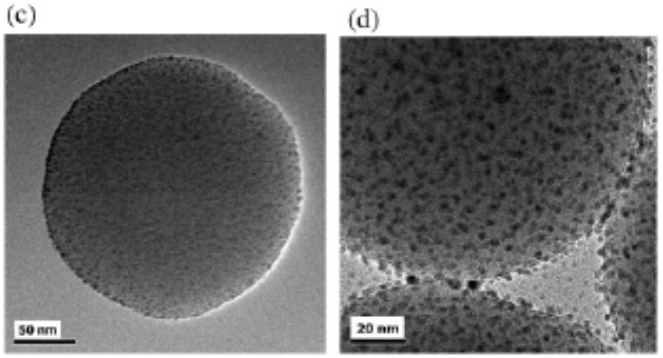

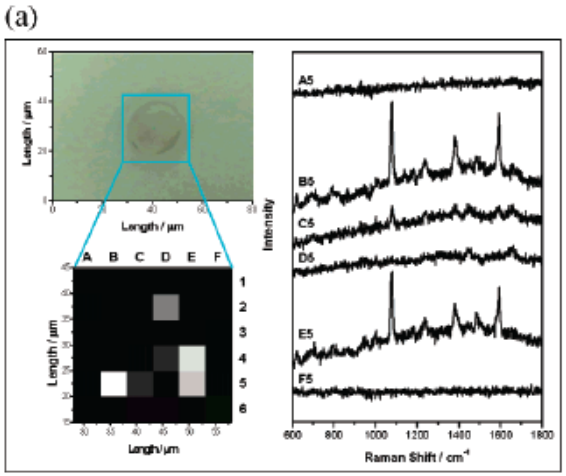

Anal. Chem. 2007, *79*, 916−922

Biological Imaging of HEK293 Cells Expressing PLCγ1 Using Surface-Enhanced Raman Microscopy

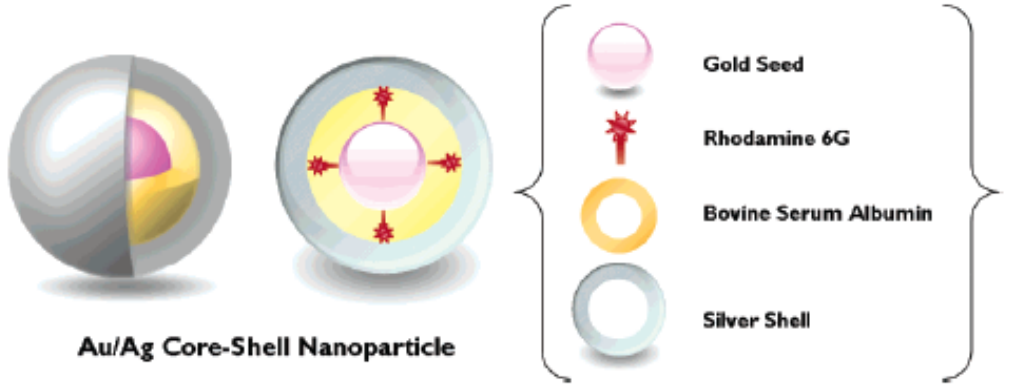

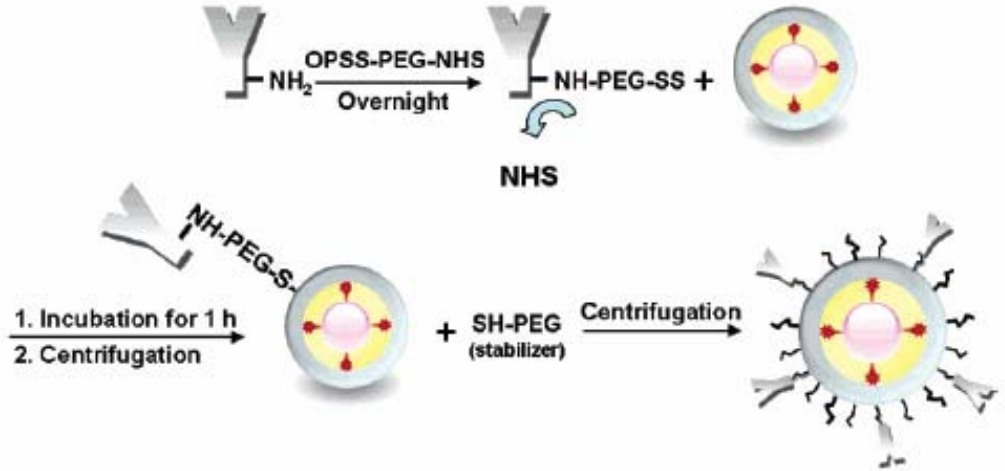

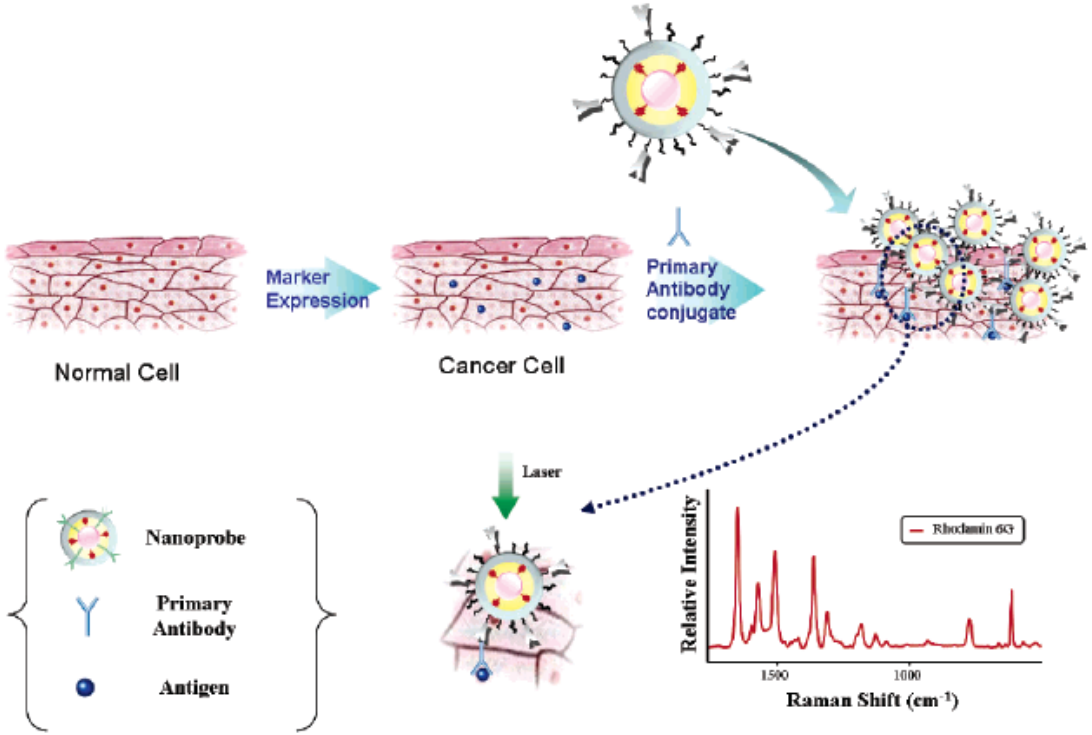

Figure 4. Schematic diagram depicting immobilization of Au/Ag core−shell nanoprobes on PLCγ1-expressing HEK293 cells and their SERS detection.

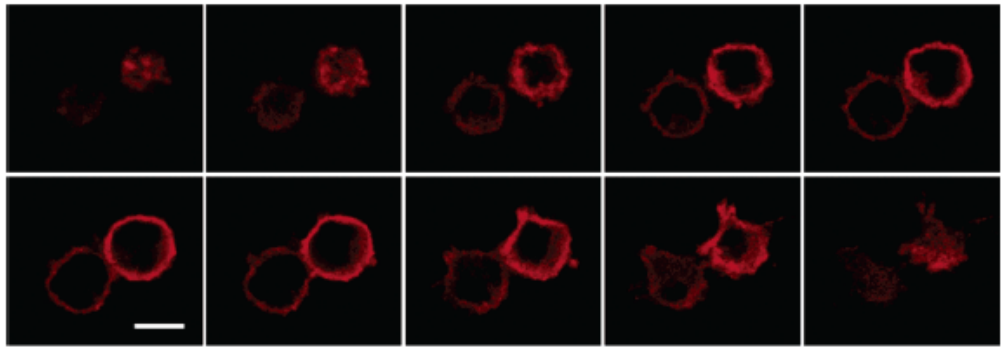

Figure 5. Serial fluorescence optical sections of PLCγ1-expressing HEK293 cells using red QDs. The *z*-axis interval of optical slices is 1.3 μm. Cells were incubated for 30 min in red QDs, after which the free QDs were washed away. These fluorescence images indicate that PLCγ1 markers are only expressed on the surface membranes. Scale bar, 10 μm.

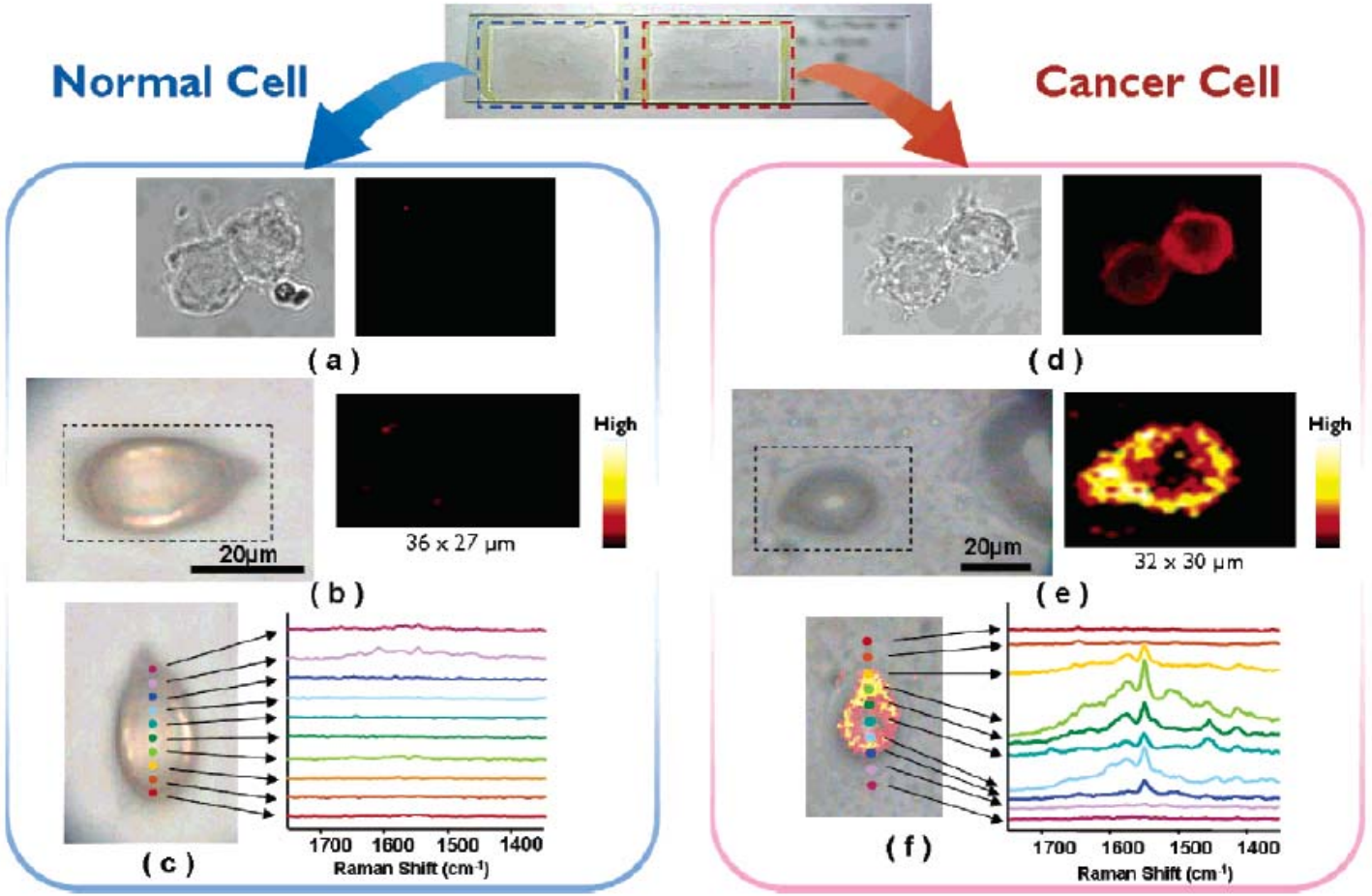

Figure 6. Fluorescence and SERS images of normal HEK293 cells and PLCγ1-expressing HEK293 cells. (a) QD-labeled fluorescence images of normal cells: (left) brightfield image, (right) fluorescence image. (b) SERS images of single normal cell: (left) brightfield image, (right) Raman mapping image of single normal cell based on the 1650-cm^{-1} R6G peak. The cell area was scanned with an interval of 1 μm. Intensities are scaled to the highest value in each area. (c) Overlay image of brightfield and Raman mapping for single normal cell. Colorful spots indicate the laser spots across the middle of the cell along the *y* axis. (d) QD-labeled fluorescence images of cancer cells: (left) brightfield image, (right) fluorescence image. (e) SERS images of single cancer cell: (left) brightfield image, (right) Raman mapping image of single cancer cell based on the 1650-cm^{-1} R6G peak. The cell area was scanned with an interval of 1 μm. Intensities are scaled to the highest value in each area. (f) Overlay image of brightfield and Raman mapping for single cancer cell. Colorful spots indicate the laser spots across the middle of the cell along the *y* axis.

J|A|C|S
COMMUNICATIONS

Published on Web 12/15/2006

Mammalian Cell Surface Imaging with Nitrile-Functionalized Nanoprobes: Biophysical Characterization of Aggregation and Polarization Anisotropy in SERS Imaging

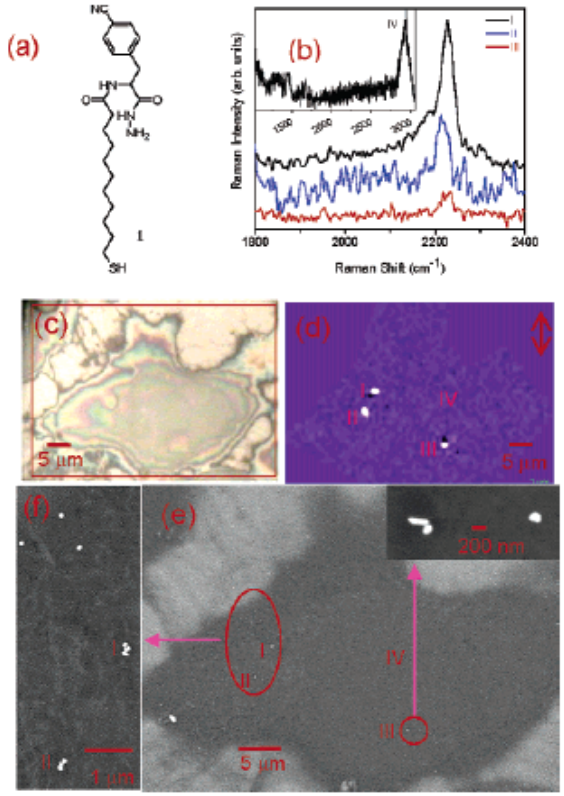

Figure 1. (a) The chemical structure of Raman reporter **1**; (b) Raman spectra of the CN vibration mode extracted from positions I, II, and III of the cell shown in the optical image (c). Inset of (b) is a cellular Raman spectrum taken from spot IV of the same cell. (d) Raman intensity map of the C≡N band of the same cell, and (e) the corresponding SEM image. Inset in (e) showed the NPs in the lower right circle. (f) The group of NPs as shown in the large oval of (e).

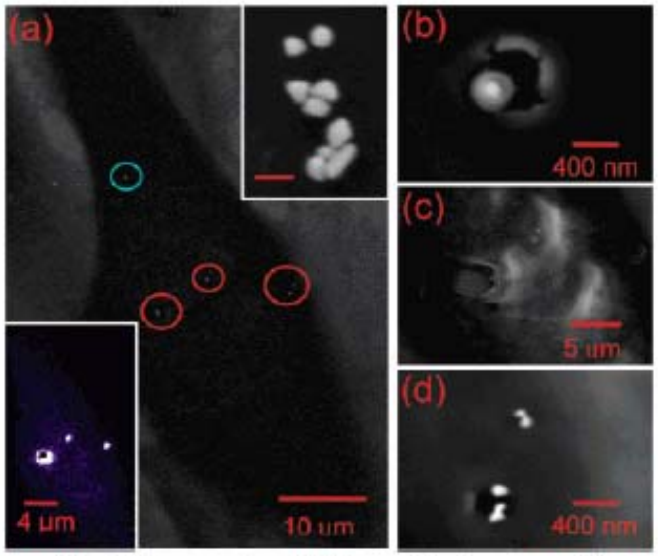

Figure 2. (a) SEM image of a cell. Upper right inset: magnification of a group of aggregated NPs. The scale bar is 200 nm. Lower left inset: the corresponding Raman intensity image of the same cell obtained with a power density of 10^5 W/cm^2. Laser-induced damage to the cell is shown in (b) the monomer (blue circle in a), (c) the aggregates, and (d) a pair of dimers.

Glass Surface Modification

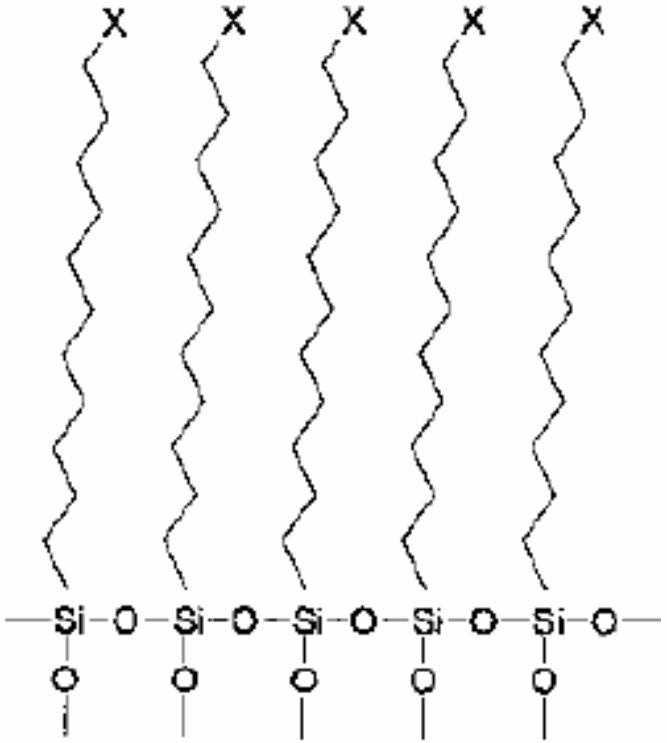

Hydroxylated Glass Surface

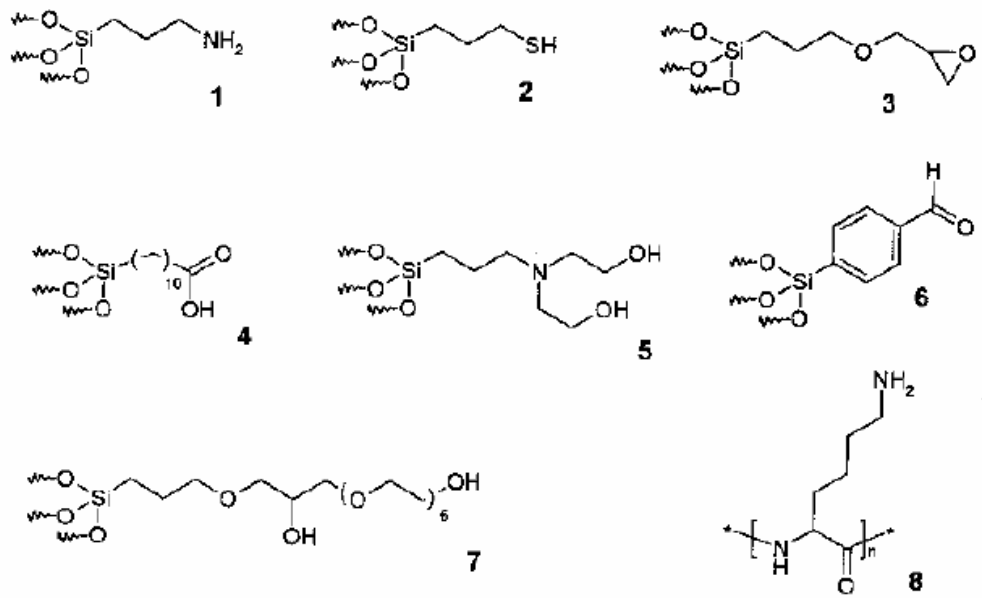

Scheme 2.2 Reagents for derivatization of glass surfaces. 1 APTES = aminopropyltriethoxysilane; **2** MPTS = 3-mercaptopropyltrimethoxysilane; **3** GPTS = glycidoxypropyltrimethoxysilane; **4** TETU = triethoxysilane undecanoic acid; **5** HE-APTS = bis(hydroxyethyl)aminopropyltriethoxysilane); **6** 4-trimethoxysilylbenzaldehyde; **7** GPTS/HEG = glycidoxypropyltrimethoxysilane-hexaethylene glycol; **8** poly(lysine).

Scheme 2.1 2D schematic description of a polysiloxane monolayer on a glass surface (X = terminal functional

Gold Surface Modification

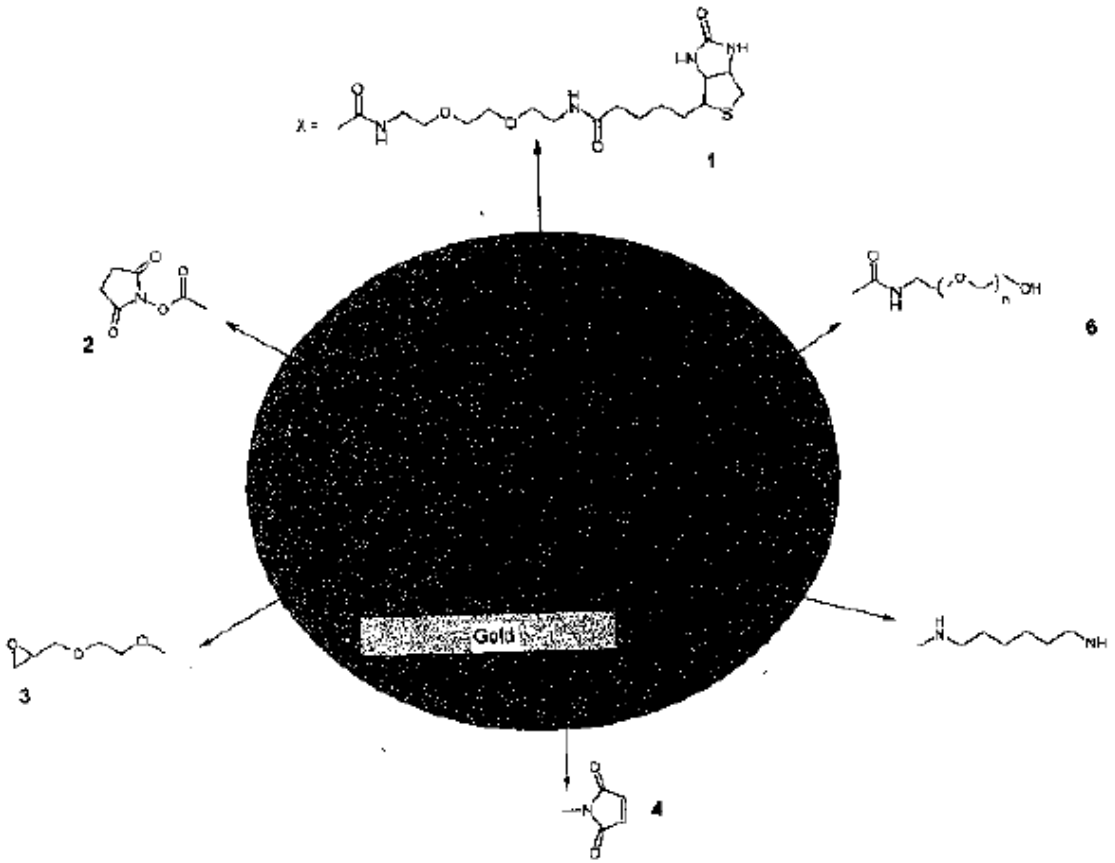

Scheme 2.3 Schematic respresentation of long-chain alkanethiol monolayers (e.g. 16 mercapto-hexadecanoic acid) on gold with different terminal functional groups.

1, biotin; 2, NHS-ester (NHS, N-hydroxysuccin-imide); 3, epoxy-ethylene glycol;
4, maleimide; 5, diaminohexane; 6 oligo (ethylene glycol).

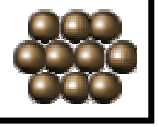

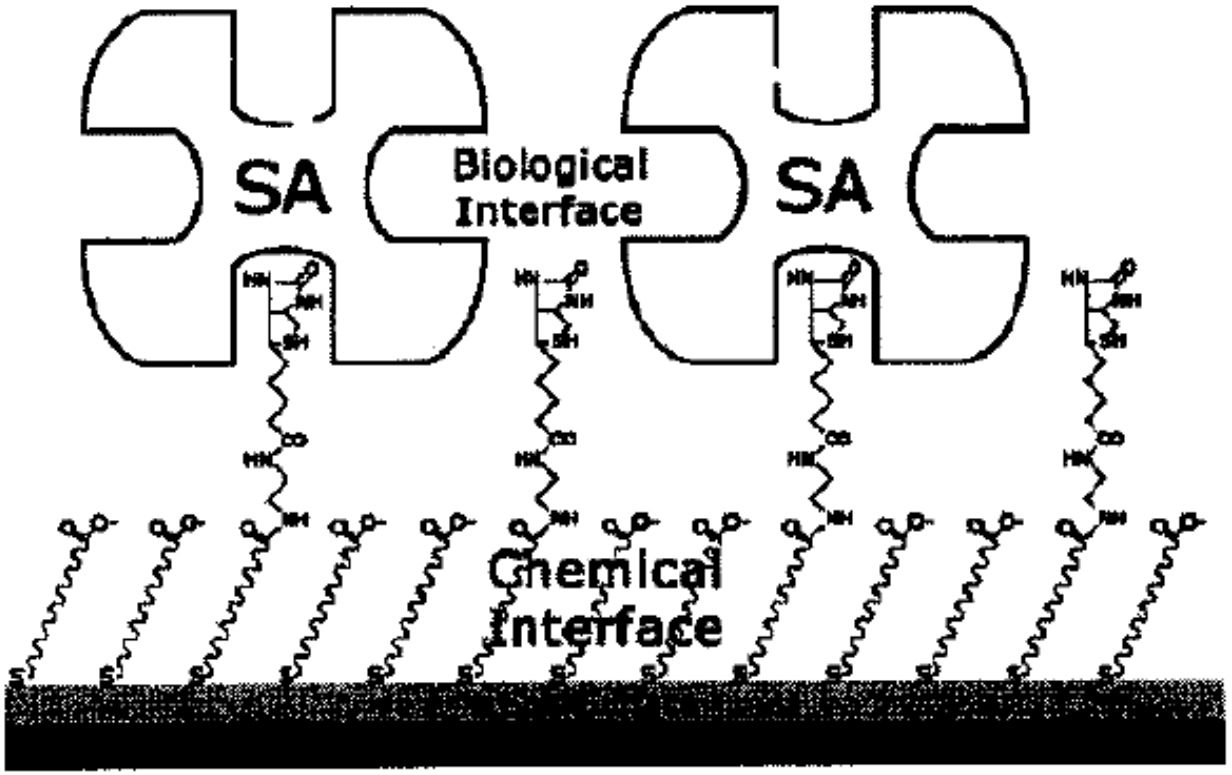

Figure 2.3 Schematic respresentation of a steptavidin sensor surface assembled on a reaction-controlled biotinylated SAM [28].

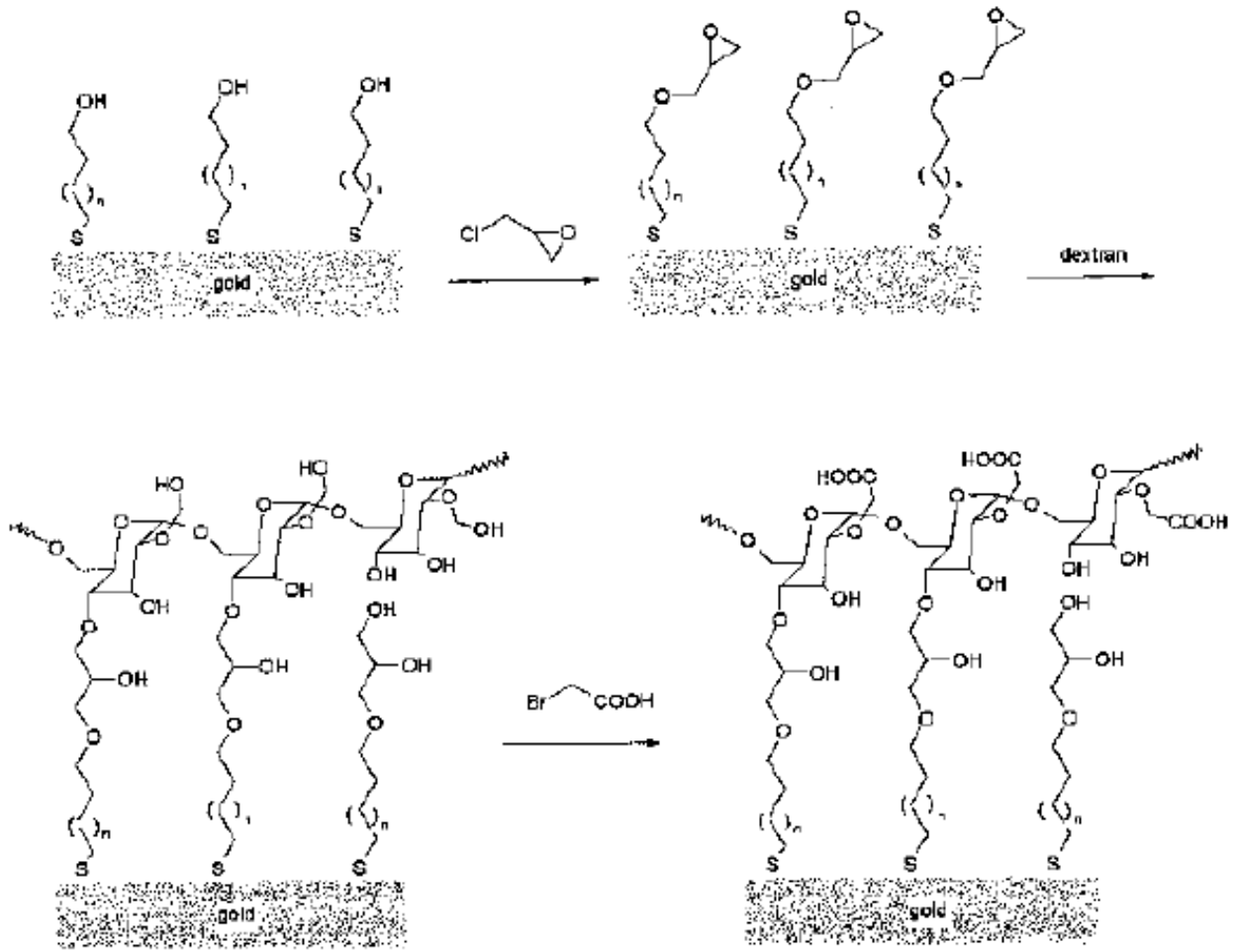

Scheme 2.4 Reaction schemes for preparing a hydrogel dextran matrix [41].

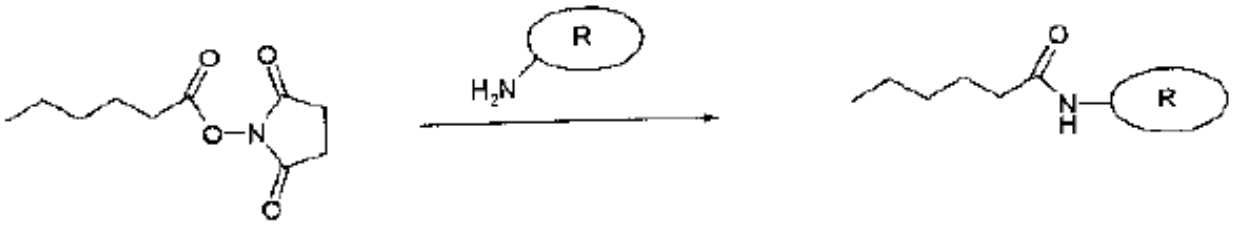

Scheme 2.6 Surface coupling reaction of NHS-esters with the amino residues of the side-chains of polypeptides (lysine units). R, protein.

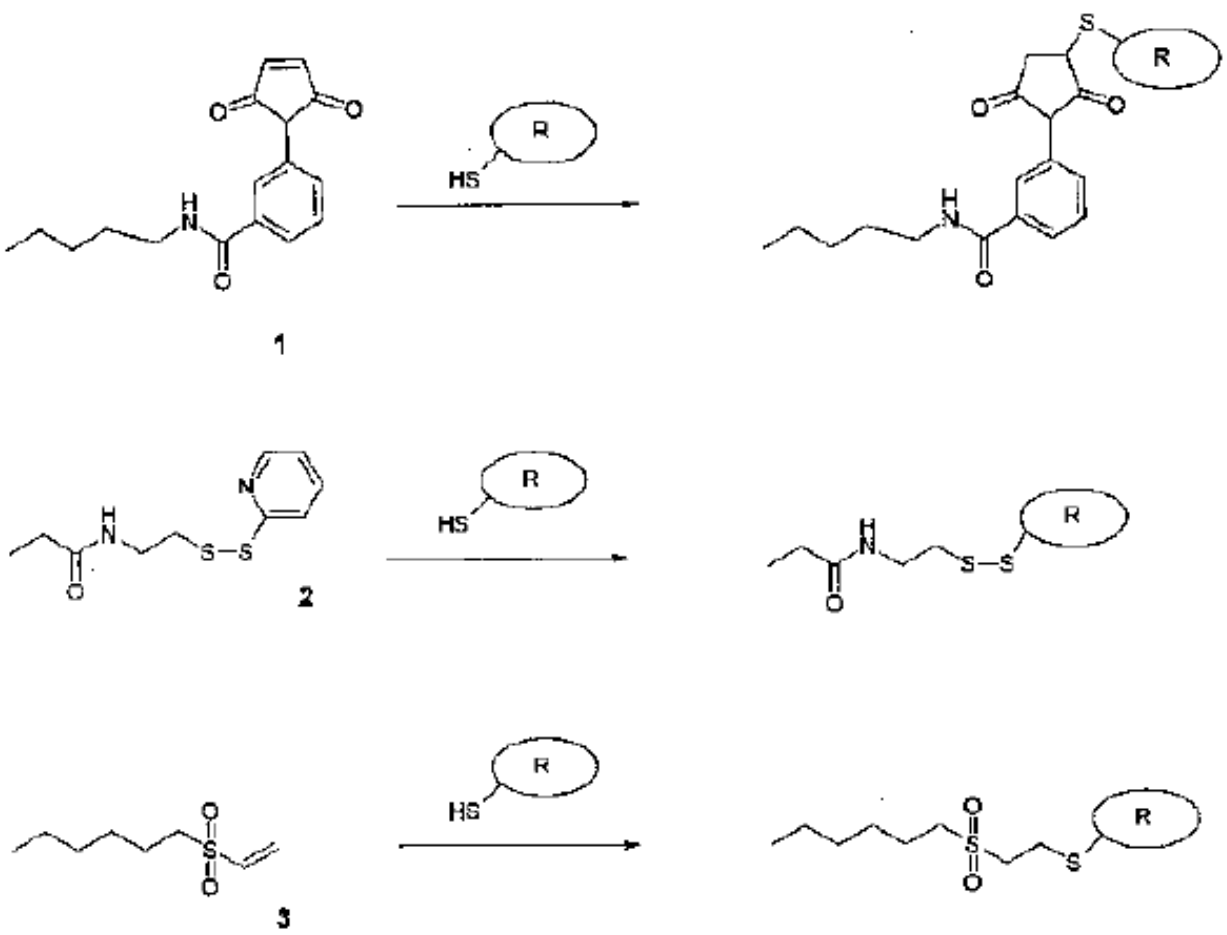

Scheme 2.7 Surface modifications for the attachment of thiol residues (which are present in the side chains) of polypeptides (cysteine units). R, protein, **1**, maleimide; **2**, disulfides; 3, vinyl sulfone.

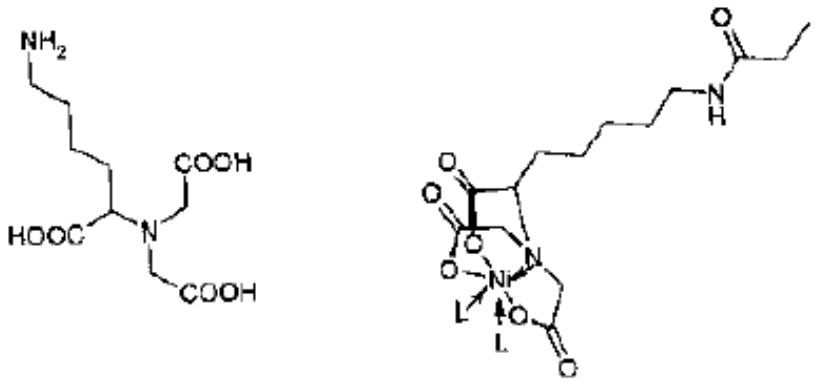

A B

Scheme 2.12 (A) Structure of N-(5-amino-1-carboxypentyl)iminodiacetic acid. (B) The quadridentate nitrilotriacetic acid (NTA) ligand forms a complex with four binding sites on the nickel metal which is present in the center. The two remaining binding sites can be coordinated with histidine ligands (L).

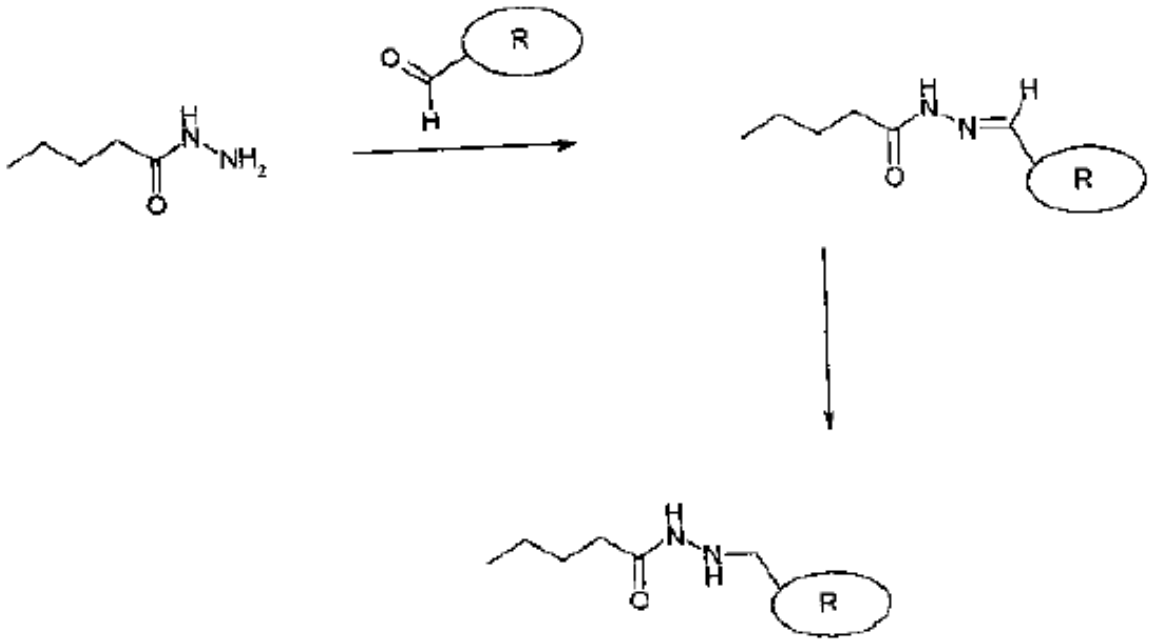

Scheme 2.13 Coupling of aldehyde residues of glycoproteins to hydrazide-terminated monolayers.

For a cell to move, it must adhere to a substrate and exert traction. Adhesion occurs at specific foci at which the actin cytoskeleton on the inside of the cell is linked via transmembrane receptors (integrins) to the extracellular matrix on the outside. These adhesion sites are composed of complexes of more than 50 different proteins

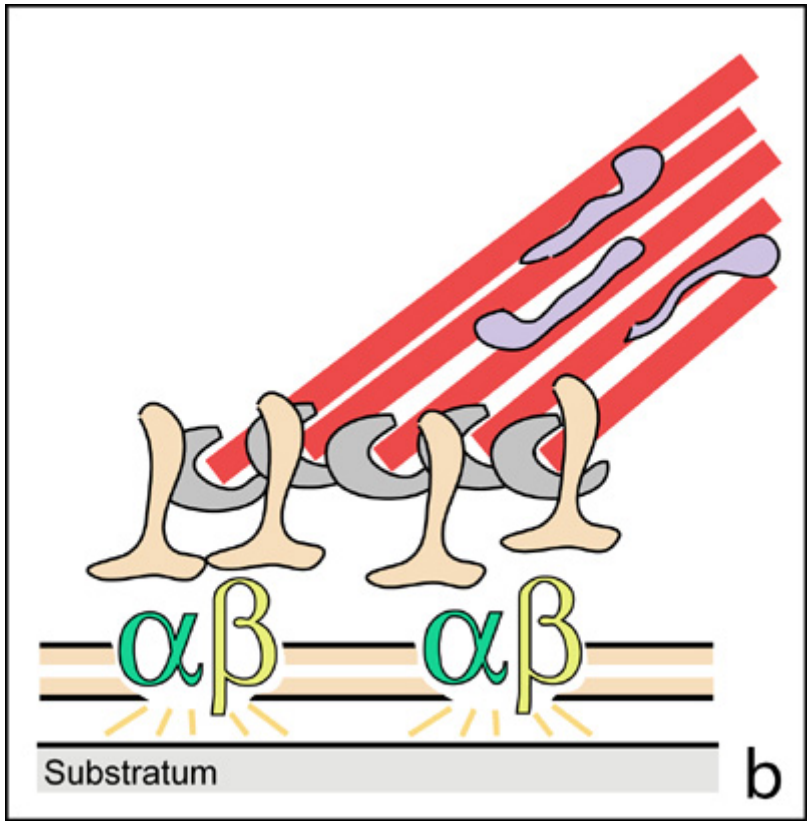

Highly simplified schematic illustration of the organisation of a focal adhesion. Transmembrane integrins (alpha/beta) bind to matrix ligands on the outside of the cell, and to a complex of molecules inside the cell that link to actin filaments. At focal adhesions, the actin filaments are bundled by actin filament cross-linkers, including the contractile protein myosin. Tension in the bundle, generated by myosin, is required to maintain the clustering of integrins and the integrity of focal adhesions

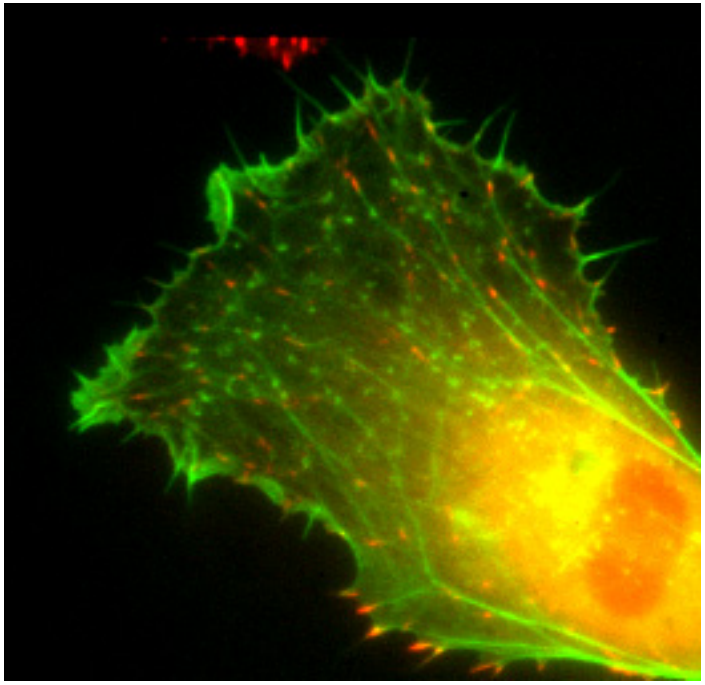

The formation of substrate adhesion sites in a migrating goldfish fibroblast. The cell was transfected with GFP-actin (green) and microinjected with rhodamine-tagged vinculin (an adhesion component; red). The protruding cell front is marked by a diffuse band of actin filaments (the lamellipodium), which contains radial filament bundles (filopodia) that project beyond the cell edge. Different types of adhesion foci (red) can be distiguished: small foci in association with lamellipodia and filopodia (focal complexes) and, behind the lamellipodium, larger foci associated with actin filament bundles (focal adhesions). Focal adhesions are also observed at the periphery of retracting cell edges (bottom region of figure). Focal complexes and focal adhesions in the advancing front remain stationary, relative to the substrate, whereas, focal adhesions at the retracting edges can slide.

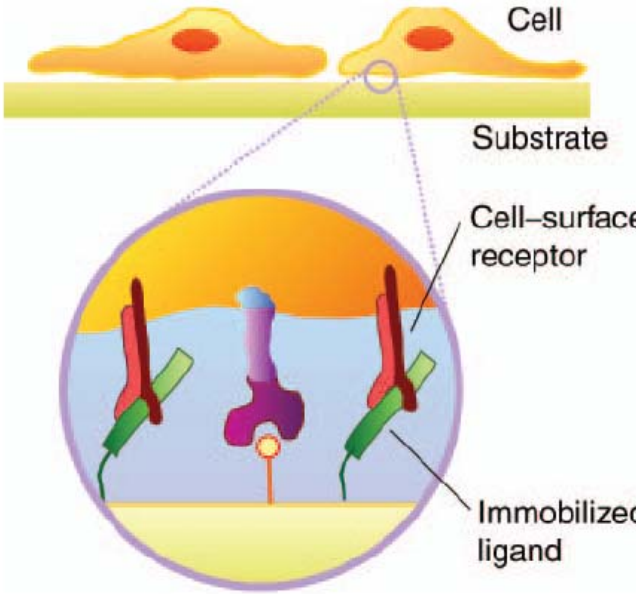

Figure 1. Most cells are adherent and must attach and spread on a matrix. The interaction of a cell with the substrate relies on the binding of cell–surface receptors with ligand proteins that are adsorbed to the material.

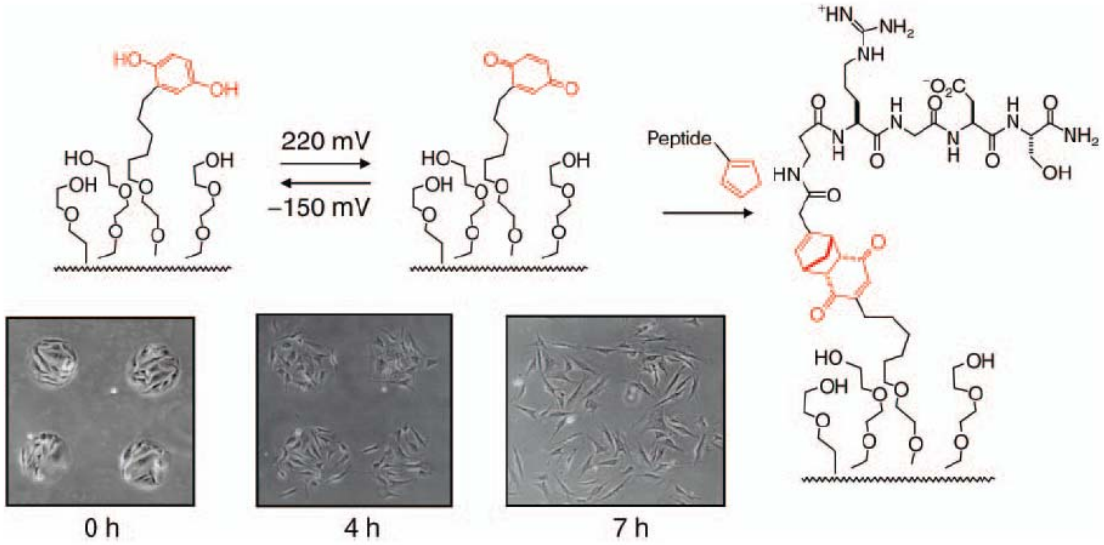

Figure 3. Design of a substrate that electrically turns on the immobilization of a ligand. An electrical potential converts a hydroquinone group to benzoquinone, which serves to immobilize a peptide ligand. The dynamic surfaces can initiate the migration of cells that are originally confined to 200 μm circular regions on the substrate.